THE PROPERTIES OF LEAD TITANATE THIN FILMS PRODUCED BY CHEMICAL VAPOUR DEPOSITION

By

LYNNETTE D. MADSEN

A Thesis
Submitted to the School of Graduate Studies
in Partial Fulfilment of the Requirements
for the Degree
Doctor of Philosophy

McMaster University

PROPERTIES OF LEAD TITANATE THIN FILMS

DOCTOR OF PHILOSOPHY (1994)	McMASTER UNIVERSITY
(Materials Science and Engineering)	Hamilton, Ontario

TITLE: The Properties of Lead Titanate Thin Films produced by Chemical Vapour Deposition

AUTHOR: Lynnette D Madsen, B.A.Sc. (University of Waterloo)
M.Eng. (Carleton University)

SUPERVISORS: Professor G.C. Weatherly and Dr. I. Emesh

NUMBER OF PAGES: xxvi, 229

ABSTRACT

This project focused on advancing the knowledge of chemical vapour deposition (CVD) $PbTiO_3$ thin films for future work on lead zirconate titanate or PZT ($PbZr_xTi_{1-x}O_3$) through an understanding of the structural, chemical and electrical properties of the material.

A study of the individual oxides, TiO_2 and PbO_x, prepared also by CVD, was made using transmission electron microscopy (TEM), scanning electron microscopy (SEM), Raman spectroscopy and x-ray diffraction (XRD), before a low pressure, low temperature process for $PbTiO_3$ was developed. The major factors in controlling the film composition and thickness uniformity were identified. The formation sequence for CVD $PbTiO_3$ films involved individual oxides of Ti and Pb, rather than pyrochlore-type phases. A Pb-rich composition ensured the formation of perovskite, however it resulted in the formation of a thin PbO_x surface layer. Removal of this layer by etching gave improved electrical properties. Capacitance measurements typically varied less than 1% over the frequency range and gave ϵ' values from 60-155. At 1 kHz, tan δ was ~ 0.01 and the resistivity was $\sim 10^{11}$ Ω.cm.

TEM examination of as-deposited films of $PbTiO_3$ revealed no macro-domains existed. After post-deposition annealing twinned structures acting as domains were found in grains, ~ 0.1 μm in size. The origin of the theoretical minimum grain size for twinning in $PbTiO_3$ thin films is discussed. A classification scheme for domain

structures was developed based on thin films of $PbTiO_3$ and PZT. Similarities were drawn between these domain structures and their bulk counterparts.

The multi-layered bottom electrode of Pt and Ti used in this study was found to react at temperatures $\leq 515°C$. At higher temperatures (698°C), the Ti layer was completely consumed, however the top surface of the Pt layer remained unaffected.

ACKNOWLEDGEMENTS

This project was supported financially by Northern Telecom Electronics Limited (NTEL), the Natural Science and Engineering Research Council of Canada (NSERC), and the Ontario Centre for Materials Research (OCMR).

The experimental equipment and facilities were made available by NTEL and Queen's University. Auger Electron Spectroscopy (AES) analysis was carried out at Bell-Northern Research (BNR). PbO_x and the preliminary $PbTiO_3$ electron microprobe (EMPA) was provided by the Surface Science Laboratory at the University of Western Ontario and detailed $PbTiO_3$ EMPA was provided by the CANMET laboratories in Ottawa. The Pt and Ti layers used as substrates were supplied by the Microelectronics Centre of North Carolina (MCNC), BNR and NTEL. The libraries of CANMET, McMaster University, Northern Telecom, and NRC CISTI provided the reference information. Travel funding was provided by NSERC, McMaster University (through Professor George Weatherly), NTEL, the Materials Research Society, Philips Electronics Instruments in conjunction with Arizona State University, the Institute of Physics and OCMR.

These films and the CVD films were tested electrically at Queen's University. In total, six sets of electrical test measurements were made over a nine month period. The necessary test apparatus to do reliable basic testing (small signal and hysteresis) and advanced reliability testing is located in the physics department of Queen's University, where there is over 5 years experience with testing of ferroelectric thin films. Their help and guidance with part of the project and access to their facilities was critical to its success and is truly appreciated.

The numerous individuals who assisted in this undertaking are thanked: Rick Adams (CVD equipment modifications and support), Marisa Ahmad (SEM), David Barrow (electrical testing), Chris Butcher (photography), Iain Calder (encouragement and the project idea), Graham Carpenter (assistance with crystallography), Jean-Pierre Charland (XRD guidance), Alison Clark (analysis), Doug Colton (encouragement and support), David Downham (electron diffraction), Ian Few (encouragement), Ellen Griswold (electrical testing and useful discussions), Robert Hadaway (managerial support), Professor Kay (general materials information), Dave Kingsley (RTA equipment support), Adrian Kitai (Ph.D. committee), Rita Leblond (comparison samples and substrates), Pak Leung (managerial support), Diane MacLean (substrates), Dawn and David Madsen (faith), David Mayer (TEM sample preparation), Paul McHugh (CVD equipment support), Jacques Mercier (encouragement), Rod Packwood (EMPA and related discussions), Anthony Petric (reference information), Brian Rioux and colleagues (substrates), Susan Ryneveld (graphics), Martine Simard-Normandin and her students (Raman spectroscopy), Claudine Simson (managerial support), Reed Seaver (standards calibration), and Louise Weaver (so much, including guidance, encouragement and fine wine). Others, not mentioned here who contributed, are nonetheless appreciated.

I would also like thank Drs. Ismail Emesh and George Weatherly, my supervisors at NTEL and McMaster University respectively, for their guidance and assistance.

Table of Contents

LIST OF ILLUSTRATIONS

LIST OF TABLES

ABBREVIATIONS and SYMBOLS*

a	lattice parameter
A	electrode area (m^2) or atomic mass in $g\text{-}mol^{-1}$ as appropriate
AES	Auger spectroscopy
at.%	atomic percent
BNR	Bell-Northern Research
BSE	backscattered electron emission
c	lattice parameter
C	capacitance or unit:Coulomb as appropriate
C-V	capacitance-voltage
CMOS	complementary metal oxide semiconductor
C_T	constant in Curie-Weiss temperature expression
CVD	chemical vapour deposition
d	dielectric thickness
d^*	diameter of the particle
$D(\alpha)$	penetration depth as a function of the angle α
DPM	dipivaloylmethane
DRAM	dynamic random access memory
E_a	apparent activation energy

---

* The standard abbreviations and symbols are used for elements and units of measure and are not defined herein.

E_c	coercive field
EDS	energy dispersive spectroscopy
EMPA	electron microprobe
f	frequency
FE	ferroelectric
FOD	dimethylheptofluoroacetylacetonate
F_x	flow of material x
G	Gibb's free energy
GA	glancing angle
IR	infrared
ITO	indium tin oxide
JCPDS	Joint Committee Powder Diffraction Standards
k	Boltzmann's constant
LCR	inductance/capacitance/resistance
LPCVD	low pressure chemical vapour deposition
MCNC	Microelectronics Centre of North Carolina
MOCVD	metalorganic chemical vapour deposition
MOD	metal organic decomposition
MOSFET	metal-oxide-semiconductor field-effect transistor
MRS	Materials Research Society
N.A.	not available
NSERC	Natural Science and Engineering Research Council of Canada
NTEL	Northern Telecom Electronics Limited

OCMR	Ontario Centre for Materials Research
OMCVD	organo-metallic chemical vapour deposition ≡ MOCVD
P	polarization or pressure as appropriate
$Pb(acac)_2$	lead acetylacetonate
$Pb(DPM)_2$	bis(dipivaloylmethanato) lead
$Pb(FOD)_3$	lead dimethylheptafluoroacetylacetonate
$Pb(OC_4H_9)_n$	lead tertiary butoxide
$Pb(thd)_2$	lead β-diketonate or tetramethylheptadione
PbEt	tetraethyl lead, $Pb(C_2H_5)_4$
PLZT	lead lanthanum zirconate titanate or $(Pb,La)(Zr,Ti)O_3$
P_r	remanent polarization
PRC	post-reaction chamber
P_s	polarization saturation
P_{sp}	spontaneous polarization
p_x	partial pressure of x
PZT	lead zirconate titanate $Pb(Zr,Ti)O_3$
q	charge produced at the electrodes
R	reaction rate
r^*	critical nucleus size
RAM	random access memory
RBS	Rutherford backscattering
R_o	frequency or pre-exponential factor in reaction rate expression
RTA	rapid thermal anneal

RTS	ratio thin window
SAW	surface acoustic wave
SEI	secondary electron emission
SEM	scanning electron microscopy
STEM	scanning transmission electron microscope
T	temperature
tan δ	dissipation factor or dielectric loss
T_c	Curie point
TEM	transmission electron microscopy
$Ti(n\text{-}OC_3H_7)_4$	titanium n-propoxide
$Ti(OC_2H_5)_4$	titanium ethoxide or $Ti(EtO)_4$
$Ti(OC_4H_9)_4$	titanium tert-butoxide
TIP	titanium isopropoxide, $Ti(OC_3H_7)_4$
t_{min}	minimum twin thickness
T_o	Curie-Weiss temperature
V	applied voltage
V^*	volume of the critical nucleus
V_{pp}	voltage peak-to-peak
XRD	x-ray diffraction
Z	atomic number
ZAF	atomic number absorption fluorescence
α	grazing incidence angle in radians
α_c	critical angle

γ^T	twinning shear
Δ	$\alpha^2 - \alpha_c^2$
ΔG^*	initial free energy
ΔG_V	free energy difference between the vapour and condensed phases
γ_{SV}	surface energy of the nucleus
Δ_V	volume change
ϵ	dielectric response (or permittivity) or strain as appropriate
ϵ_o	permittivity of free space (8.85×10^{-12} C $V^{-1}m^{-1}$)
η	susceptibility
λ	wavelength of x-rays or electrons
μ	x-ray linear absorption coefficient in cm^{-1}
ρ	resistivity (Ω-cm) or density ($g\text{-}cm^{-3}$) as appropriate

1.0 INTRODUCTION

During the last decade, the use of ferroelectric (FE) material for random access memory (RAM) elements has reached commercial applications in the semiconductor industry, to the extent that companies started production of 4 Kbyte (to 64 Kbyte) memories in 1993 [Huffman]. These memory elements are non-volatile, compact, programmable with five volts with 250 ns access time and 10^8 cycle endurance. This non-volatile technology has the potential to replace any or all memory cells with one standard cell. Both non-volatile and dynamic access memories (DRAM) are under development. It is sufficient to say here that the former relies on the material's ferroelectric properties, while the latter utilizes the high dielectric property. (Further discussion of memory applications is given in §2.2.) Northern Telecom undertook and supported work in this area for implementation in next-generation memory devices in the telecommunications industry.

Deposition of $PbTiO_3$ and/or PZT thin films has been achieved by several methods (see §2.3). Commercially available devices employ a sputtered lead zirconate titanate ($Pb(Zr,Ti)O_3$ or PZT) film [Huffman 1991]. A significant amount of research has been devoted to the sol-gel method [Yi et al. 1988, Payne et al. 1989, Parikh et al. 1990] due to its low start-up cost and the relative ease of preparing films. Chemical vapour deposition (CVD) is however the most promising technique for producing the thin films useful for integrated circuit fabrication and also, CVD films are known for their conformal coverage which expands the device structures possible in implementation [Emesh, Calder, Ho, Jolly and Madsen 1994; Calder, Ellul, Emesh and Madsen 1993].

This work deals with the deposition and characterization of titanium oxide, lead oxide and lead titanate ($PbTiO_3$) thin films. The film deposition technique employed was metalorganic chemical vapour deposition (MOCVD) using a low pressure CVD horizontal reactor. The influence of deposition conditions on material properties, and the optimization of characteristics favourable for capacitor structures to application in memory devices were examined. The process development entailed the exploration of deposition parameters, such as substrate temperature, chamber and vapour pressures, whilst investigating the effect of temperature and duration of post deposition rapid thermal annealing. The use of different electrode materials was also studied. The relationship between the processing conditions, composition and structure was examined. To achieve these goals, analytical techniques were used to investigate film quality and characteristics such as thickness, composition, structure, interfacial properties and growth patterns. The remaining task was to measure the electrical properties and correlate them to the film characteristics and hence make the link to the deposition parameters and annealing conditions for specific electrode materials. The electrical characteristics of primary interest are: remanent polarization (P_r), coercive field (E_c), spontaneous polarization (P_{sp}), saturation polarization (P_s), permittivity or dielectric response (ϵ), resistivity (ρ), dissipation factor or dielectric loss ($\tan \delta$) and the effects of fatigue and aging.

Results in this field in achieving the desired electrical characteristics has been impeded by ferroelectric thin film quality, choice of electrode materials, and insufficient investigation and understanding of the physical properties. With increased knowledge on compatible materials for electrodes, high quality films and in-depth characterization, this vital link to the electrical parameters can be made.

The relationship between the physical and electrical properties of the $PbTiO_3$ films formed an essential base for process development and future optimization. The characterization of these films was crucial for understanding the impact of the deposition parameters on film properties and obtaining the best properties for semiconductor applications. As the overall knowledge in this field for such an application is still maturing, optimizing the film properties is often hindered by the lack of definition of a "standard film".

PZT is one of the favoured FE materials for memory applications in the semiconductor field. The simpler material, $PbTiO_3$, was studied here due to time constraints and the complexity of the PZT deposition process. Due to its lower dielectric constant, $PbTiO_3$ is not as suitable a material for semiconductor applications as PZT, but it is still ferroelectric and can be subjected to the same electrical tests. It is thought that a good understanding of the $PbTiO_3$ deposition process would allow a process for the more complex PZT material to be developed more easily. Indeed the literature suggests that the development of an $PbTiO_3$ process almost always precedes the PZT process development by a minimum period of one to two years [Okada et al. 1988 & 1990, de Keijser et al. 1991 & 1993, Kwak et al. 1988 & Erbil et al. 1992].

Understanding of less complex oxides, such as TiO_2, lead oxides and $PbTiO_3$, may prove to be important in understanding degradation effects (fatigue) apparent with device operation. There has also been some indication of enhancement in growth characteristics of PZT through the use of seed layers of $PbTiO_3$ [Shimizu et al. 1993, Yoo et al. 1993, Chandler et al. 1993].

The main thrust of this project involved a critical analysis of the factors affecting deposition, through theory and experimentation, and related the growth processes to the structural and electrical properties of the material. Examination of microstructural defects, domain characteristics, and interfacial properties was carried out to further the understanding of degradation effects within lead titanate type materials. Obtaining reproducible properties in FE films involves the ability to characterize deposited films and relate the salient aspects of film composition, bonding and microstructure to the deposition conditions [Roy et al. 1990].

2.0 FERROELECTRIC MATERIALS

Crystals can be classified into seven systems: cubic, orthorhombic, rhombohedral[*], tetragonal, hexagonal, monoclinic and triclinic. These systems can be further sub-divided into 32 point groups (crystal classes) with 21 of them being non-centric (that is, without a centre of symmetry). Ten of these classes are called polar because they have a finite and permanent value of polarization, known as spontaneous polarization, in the absence of an applied field or stress [Burfoot and Taylor 1979]. Ferroelectrics (FE's) are a subset of this last group where the crystal's direction of spontaneous polarization is reversible by application of an electric field.

Perovskites, so called because of the mineral perovskite, $CaTiO_3$ (a distorted perovskite structure) named after Count L.A. Perovski of St. Petersburg (Leningrad) [Deer et al. 1962] form one group of FE material. Many perovskites however do not exhibit FE behaviour and some are actually anti-ferroelectric in character [Lines and Glass 1977]. The perovskite structure has the general formula ABO_3, Pm3m, space group 221 [Lines and Glass 1977]. It is cubic with the A atoms at the cube corners, B atoms at the body centres, and the oxygen atoms at the face centres (figure 1). Most perovskite compounds are slightly distorted and hence have lower symmetry than Pm3m. Some of the structural modifications that may be present

---

[*] also referred to as trigonal

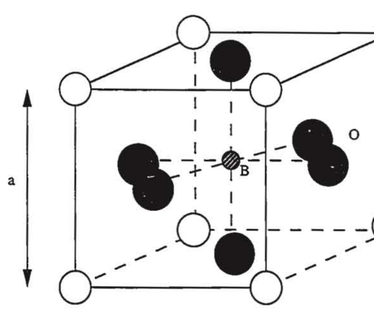

Figure 1: The cubic ABO_3 perovskite structure

are: a doubling of the basic unit cell, orthorhombic, tetragonal (c/a > 1 or pseudo tetragonal c/a < 1), and rhombohedral structures [Roth 1957]. These departures from the cubic structure result in dielectric and magnetic properties including ferroelectricity.

2.1 Properties

The fundamental behaviour and characteristics of an FE material can be described in terms of a capacitor. The relationship between the polarization and electric field is represented by a hysteresis loop (figure 2). Initially, the net macroscopic polarization can be zero and the overall electric dipole direction random. Regions where the dipoles are aligned are called domains. Upon application of a field, the domains will grow and eventually reach maximum alignment when polarization saturation, P_s, is reached (figure 3). In general, only easy directions are polarized into domains. The direction of P_s is called the polar axis (figure 3) [Hench and West 1990]. If the field is removed some dipoles will remain aligned giving a remanent polarization, P_r. To reduce the polarization to zero, a coercive field, E_c must be applied in the opposite direction.

The spontaneous polarization usually decreases with increasing temperature and disappears continuously, or more often discontinuously, at a Curie point T_c. Above the Curie point, the approaching transition is often signalled by a diverging dielectric response or permittivity ϵ, which close to T_c varies in a Curie-Weiss manner (eqn. 2.1):

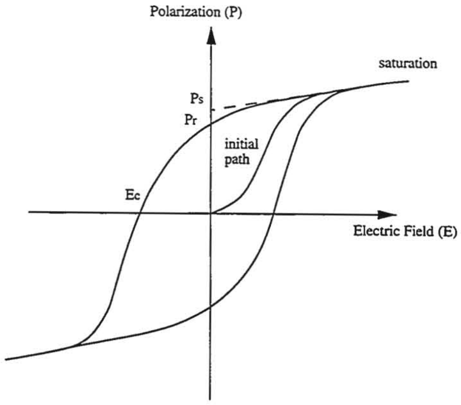

Figure 2: Schematic diagram of an FE hysteresis loop [Jona and Shirane 1962]. Ps is the spontaneous polarization, Pr, the remanant polarization and Ec, the coercive field. Dielectric displacement is related to polarization by: $D = \varepsilon_0 E+P$ where ε_0 is the dielectric of free space.

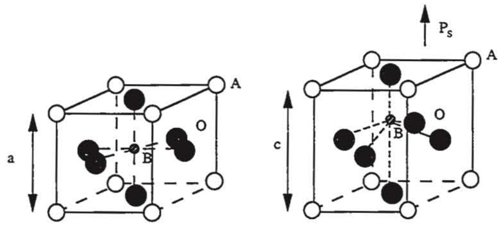

(a) (b)

Figure 3: The two forms of $PbTiO_3$: (a) the cubic and non-ferroelectric form and (b) the tetragonal and ferroelectric form. a and c are lattice parameters where c > a. Ps indicates the direction of the spontaneous polarization [Johnson 1989].

$$\epsilon = C_T / (T - T_o) \qquad (2.1)$$

where C_T is a constant, T_o is the Curie-Weiss temperature equal to T_c for the case of a continuous transition.

2.2 Memory Applications

Numerous ferroelectric materials have been recognized since the initial discovery of ferroelectricity in 1921 [Lines and Glass 1977]. The following characteristics are desirable for FE thin films for memory device applications: rectangular hysteresis loop, low coercive field, large remanent polarization, fast and non-degraded switching, long period of retention, and compatibility with semiconductor integrated circuit technology [Ramakumar et al. 1990]. Five materials or groups of materials have been identified as most promising for switching applications [Scott 1989], namely, potassium nitrate KNO_3, bismuth titanate $Bi_4Ti_3O_{12}$, PZT compounds, lead germanate $Pb_5Ge_3O_{11}$ and lithium niobium and lithium titanate compounds $Li(Nb,Ti)_2O_6$.

Much attention has been given to the use of FE material, mostly perovskites, in DRAM and non-volatile memory cells. Non-volatile devices retain their polarization state and hence the stored information for an indefinite period of time after the removal of voltage from the circuitry. Application of FE materials in DRAMs has also been examined since the higher dielectric constants offered by FE materials allow for greater packing densities in these simple charge-storage cells [Parker and Tasch 1990]. As the area available per memory cell decreases for

greater packing densities, these simple charge-storage cells require the higher dielectric constants offered by FE materials.

To form a non-volatile memory cell, a capacitor structure using FE material as the dielectric, is situated over the semiconductor layers normally used for a metal-oxide-semiconductor field-effect transistor (MOSFET) (figure 4). The FE capacitor requires three additional masking-steps and hence a knowledge of deposition, anneal and etch characteristics of each layer is required. The FE capacitor shown (figure 5), can be used as a shadow random access memory (RAM), that is, as a back-up during power failure. A four transistor static RAM cell is interconnected with two FE capacitors where the capacitors are only activated to store data upon loss of power and restore data upon regaining power.

Thin films less than 1 μm in thickness are required if the standard 5 V operation of the integrated circuitry is to be used and the following complications may be introduced:

1. stability of the FE phase is changed because the physical dimensions are reduced,
2. surface effects are introduced arising from incomplete neutralization of depolarizing fields (when the polar axis is perpendicular to the film) and space-charge fields arising from energy-band bending normal to the film surface,
3. departures from stoichiometry (representing a larger volume fraction in thin films) usually result in decreased dielectric constant and increased loss as a function of frequency,

and

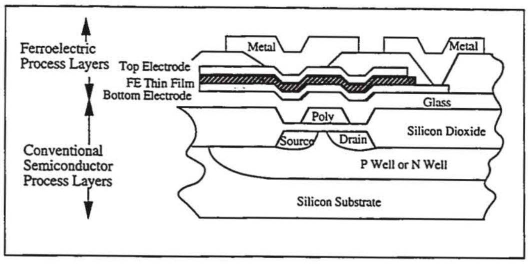

Figure 4: A thin film FE memory capacitor is created by forming a sandwich of metal electrodes and FE material on traditional Complementary Metal Oxide Semiconductor (CMOS) technology [Bondurant and Gnadinger 1989].

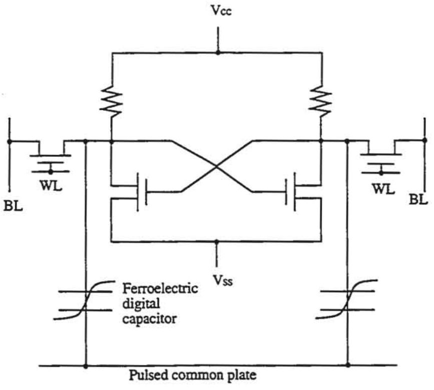

Figure 5: Schematic drawing of shadow RAM layout using four transistors and two FE capacitors (Application note)

4. interfacial polarization effects appear in polycrystalline films [Lines and Glass 1977].

The polycrystalline nature of these films introduces further complexities as second phase particles can form at the grain boundaries and act as sinks for defects. Furthermore, grain size affects switching mechanisms [Martirena and Burfoot 1974], mechanical stability [Matsuo and Sasaki 1966] and cracking tendencies [Weaver, Madsen and Griswold 1991] of the material. For bulk samples, reversal of the polarization direction (switching) can occur through nucleation and domain wall motion (or growth) of new domains or by the growth of existing domains [Jona and Shirane 1962]. For small grains, the domain wall thickness can be of the same order of magnitude as the grains and then the grains will be either single domains or will contain very few non-mobile walls [Martirena and Burfoot 1974].

Additional requirements are placed on these thin films in terms of the contacting materials and this issue is addressed in more detail in §2.6. The deposited FE material should have the minimum porosity and number of defects and pinholes, and be continuous over the underlying device topography. Several manufacturing and operational conditions may be placed on the material depending on the specific application. The work described herein focuses on memory applications with $PbTiO_3$.

2.3 Deposition Methods

Deposition of PZT thin films has been achieved by electron or ion beam deposition [Castellano 1980, Oikawa and Toda 1976], sputtering techniques [Croteau et al. 1987, Croteau and Sayer 1986, Sviridov et al. 1985, Shintani et al. 1978], sol-gel methods [Payne et al. 1989, Yi et al. 1988], laser ablation [Saenger et al. 1990, Ramakumar et al. 1990, Chiang et al. 1990] and CVD [Ainger et al. 1990, Okada et al. 1990, Kavanaugh and Williams 1989]. The approach in each method is to deposit thin films directly rather than work from polished, expensive bulk ceramics [Brierley et al. 1987]. Sputter-deposited films can suffer from the following problems: the deposition rate is low [Okada et al. 1990, Kavanaugh and Williams 1989], the composition is difficult to control because of sputter variation with elements [Okada et al. 1990], defects and damage are generated at the substrate surface due to the sputtering itself [Okada et al. 1990], the apparatus is expensive [Kavanaugh and Williams 1989], and a variation in film composition occurs across the deposited film [Kavanaugh and Williams 1989]. Although configurational changes have nearly eliminated the sputter damage problem and improved composition control [Roy et al. 1990], the other issues mentioned above remain. The quality of films grown by sol-gel or metal organic decomposition (MOD) techniques are limited because cracking can occur during the drying and firing stages as pyrolysis and subsequent loss of organics occurs and the film shrinks [Kavanaugh and Williams 1989]. Films free of macroscopic cracking tend to be porous from loss of organics present in the initial solvents. With laser ablation it is difficult to produce films with sufficiently large uniform areas for memory devices. Overall, no technique is without fault (Table I) [Roy et al. 1990], however, progress in the CVD area in the past has suffered primarily from a lack of suitable precursors [Brierley et al. 1987]. If this and other problems can be overcome, CVD potentially has the uniformity, composition control, high deposition rates [Kwak et al. 1988], step coverage, purity and density [Yoon and Kim 1988] needed in industry.

Table I : Advantages and Disadvantages of Various Deposition Techniques

Method	Rate nm-min^{-1}	Epitaxy^{a} 1-10	Stoichiometry^{a} 1-10	Wet/Dry^{b}	Temperature (C)^{c} Substrate	Anneal	Memory Devices	Cost^{d}	Miscellaneous Problems
RF Sputter	0.5-5	8	3	D	RT-700	500-800	✓	H	Negative Ions
Magnetron sputter	5-30	5	5	D	"	"	✓	H	Target Surface
RF Magnetron	5-10	9	5	D	"	"	✓	H	
Ion Beam Sputter	2-100	9	8	D	"	"	✓	H	Uniformity
Evaporation	10-100	7	4	D	"	"	✓	H	Rate Control
Laser Deposition	5-100	9	6	D	"	"	x	H	Debris, Uniformity
Sol-Gel	100^{e}	2-8	9	W	RT	450-800	✓	L	Multiple coating
MOD	300^{e}	2	9	W	RT	500-800	x	L	High T_{anneal}
MOCVD^{f}	5-100	5	7	D	400-800	600	✓	H	High $T_{substrate}$

a: 1 for best to 10 for worst
b: W for wet and D for dry
c: RT for room temperature
d: H for high and L for low
e: nm per coating
f: since 1990 many of the limitations noted by Roy et al. have been overcome or reduced.

2.4 Chemical Vapour Deposition (CVD)

CVD may be defined as the material synthesis method for the formation of a non-volatile solid film on a substrate by the reaction of vapour phase chemicals that contain the required constituents. The reactant gases are introduced into a chamber, decomposed and reacted at or close to a heated surface. This process can be broken down into a sequence of steps (figure 6):

(i) mass transport in the bulk gas flow region from the reactor inlet to the deposition zone.

(ii) gas phase reactions leading to the formation of film precursors and byproducts,

(iii) mass transport of film precursors to the growth surfaces,

(iv) adsorption of film precursors to the growth surface,

(v) surface diffusion of film precursors to growth sites,

(vi) incorporation of film constituents into the growing film,

(vii) desorption of byproducts of the surface reactions, and

(viii) mass transport of byproducts in the bulk gas flow region away from the deposition zone towards the reactor exit [Jensen 1993].

The chemical reaction is the essential characteristic of CVD which

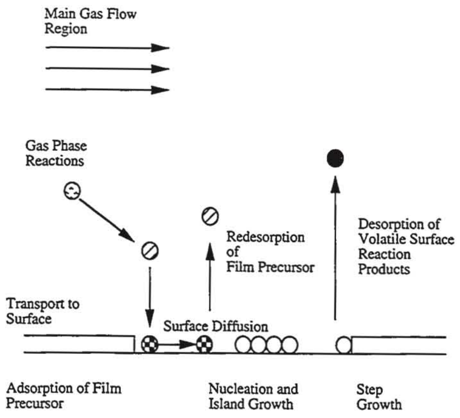

Figure 6: Schematic drawing illustrating the transport and reaction process underlying CVD [Jensen 1993].

distinguishes it from physical deposition processes. Typical chemical reactions are pyrolysis, reduction, oxidation, hydrolysis, nitridation, carbonization, disproportionation, synthesis and combined reactions [Kern and Ban 1978]. The fundamental reaction pathways and kinetics involved in CVD processes are only well understood for a few commercially important systems, such as silicon deposition [Jensen 1993]. Thermodynamics can be used to predict the likelihood of a given reaction, and calculate the theoretical efficiency of the reaction and partial pressures of all vapour species for a given set of conditions. This approach, however, assumes chemical equilibrium which does not normally prevail in flow reactors. To obtain information on the rate of these reactions, kinetics must be used. The free energy of some reaction ΔG_r° can be calculated by subtracting the summation of the standard free energy of the reactants from those of the products:

$$\Delta G_r^\circ = \Sigma \Delta G_f^\circ \text{ products} - \Sigma \Delta G_f^\circ \text{ reactants} \qquad (2.2).$$

ΔG_r° can in turn be related to the equilibrium constant k_p and related to the partial pressures (P_i) in the system:

$$-\Delta G_r^\circ = 2.3\ RT \log k_p \qquad (2.3)$$

$$\text{where } k_p = \Pi^n_{i=1} P_i \text{ products} / \Pi^n_{i=1} P_i \text{ reactants} \qquad (2.4).$$

Determining the likely reaction in a system can be found by one of two methods [Kern and Ban 1978]. The first method looks at the minimization of the free energy with respect to the degree of completion of a reaction. The second approach is to solve a set of simultaneous nonlinear equations to find the partial pressures of all species present and then use this information to determine the total quantity of a species in the vapour phase. This method involves specifying the equilibrium constant for each reaction likely to occur, in terms of the partial pressures and activities for each compound in the reaction expression. Variations of parameters can be modeled with a computerized system and the optimal parameters for a CVD system found.

In practice, good quality films result from chemical reactions which are usually heterogeneous and take place at the substrate surface. Conversely a homogeneous reaction characterized by a dominance of gas phase reactions results in clusters of the deposit and subsequently poorly adhering, porous films with numerous defects [Wolf and Tauber 1986]. Furthermore some homogeneous reactions may consume reactants excessively and lead to decreased deposition rates.

The overall deposition sequence is composed of gas-phase and surface processes. The surface process may be a thermally activated phenomenon where the reaction rate is given by:

$$R = R_o \exp(-E_a/kT) \qquad (2.5)$$

where R_o is the frequency or pre-exponential factor, E_a is the apparent activation energy in eV, k is Boltzmann's constant (8.6×10^{-5} eV/K) and T is the temperature in Kelvin. A process is said to have Arrhenius behaviour if a plot of ln R against 1/T produces a straight line since E_a must then be temperature independent.

Typically the temperature dependence of a CVD deposition process can be divided into two regions each having a different slope determined by the slowest (and hence controlling) mechanism. When the temperature increases such that the reaction rate surpasses the rate at which species arrive at the surface, the reaction is mass transport limited (figure 7) [Wolf and Tauber 1986]. At low temperatures on the other hand, the surface reaction rate is reduced and the arrival of reactants exceeds the consumption rate, and hence the process becomes reaction rate limited. The overall growth rate of a CVD layer is controlled by a combination of these two processes (figure 8) [Hitchman and Jensen 1993].

Generally, the number of different molecules required to come together to react indicates the order of the reaction [Cottrell 1968]. Reaction orders are usually first or second order. Often reactions which are apparently higher order can be broken down into a sequence of steps where the order of the slowest step occurring determines the actual overall reaction order [Cottrell 1968]. An exception to this rule is found if a reactant has such a low concentration that the rate of the reaction is determined effectively by its concentration only [Cottrell 1968] and in turn, the order of the reaction may appear to change. Examination of the dependence of the deposition rate with pressure can reveal the order governing a CVD reaction.

The rate determining step in the deposition process is the slowest step involved. For example the rates of reactions might vary with temperature or substrate orientation [Kern and Ban 1978]. Changes in the temperature dependence with growth rate indicate different steps are controlling the deposition rate. For instance, at low temperatures weak adsorption of the reactants on the substrate surface might dominate, while at high temperatures, the diffusion of reactants and products to and from the reacting surface might govern the rate of the reaction. Substrate variations,

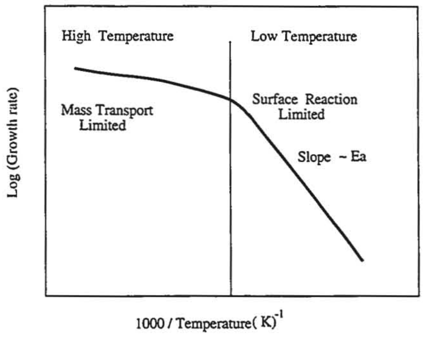

Figure 7: Temperature dependence of growth rate for CVD films [Wolf and Tauber 1986.].

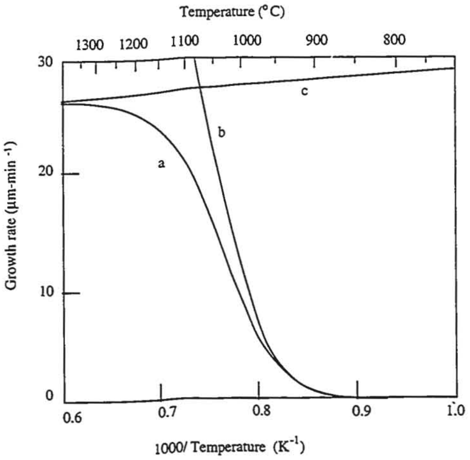

Figure 8: Overall growth rate (a) is a result of kinetically controlled growth (b) and transport controlled growth (c) [Hitchman and Jensen 1993].

such as the densities and geometric arrangements of surface sites, the number and nature of surface bonds, the composition of various crystallographic surfaces, and the nature and number of surface features (steps, kinks, vacancies, etc.) affect the deposition rate.

Most of the transport phenomena, e.g. fluid flow, heat transfer, and mass transfer, are intimately tied to the system design. A typical experimental system for CVD can be divided into three regions: precursor handling, the reaction chamber, and exhaust of by-products. Precursors are usually selected by factors such as their ease of handling (room temperature and pressure utilization), safety, cost and availability, and purity of deposit. Metalorganic chemicals are often liquid or solid at ambient conditions, and then higher temperatures and/or lower pressures along with a carrier gas must be used. As the carrier gas (usually an inert gas) bubbles through the precursor, it picks up vapour which is subsequently carried into the reactor. Care must be taken with additional heating of this type of gas distribution network to ensure condensation does not form in the reactor delivery lines. Relatively little has been published about gas handling [Hitchman and Jensen 1993] and the current tendency is to buy commercial systems or learn through experience. The precursor, whether a major reactant or a dopant, should have a vapour pressure in the range of 1 to 10 Torr in the temperature range -20°C to 40°C and thermally decompose at a temperature in the range of 300-500°C [Moon and Huong 1993].

Reactors can be divided into hot wall and cold wall systems. Hot wall reactors are usually tubular in form and heating is often accomplished by resistance

elements surrounding the reactor tube [Kern and Ban 1978]. The use of temperature gradients or uniform heating, in combination with various wafer arrangements and gas distribution systems are employed to obtain reproducible and uniform films. These systems can suffer from build-up of deposit on the walls which can lead to subsequent flaking and wafer particulate control problems, but more importantly, serious precursor depletion effects can make deposition rates low and unreliable. For cold wall reactors, the susceptor is the only intentionally heated area and this is usually done through radio-frequency heating or high intensity radiation lamps; resistance heated graphite slabs are rarely used as they are reactive with oxygen [Kern and Ban 1978].

CVD can be performed at atmospheric or reduced pressure (typically 0.25 to 2 Torr) and is commonly referred to as low pressure CVD (LPCVD) [Wolf and Tauber 1986]. Other benefits may be obtained (depending on reactor geometry) from a pressure reduction, such as, increased throughput due to high packing density of substrates allowed because of the reaction rate limitations rather than mass transport control. Significant decreases in pressure may only result in slight decreases in deposition rate [Hitchman and Jensen 1993]. Often slightly higher deposition temperatures, 550-600°C are used to boost the deposition rate. Reduced pressures are technologically advantageous for many commercial processes.

For very low temperature deposition (down to 20°C), photo induced (or enhanced) processing is sometimes used. This method uses high energy, high intensity photons to either heat the substrate surface or to dissociate and excite reactant species in the gas phase [Wolf and Tauber 1986]. In the former case, the reactant gases are transparent to the photons and gas-phase reactions are thereby eliminated [Wolf and Tauber 1986]. In the latter case, the energy of the photons can be chosen such that the energy transfer to the reactant molecules (or to a catalytic intermediary) is efficient. Films from photo-induced CVD give good step coverage but may suffer from low density and molecular contamination as a result of the low deposition temperature [Wolf and Tauber 1986].

The variables for deposition of a simple (2 component) oxide are source temperature, substrate temperature, partial pressures of the O_2 and the liquid source, total flow, deposition duration and system pressure. The source temperature needs to be sufficiently high to produce a vapour, but must be lower than the substrate temperature. The latter temperature usually ranges from 200 to 800°C in the semiconductor industry, with low temperatures (<450°C) being more desirable, especially if Al alloys have already been deposited (since Al forms hillocks at elevated temperatures [Wolf 1990]). The flow rate of the carrier should be as high as possible (in order to increase the deposition rate) without resulting in liquid formation in the gas lines. The total flow obtained by the combination of the carrier gas, O_2, and an inert gas, such as Ar or N_2 used to control the vapour pressure of the liquid source reactants and increase the pressure of the system is limited by the dilution effect. System pressure can be varied, within certain ranges as allowed by the total flow in the system, by adjusting the throttle valve. The above seven variables are easily reduced by fixing the duration of the deposition to a reasonable value and selecting a total flow which allows pressure adjustments from 500 mTorr to 3 Torr. The partial pressure is related to the system pressure (p_{total}) and flow rates (F) as follows:

$$p_x = p_{total} \cdot F_x / (F_{total} + F_x) \qquad (2.6)$$

where x is the component of interest.

Increases in the partial pressure of the liquid yield higher deposition rates since more vapour is incorporated into the gas stream. An upper limit is placed on this when the saturation point is reached.

Properties which are important in the deposited films include the thickness, adhesion, porosity, chemical purity, structure and composition. The films with the best characteristics are usually epitaxial, that is, they have regularly oriented growth which is aligned in some way to the substrate. When the substrate is of the same material, this alignment is called homo-epitaxy; otherwise, it is called hetero-epitaxy. Strain caused by lattice mismatch between the substrate and grown film is accommodated in various ways according to the film thickness. For thin films, misfit is accommodated by elastic strain with no dislocations. For very thick films, accommodation is totally by dislocations and not by elastic strain. For intermediate thicknesses both elastic strain and dislocations relieve the misfit. Another way of dealing with strain is to use graded layers such that the mismatch from one atomic layer to the next is reduced. This can be accomplished by changing the composition of the film gradually. Epitaxial films can only be obtained when good lattice matching, and the proper temperature range and reactant concentrations are used. For many applications, amorphous or polycrystalline films are deliberately formed to exploit their unique characteristics. In general, lower temperatures and higher gas phase concentrations favour the formation of polycrystalline deposits. Under these conditions the arrival rate at the surface is high, but the surface mobility is low [Kern and Ban 1978]. As the temperature is reduced, an increase in supersaturation results in more nuclei and consequently a finer grained film is formed. At even lower temperatures an amorphous film, without crystallites, may be formed. Growth rates for amorphous films are usually quite high, while epitaxial growth is considerably slower.

An understanding of the structure of films, whether they be polycrystalline, amorphous or epitaxial, may be gained through examination of film growth aspects. The nucleation process can be described in free energy terms [Porter and Easterling 1981]. The driving force for the reaction is provided by the free energy difference (ΔG_V) between the vapour and condensed phases, while the interfacial energy term opposes the reaction. Above a critical nucleus size,

$$r^* = 2\,\gamma_{SV} / \Delta_V \qquad (2.7)$$

where γ_{SV} is the surface energy of the nucleus (assumed to be isotropic), continued growth of the solid phase is favoured. The initial free energy (ΔG^*) is provided by thermal activation,

$$\Delta G^* = \tfrac{1}{2}\, V^*\, \Delta G_V \qquad (2.8)$$

where V^* is the volume of the critical nucleus.

The types of growth observed in CVD films are mainly characterized by one of three models [Jensen 1993]. In the Volmer-Weber model, three-dimensional island growth occurs where small clusters are nucleated on the surface. As the film atoms are more strongly bound to each other than to the substrate, the islands continue to grow and then eventually coalesce and form a continuous film. In the Frank-van der Merwe model, two-dimensional layer-by-layer growth occurs as the film atoms are equally or less strongly bonded to each other than to the substrate. This model applies to homo-epitaxial growth on clean substrates. The presence of impurities can give rise to three-dimensional island growth [Joyce 1974]. The Stranski-Krastanov growth mode or layer followed by island growth combines the previous two. After the growth of one or two monolayers, layer growth is no longer favoured and islands form on the top of the initial layers. The factors which control this transition from two-dimensional to three-dimensional growth are not well understood.

2.4.1 Titanium Oxide

Titanium oxide films can be deposited from Ti alkoxides, in particular from titanium isopropoxide (TIP), (written as $Ti(OC_3H_7)_4$ or $Ti(O.i\text{-}Pr)_4$) (figure 9). This compound has a vapour pressure of 80 mTorr at 20°C [Siefering and Griffin 1990b] which varies with temperature according to the following expression:

$$\mathrm{Log}_{10}P = 9.837 - 3193.7 \times T^{-1} \qquad (2.9)$$

where P is the pressure in Torr and T is the temperature in K.

The reaction in forming an oxide from TIP is thought to consist of three elementary steps: (i) activation of a gas phase TIP molecule by vibrational excitation through a collision with a second molecule, perhaps involving loss of alkoxides groups; (ii)

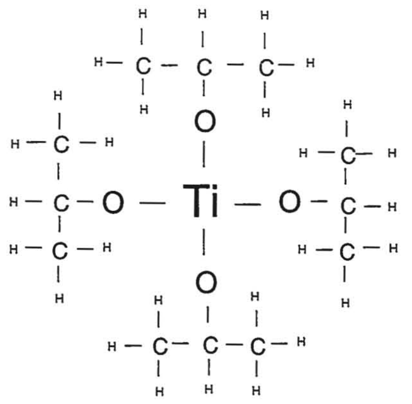

Figure 9: TIP structure [Itoh 1991].

adsorption of the activated TIP molecule at the surface; and (iii) decomposition of the remaining alkoxide groups in the adsorbed TIP molecule to produce TiO_2 [Siefering and Griffin 1990a]. A bimolecular gas-phase collision is thought to be the rate limiting step under the conditions studied by Siefering and Griffin [1990a and 1990b]. The deposition parameters used for the production of TiO_2 in a number of different studies are listed in Table II. No information is offered by Siefering and Griffin [1990] about the proposed TIP intermediate or the pathway for its formation. However, in the studies by Okada and his colleagues [1988], the following overall (simplified) reaction:

$$Ti(i\text{-}C_3H_7O)_4 = TiO_2\ (ad) + 4C_3H_6 + 2H_2O \tag{2.10}$$

based on pyrolytic decomposition, is proposed. A log-log plot of the pressure versus growth rate indicates that the process was zero order at 220°C and second order at 300°C [Siefering and Griffin 1990]. From the kinetic rate expression (eqn. 2.5), the apparent activation energy for low pressures (<0.15 Torr) was 35 $kJ\text{-}mol^{-1}$ which varied continuously to 150 $kJ\text{-}mol^{-1}$ at 2 Torr [Siefering and Griffin 1990a]. Another study found the apparent activation energy to be 53 $kJ\text{-}mol^{-1}$ at 6 Torr [Okada et al. 1989] and 75 $kJ\text{-}mol^{-1}$ at atmospheric pressure [Okada et al. 1988]. The deposition of TIP with different ambients: H_2O saturated N_2 [Sladek and Herron 1972], N_2 [Siefering and Griffin 1990a], N_2/O_2 [Okada et al. 1988], O_2 [Okada et al. 1989], tetraethoxysilane [Aitchison et al. 1992] and in the absence of a carrier gas [Siefering and Griffin 1990b] has been examined. It is difficult to draw clear conclusions from these studies because changes in reactor geometries and conditions have significantly affected the results. One study showed a large increase in growth rate with the substitution of O_2 for an inert gas [Sladek and Herron 1972], while others [Okada et al. 1988, 1989] observed no appreciable change. Siefering and Griffin's work [1990a,b] appears to delve most deeply into the fundamental kinetics and they found that N_2 as a carrier gas compared with deposition in the absence of a carrier gas, reduced the efficiency of the system thereby causing a drop in deposition rate. The study by Aitchison and his colleagues [1992] was more complicated since TIP had an apparent catalytic effect on the tetraethoxysilane also leading to the deposition of SiO_2 in addition to TiO_2.

Table II: Deposition parameters for TiO_2

System Pressure (Torr)	Substrate Temperature (°C)	TIP Temperature (°C)	Reference
.0023	**400-650**	60	Aitchison et al. 1993
0.04-2	**220-300**	20	Siefering & Griffin 1990a
5	**300**	**40-145**	Siefering & Griffin 1990b
6	**300-600**	**25-35**	Okada et al. 1989
760	150	75	Fitzgibbons et al. 1972
760	**300-700**	50-70	Okada et al. 1988

Bold type refers to overlap of deposition parameters with those used in this study, see § 4.1.

Titanium forms several different oxides as indicated in the phase diagram (figure 10) [ASM 1989]. At high oxygen compositions (O > 66.7%), TiO_2 forms, often with the rutile structure [Cotton and Wilkinson 1980]. However, TiO_2 has five polymorphs: anatase and brookite (usual low temperature and pressure forms), TiO_2-II and TiO_2-III (formed from anatase or brookite under pressure) as well as rutile (usual form at all temperatures and ambients) [ASM 1989].

Between 400 and 600°C films deposited by CVD were anatase, while those deposited at 650°C showed some evidence of the rutile phase [Aitchison et al. 1992]. Films deposited at higher temperatures have been shown to have a finer grain structure [Aitchison 1992] and a greater likelihood of being deposited as rutile. A variation in structure has also been observed with film thickness: for example Siefering and Griffin [1990a] reported that the initial films were amorphous or microcrystalline while at greater thicknesses anatase with a preferred (220) orientation was observed; the thickest films were rutile. The studies listed in Table II vary widely in terms of their deposition parameters (as well as in their deposition system configurations and ambient atmospheres) which can be expected to affect the structure (morphology and phase) of the films significantly. Other studies have found a combination of substrate heating and annealing was necessary for growing rutile films [Wicaksana et al. 1992].

According to Fitzgibbons and his colleagues [1972], anatase and brookite transform irreversibly to rutile on heating. From sputter deposition and annealing of TiO_2 thin films, it was suggested that over the range of 200-400°C anatase is the

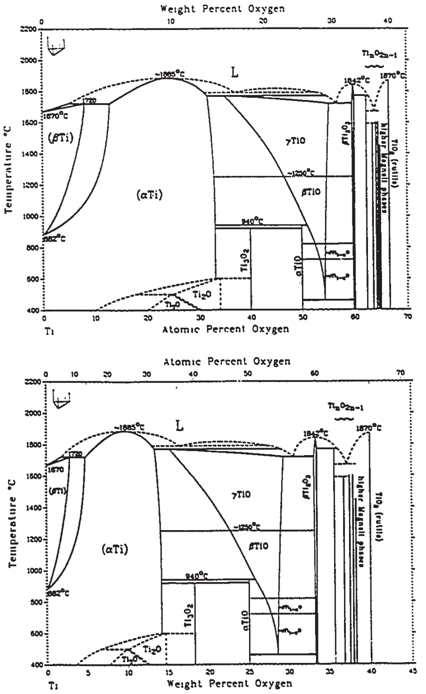

Figure 10: TiO_2 Phase Diagram [ASM 1989].

preferred phase and rutile may be in a metastable state [Wicaksana et al. 1992]. In one study, annealing at temperatures of 800°C or greater caused the transformation of CVD anatase thin films to rutile [Wang et al. 1970]. Conversely, another study of low temperature sputtered TiO_2 films showed an anneal at 850°C did not completely transform the films into the rutile phase [Wicaksana et al. 1992].

However despite the experimental evidence for rutile, thermochemical data indicates that anatase is 8 to 12 kJ-mol^{-1} more stable than rutile at room temperature [Cotton and Wilkinson 1980]. On the other hand, Mitsuhashi and Kleppa [1979] have suggested that anatase and brookite are not stable at any temperature [ASM 1989]. From the contradictions presented in the literature, it is apparent that the relationship between anatase and rutile is not well understood.

2.4.2 Lead Oxide

The earliest studies of lead oxide were done primarily with powder and single crystal samples [White et al. 1961, Abadir et al. 1976, Adams and Stevens 1977], while more recently thin film work, usually as one of the development steps in a $PbTiO_3$ process has been undertaken [Okada et al. 1988 & 1989, Greenwald et al. 1992]. Many different forms of lead oxide exist as Pb can adopt either a 2^+ or 4^+ valence state [Cotton et al. 1987]. Lead oxides, PbO, $PbO_{2\pm0.2}$, Pb_2O_3 and Pb_3O_4 (known as red lead or minium), exist in at least 15 different crystal forms [JCPDS 1992].

Litharge, the low temperature form of PbO (which is also red in appearance) exists in equilibrium at 491±3°C [Adams and Stevens 1977] with massicot, the high temperature, yellow form of PbO. Litharge is tetragonal (P4/nmm, space group 129) with a=0.39729 and c=0.50217 nm, while massicot is orthorhombic (Pcam, space group 57) with a=0.54903, b=0.58920, and c=0.47520 nm. Below 200 K, α-PbO, which is orthorhombic (Cmna, space group 67) with the lattice parameters a=0.56085, b=0.56036, and c=0.49893 nm is stable. Commercial PbO is often a mixture of massicot and litharge [White et al. 1961]. When pure material exists, particularly in large crystals, the colour can be used for identification purposes [White et al. 1961]. Other researchers have also reported difficulties obtaining pure powder samples and have used specially grown crystals instead [Adams and Stevens 1977]. An early study [White et al. 1961] showed a complex phase relationship between massicot and litharge in terms of pressure, temperature and stability; however other researchers have shown massicot can be stable at ambient temperatures [Adams and Stevens 1977].

Lead oxide deposition can be produced by the oxidation of tetraethyl lead (PbEt or $Pb(C_2H_5)_4$) [Okada et al. 1988]. These workers showed that the deposition rate was controlled by the adjustment of the source temperature (0 to 30°C) and carrier flow rate (200 to 600 sccm). Higher source temperatures and carrier gas flow rates increased the deposition rate. PbO deposition started at 350°C and increased with temperature until 450 - 470°C. At higher temperatures the deposition rate was limited by the diffusion rate of reactant species to the substrate surface or by decreases in source concentration due to homogeneous nucleation in the vapour phase. The activation energy for PbEt oxidation was estimated to be 134 kJ-mol^{-1} irrespective of the concentration of the source gas. A further study examined the deposition of PbO at lower PbEt source temperatures of -15 to -25°C and higher substrate temperatures of 400 to 600°C at a reduced pressure of 6 Torr [Okada et al. 1989]. The apparent activation energy for the surface reaction controlled step was estimated to be 78 kJ-mol^{-1}. The decrease in the deposition rate observed at high temperatures in the atmospheric study was not evident at the reduced pressure. CVD of lead oxide exhibited selective deposition and could not be deposited on SiO_2 but did form readily on metallic surfaces [Greenwald et al. 1992].

2.4.3 Lead Titanate

Most of the precursors used in lead titanate $PbTiO_3$ (and PZT) CVD are metalorganic[*] in nature and hence the terms CVD and MOCVD can often be used interchangeably in this context. Normally a precursor for each element (e.g. Ti, Pb and O) is introduced separately, however some effort has been expended in using sol-gel solutions as a precursor for CVD with limited success [McMillan 1991].

The first publication on CVD $PbTiO_3$ thin films appeared in 1982 [Nakagawa et al]. The interest in this area rose significantly in the late 1980's (figure 11) with the development work on non-volatile memory devices. In 1990 the first documentation of a CVD PZT process appeared [Okada et al. 1990] and in 1992 lanthanum doped PZT (PLZT) by CVD was reported [Okada and Tominaga 1992].

---

[*] MOCVD is also written as OMCVD which corresponds to organo-metallic CVD

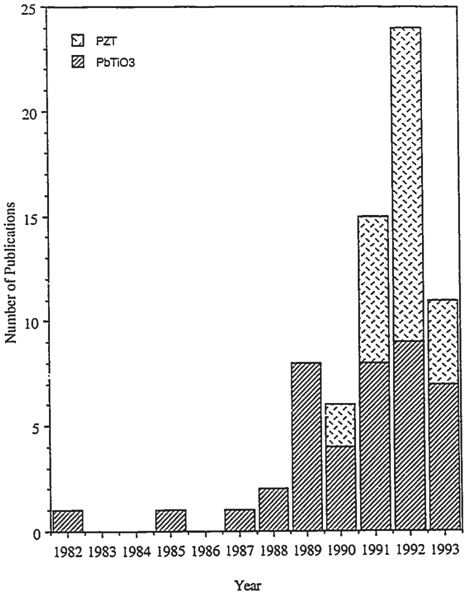

Figure 11: CVD publications on $PbTiO_3$ and PZT.

Numerous precursors have been used for $PbTiO_3$ and approximately half of the work has been done with TIP and PbEt (Table III).

Published work using tetraethyl lead and titanium isopropoxide to form $PbTiO_3$ indicate a range of deposition parameters (Table IV) [Okada et al. 1988, 1989; Kwak et al. 1988; Swartz et al. 1989; Shimizu et al. 1991; Dormans et al. 1991, 1992; de Keijser et al. 1991; Greenwald et al. 1992, Erbil et al. 1992, Chen et al. 1992, Katayama et al. 1992]. At atmospheric pressure some researchers have reported no success in forming lead titanate films [Kavanaugh and Williams 1989], while others have switched from atmospheric to reduced pressures to obtain an increase in the deposition rate [Okada et al. 1988 & 1989]. The growth of $PbTiO_3$ from TIP and PbEt has been described qualitatively by eqn. 2.10 for the formation of TiO_2 and by the following reactions [Dormans et al. 1991]:

$$Pb(C_2H_5)_4 + 3/2\ O_2 \text{ -> } PbO + 2H_2O + 4C_2H_4 \tag{2.11}$$

$$PbO + TiO_2 \text{ -> } PbTiO_3 \tag{2.12}$$

These researchers later concluded that the growth of $PbTiO_3$ cannot be described by a combination of independent diffusion limited growth of PbO and TiO_2, but that it is controlled by a competitive process of Pb- and Ti-containing species on the surface [Dormans et al. 1992b].

No reports of $PbTiO_3$ films formed by LPCVD conditions (see definition in §2.4) have been made. Some researchers have used photo-induced processes [Shimizu et al. 1991, Katayama et al. 1992] and have achieved highly oriented films at lower temperature (600°C). Other researchers used additional oxygen (wet or dry)

Table III: Precursors used in the MOCVD of $PbTiO_3$

Source		Reference
Lead	Titanium	
$PbCl_2$	$TiCl_4$	Nakagawa et al. 1982, Okuyama & Hamakawa 1985, Kavanaugh & Williams 1989
PbO	$Ti(OC_4H_9)_4$	Okuyama & Hamakawa 1985, 1991
$^1Pb(OC_4H_9)_n$	$^2Ti(OC_3H_7)_4$	Brierley et al. 1987,1989
Pb	$^3Ti(OC_2H_5)_4$	Yoon & Kim 1988, 1990; Yoon et al. 1989, 1991; Kim & Yoon 1992
$Pb(C_2H_5)_4$	$Ti(OC_3H_7)_4$	Okada et al. 1988, 1989, 1990; Kwak et al. 1988; Swartz et al. 1989; Sakashita et al. 1991; Shimizu et al. 1991; Dormans et al. 1991, 1992; de Keijser et al. 1991, 1993; Greenwald et al. 1992, Okada & Tominaga 1992; Erbil et al. 1992, Chen et al. 1992, Katayama et al. 1992
$Pb(C_2H_5)_4$	$^4Ti(n\text{-}OC_3H_7)_4$	Erbil et al. 1992
$^5Pb(FOD)_3$	$Ti(Acac(MeO))_2(OPr^i)_2$	Brierley et al. 1989, Ainger et al. 1990
$^6Pb(acac)_2$	$Ti(OC_3H_7)_4$	Kingon et al. 1990
$Pb(OBu^t)_2$	$Ti(OPi)_4$	Brierley et al. 1989
$^7Pb(DPM)_2$	$Ti(OC_3H_7)_4$	Itoh et al. 1991, Funakubo et al. 1991
$Pb(C_2H_5)_4$	$^8Ti(OC_4H_9)_4$	Petuskey et al. 1991
$^9Pb(thd)_2$	$Ti(OC_2H_5)_4$	Peng & Desu 1992
$Pb(thd)_2$	$Ti(OC_3H_7)_4$	Gao et al. 1993

1. lead tertiary butoxide
2. titanium isopropoxide (TIP)
3. titanium ethoxide or $Ti(EtO)_4$
4. titanium n-propoxide
5. lead dimethylheptafluoroacetylacetonatate
6. lead acetylacetonate
7. bis(dipivaloylmethanato) lead
8. Titanium tert-butoxide
9. lead β-diketonate or tetramethylheptadione

during deposition [Okada et al., Swartz et al. 1989]. Annealing at higher temperatures might be connected to increased preferred orientation (see §2.6) of the films [Swartz et al. 1989], while other studies found annealing was necessary to improve film properties for the best electrical results [Dormans et al. 1991]. Work on $PbTiO_3$ showed the crystalline phase formed tends to be perovskite only in the range of 520-640°C, while pyrochlore [Martin 1965] or $PbTi_3O_7$ [Aykan 1968] phases form outside this range [Katayama et al. 1991, Okada et al. 1989]. It is desirable to have some excess Pb (in the form of lead oxide) because this ensures that a lead deficient state which promotes the formation of a pyrochlore compound does not prevail. Pb loss occurs upon annealing, so the need for excess Pb is increased for films which are to undergo further heat treatment(s) [Baba-Kishi et al. 1990].

2.5 Structural Characterization

For optimization of films for memory applications, investigation of their physical and electrical properties is essential. To begin with, the ferroelectricity of the material, in particular, whether a pure perovskite-type structure and ferroelectric film have been obtained, and whether the material will behave in a ferroelectric manner, as determined by electrical testing, needs to be assessed. This latter item will be addressed in §2.7.

Attempts to produce a $PbTiO_3$ film can result in TiO_2 or PbO_x-rich $PbTiO_3$ [Dormans et al. 1991, Katayama et al. 1992], impure $PbTiO_3$ contaminated by elements from the precursor materials (with Cl or C for example) [Yoon et al. 1991, Greenwald et al. 1992] or from system problems [Greenwald et al. 1992], or a new compound formed by reaction with the substrate [Madsen and Weaver 1992, Dormans et al. 1991]. An inhomogeneous film with two or more regions varying in composition or phase could also be formed. Investigation of the chemical composition at reasonably high spatial resolution can be done with energy dispersive x-ray spectroscopy (EDS), electron microprobe (EMPA), or AES. EDS is a widely available technique and although less quantitative than other methods, it can give semi-quantitative data by using standards.

Table IV: Deposition parameters for $PbTiO_3$ with TIP and PbEt as the Ti and Pb precursors[a] respectively.

Parameters	PbEt	TIP
Temperature (°C)	-10 to 25	15 to 106
Partial Pressure (Torr)	0.008- 3.75	0.008- 3.75
Flow Rate (sccm)	40.5 to 700	12.5 to 2000
Carrier Gas	Ar or N_2	Ar or N_2
Substrate Temperature (°C)	350 to 800	
Deposition Time (hrs.)	0.5 to 6	
Deposition Rate (μm/hr)	0.08 to 600	
Oxygen Source Gas	O_2, N_2O/NH_3, NO_2/Ar	
Total Flow (sccm)	260 to 5000	
System Pressure (Torr)	3.75 to 760	
Metallization or Oxide base	MgO(100), sapphire(0001), $SrTiO_3$(001), Pt, Pd, SiO_2, fused quartz, Si(100)	
Anneal	none, 600°C/60 min/O_2, 700°C/30 min/air	

[a] For other precursors, see Table III.

Although, it is desirable to obtain the tetragonal ferroelectric, perovskite $PbTiO_3$ compound, at least five other ternary phases or compounds are known to exist in the Pb-Ti-O system (Table V). Commonly a pyrochlore phase is observed with $PbTiO_3$ or PZT-type compounds [Wong-Ng et al. 1992]. The particular compounds which form are typically determined by temperature and pressure conditions during deposition [Chen et al. 1992] and their formation may be affected by heating or cooling rates, or impurities in the films.

Table V: Types of lead titanate compounds in the JCPDS database [1992].

Compound	Crystal System	JCPDS reference number	Structure Type/ Common Name
$PbTiO_3$	cubic	40-99	perovskite
$PbTiO_3$	tetragonal	6-452	perovskite/ macedonite
$PbTiO_3$	tetragonal	42-4	
$Pb_2Ti_2O_6$	cubic	26-142	pyrochlore
$PbTi_2O_7$	cubic	20-601	
$PbTi_3O_7$	monoclinic	21-949	

Phase identification may be obtained using x-ray diffraction (XRD), Raman spectroscopy or electron diffraction. These techniques allow the crystallography of the material to be determined by matching to standards in a database using a knowledge of the probable elements in the film, or when insufficient information in the database exists, through simulation of spectra or patterns of the relevant compounds.

XRD is an analysis tool which yields crystallographic information from

studying the interaction of monochromatic x-rays with a periodic crystal lattice. This interaction gives rise to diffracted beams of x-rays which can be used to identify the crystal. A typical sampling volume with this technique is of the order of 1 cm^3. When thin films are being examined, it is often desirable to reduce the substrate contribution to the x-ray spectra by altering the system geometry to a glancing-angle (GA) mode. Without this adjustment, reflections from the thin film can be obscured by those from the substrate or other underlying layers. The penetration depth of the x-ray beam into the material varies according to whether evanescent or normal absorption occurs [Toney et al. 1988]. The x-ray beam is described as evanescent within the film below a critical angle, α_c defined as:

$$\alpha_c \text{ (radians)} = 2.32 \times 10^5 \text{ (cm/mol)}^{1/2} \lambda (\rho\, \Sigma Z_j / \Sigma A_j)^{1/2} \qquad (2.13)$$

where λ is the x-ray wavelength in cm (1.54×10^{-8}cm for Cu K_α radiation), ρ is the density in g-cm^{-3}, Z_j is the atomic number, and A_j is the atomic mass in g-mol^{-1}.

In the evanescent region, the penetration depth (m) is given by:

$$D(\alpha) = \lambda/(\pi\sqrt{8})\,[(\Delta^2 + (\lambda\mu/2\pi)^2)^{1/2} - \Delta]^{-1/2} \qquad (2.14)$$

where μ is x-ray linear absorption coefficient in cm^{-1} and $\Delta = \alpha^2 - \alpha_c^2$ where α is the grazing incidence angle in radians.

Well above the angle α_c, normal absorption occurs according to the following expression:

$$I_x = I_o e^{-\mu x}$$

where I_x is the intensity of the transmitted beam after passing through a

thickness x and I_o is the intensity of the incident beam [Cullity 1978]. For a grazing incidence beam, the penetration depth (normal to the surface) may be calculated from:

$$D(\alpha) = \sin\alpha / \mu \qquad (2.15).$$

As the density of thin films or powder samples [Cullity 1978] can be lower than the values for bulk samples, figure 12 shows the penetration depths of Cu K_α radiation for $PbTiO_3$ for $\rho = 7.97$ g-cm^{-3} and for 60 percent of the bulk density ($\rho = 4.78$ g-cm^{-3}).

As with many thin films, a preferred orientation(s) or non-random texture can form in $PbTiO_3$. For example preferred orientation can develop due to film alignment with the substrate [Chen et al. 1992, Dormans et al. 1991] or growth conditions. To investigate the preferred orientation of a deposited layer, the texture coefficient TC(hkl) can be obtained using the Harris method [Barrett and Massalski 1980]:

$$TC(hkl) = \frac{I(hkl)}{I_o(hkl)}\left[\frac{1}{n}\sum\left(\frac{I(hkl)}{I_o(hkl)}\right)\right]^{-1} \qquad (2.16)$$

where I_o(hkl) is the intensity of a standard for a given plane, I(hkl) is the measured intensity for a given plane, and the summations are for all planes observed for the deposited film.

XRD also can provide precise information on the lattice parameters of the material. For bulk $PbTiO_3$, the values of the tetragonal crystal formed were measured as a=3.904 Å and c=4.150 Å (c/a=1.063) [Megaw 1946] and a=3.894 and

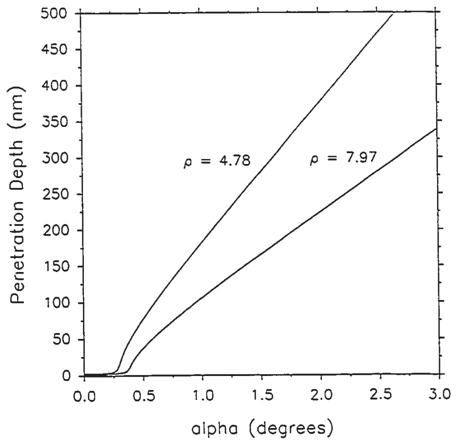

Figure 12: Penetration Depth of Cu Kα x-rays into $PbTiO_3$ at two densities, 7.97 g-cm^{-3} for single crystal material, and at 60% of this value (4.78 g-cm^{-3}) for powders or porous thin films.

c=4.140 Å (c/a=1.063) [Shirane et al. 1950] by x-ray diffraction. Later the values of a=3.90 Å and c=4.15 Å were determined by neutron diffraction [Shirane et al. 1956]. Table VI summarizes the XRD findings on $PbTiO_3$ thin films deposited with TIP and PbEt precursors onto Pt-coated substrates.

Table VI: Summary of XRD investigations

Substrate	Texture of $PbTiO_3$	Lattice Parameters (Å)	Reference
(100) Pt on (100) MgO	c-axis oriented	a=4.15, c=3.90	Chen et al. 1992
Pt on Ti/SiO_2/Si	N.A.	-	Greenwald et al. 1991
Pt on (0001) sapphire or (100) MgO	N.A.	-	Katayama et al. 1992
Pt on alumina	100 & 200 preferred orientation	a=4.09, c=3.91	Swartz et al. 1989
Pt on SiO_2/Si	randomly oriented	-	Dormans et al. 1991

N.A.: not available

Lattice parameters can vary with chemical composition, and strains or stresses in the film. The latter are almost always present in thin films deposited on substrates [Segmüller and Murakami 1988]. They are introduced into the film during the film deposition and/or during an additional thermal or chemical treatment. If the stress field is uniform in the volume being analyzed, there will be a systematic shift in the angular position of the diffraction peaks, which can be used to measure the stress

[Prevey 1986]. On the other hand, stresses varying from point to point within the volume being analyzed cause broadening of the diffraction peaks. The stresses and strains in thin films can be measured in two ways: (i) by measuring the lattice spacings of the film in one or more directions using an x-ray diffractometer and comparing these results to an unstressed strain-free film, or (ii) by measuring the elastic deformation imposed on the substrate [Segmüller and Murakami 1988].

Raman spectroscopy has been used for material and phase identification, and structure and phase transition temperature determination of bulk ceramics [Burns and Scott 1970, Burlakov and Yakheev 1989]. Usually a Raman microscope uses a highly monochromatic, coherent, narrow beam with high intensity as a light source, namely a continuous wave laser [Gardiner and Graves 1989]. It is coupled to a spectrometer so that light transmitted, reflected or scattered by the sample can be imaged and analyzed spectroscopically. When a photon of light, too low in energy to excite an electronic transition, interacts with a molecule it can be scattered elastically (retaining its incident energy) or inelastically (by giving energy to or taking energy from a molecule). Energy gained by a molecule (by a process called Stokes scattering) appears as "vibrational energy". Usually the intensity of the scattered beam is displayed as a function of frequency relative to the excitation wavelength (in the units of r-cm^{-1}). The individual features of a Raman spectrum are characteristic of certain lattice phonons and/or chemical bonds. The strength of Raman spectroscopy lies in this ability to provide information on the chemical and physical structure of materials, including molecular bonding whereas other techniques often supply only elemental

composition [de Wilton 1988]. The identity (including the composition and phase) and quality of a material may be assessed from the spectrum, by comparison to reference spectra. Any individual features or regions of the films can also be easily examined. Raman spectroscopy is capable of acquiring characterization data quickly and non-destructively. There are 2 major areas of interest in the Raman spectroscopy of ferroelectrics: crystallographic structure and phase changes as studied in the high frequency regime (100-1000 r-cm^{-1} shift from incoming laser frequency) and the heavily damped temperature dependent "soft" modes of oscillation characteristic of ferroelectrics and observed at shifts typically under 100 r-cm^{-1} [Oliver 1989]. Care must be taken with this technique since the observation of peak shifts or the occurrence of new peaks can also be indicative of changes in stoichiometry or contamination.

Electron diffraction studies consist of analyzing patterns formed in the back focal plane of the objective lens of a transmission electron microscope [Goodhew and Humphries 1988]. If the specimen is amorphous, that is the constituent atoms or molecules are arranged entirely randomly and without any repeating structure, the diffraction pattern will contain no distinct maxima and will consist only of 2-3 diffuse rings around the bright central spot. As the arrangement of atoms or molecules in a material become more ordered, the diffraction pattern will be composed of spotty rings, and then with more ordering, spots will be observed. For example, single crystals give a diffraction pattern which is a simple array of bright spots arranged in a symmetrical pattern about the incident beam. If the area of the sample being analyzed incorporates several grains, then its diffraction pattern will consist of a number of spotty rings. If the specimen consists of two crystals, as in the case of twins (when one crystal is the mirror image of the other), the diffraction pattern contains two superimposed patterns rotated with respect to each other. Orientation relationships between grains, or between precipitates, inclusions or twins and the surrounding matrix can be determined. Preferred orientation can be detected in diffraction patterns of polycrystalline samples as regions of higher contrast form within the rings. As in XRD, d-spacings can be calculated from the distances between spots or the diameters of the rings and the lattice parameters of the material can be determined. For d-spacings calculations, the following equation is used [Hirsch, Howie et al. 1965]:

$$D = 2\lambda L / d \tag{2.17}$$

where D is the measured ring diameter in cm, λ is the relativistic wavelength in Å, L is the camera constant in cm, and d is the d-spacing of the crystal planes in Å.

Stress and strain manifest themselves as distortion in diffraction patterns, such as "smearing" of spots. Electron diffraction necessarily involves the preparation of a thin transmission electron microscopy (TEM) sample, which may be useful for other purposes, but is nevertheless often tedious and requires the use of specialized equipment. Diffraction patterns from plan-view (transverse) samples of the top layer of thin film samples provide larger areas to work with because of the columnar nature of many films. However to look at the substrate and substrate-film interface, cross-

sectional samples are needed. Electron diffraction offers an advantage over XRD in terms of its specificity within the sample because of the much smaller beam size.

An understanding of how the processing parameters (film deposition, annealing, etc.) affect the material properties, such as morphology, structure, porosity, and interfacial characteristics, can be obtained with the aid of a variety of analytical techniques. Degradation (shorting of electrodes) observed during electrical testing has been attributed to diffusion along grain boundaries or high porosity of films. A knowledge of the surface morphology of films in terms of microcracks, porosity, and roughness obtained by scanning electron microscopy (SEM) have aided in the understanding of electrode contact quality.

As described in §2.1, the basic mechanism by which ferroelectricity takes place is through the formation and motion of domains. TEM imaging can reveal the microstructure of the material including the domain structure, interfacial characteristics, and growth pattern of the film (for example, whether it is epitaxial or columnar). Domains have been observed in three different forms in $PbTiO_3$ type films (figure 13).

A "herringbone" pattern has been observed in TEM images of bulk ceramics of the $PbTiO_3$ type. This pattern has also been observed in thin films with grain sizes ranging from 0.2-2 μm [Hseuh & McCartney 1990, Goral et al. 1990, Myers and Chapin 1990, Gao et al. 1993]. Experimentally the minimum grain size found for twinning in bulk La-modified $PbTiO_3$ ceramics was 0.3 μm [Demczyk et al. 1987]. The contrast observed in TEM images is due mostly to 90° (or 180°) domains (or twins). The domain widths observed range from 10-100 nm. As well, defects such as voids, regions of amorphous structure, or pyrochlore phases have been reported.

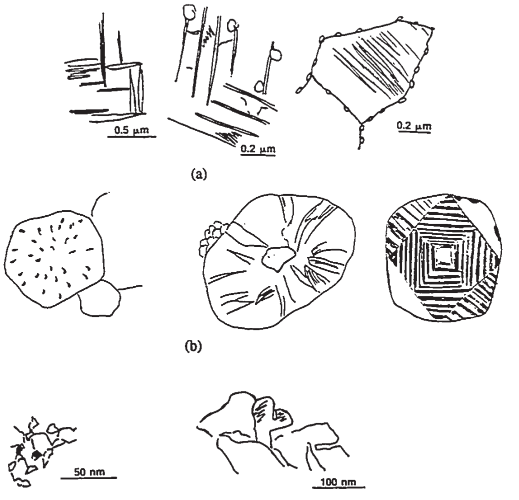

Figure 13: Schematic diagram indicating the three types of domain structures observed by TEM:
(a) traditional "herringbone" (*from left to right*)- (i) MOCVD $PbTiO_3$, grain size ~1 µm in diameter, domain width ~75 nm [Gao et al. 1993], (ii) sputtered PZT, grain size ~1 µm in diameter, domain width 10-100 nm [Goral et al. 1990], and (iii) sol-gel PZT, grain size 0.8-2 µm in diameter, domain width 25-100 nm [Myers and Chapin 1990];
(b) rosettes (*from left to right*)- (i) sol-gel PZT, grain (rosette) 1-4 µm in diameter [Hseuh and McCartney 1990], (ii) sol-gel PZT, rosettes of 2-5 µm in diameter, width of arms of rosette 28-130 nm [Myers and Chapin 1990], (iii) sol-gel circular single crystal perovskite 0.96 µm in diameter, width of domains ~25 nm [Voigt et al. 1993],
(c) mono-domains (*from left to right*)-(i) chemical beam $PbTiO_3$, grain size 10-50 nm in diameter [Kingon et al. 1990], and (ii) sputter deposited PZT, grain size 2-5 nm in diameter [Weaver, Madsen and Griswold 1991].

Spherulite grains or rosettes 1-5 μm in diameter, have been found in sol-gel processed thin films [Myers and Chapin 1990, Hseuh & McCartney 1990] reflecting the nucleation and growth sequence prevalent in these films. Some rosettes were almost featureless apart from a radial pattern of porosity [Hseuh and McCartney 1990]. Others had a single grain in the centre acting as a nucleation site for lamellae (domains) which radiated outwards [Myers and Chapin 1990]. The single central grain contained a herringbone type structure. Each lamella in the radiating arms had a different orientation and a width of 28-130 nm. Voids and pyrochlore phases were observed at the grain boundaries [Myers and Chapin 1990].

Small individual grains can act as domains in thin films [Weaver, Madsen and Griswold 1991; Kingon et al. 1990] or bulk ceramics [Martirena and Burfoot 1974] and are termed mono-domains. In the thin films of these studies, sub-grains 2-50 nm in diameter were observed. Slight orientational changes were noted from grain-to-grain. Dislocations at low angle grain boundaries as well as some amorphous regions have been reported [Kingon et al. 1990]. Micro-cracking at grain boundaries was found despite processing below T_c [Kingon et al. 1990]. Processing below T_c dictates that the grains were formed in the tetragonal structure and would not undergo the significant volume change which occurs when the cubic to tetragonal transformation takes place. The marked micro-cracking in films processed above T_c was believed to be a form of stress relief since again for these fine-grained films there was an absence of stress relief by twinning which can occur in coarser grained material [Weaver, Madsen and Griswold 1991]. It is thought that a combination of the unusual clamping criteria for small grains (200 nm) and the presence of a morphotropic composition (near the tetragonal-rhombohedral boundary of PZT) hindered the formation of a simple domain structure [Reaney et al. 1994].

Domains in bulk ceramics with the traditional domain configuration (as depicted in figure 13a) either have a parallel twin structure or a wedge type structure (as observed by Hseuh and MeCartney 1990 for thin films). Periodic wedge domains are essentially twins with head-to-tail dipole coupling [Randall et al. 1985]. The bulk ceramic grains were normally quite large (>1 μm) but the width of the domains was 10-150 nm [Michel 1976, Randall et al. 1985, Lucuta 1989].

In summary, it would appear that domain formation varies with grain size in the same way for bulk ceramics and thin films of $PbTiO_3$ type compounds. Furthermore domains are roughly of the same size: 2-50 nm in diameter (for mono-domains); 28-130 nm wide in spherulite lamellae, and 10-150 nm wide twins in conventional large grains (>0.2 μm). These results suggest that the domain structure is directly related to the grain size; that is, if the grains are too small to twin then individual grains themselves act as domains [Martirena and Burfoot 1974]. The ferroelectric domain structure is related to the formation of twins which accommodate the stress in the material during the cubic to tetragonal transformation [Zheleva et al. 1993]. More success with electrical reliability has been obtained with spherulite sol-gel films than with films with the traditional herringbone structure [Myers 1993].

The reason for this behaviour was not known.

A categorization scheme for the observed TEM domain structures with an indication of the formation mechanisms and resulting size of the domains has not previously been presented. This method of analysis allows comparison between films with different structures and between bulk and thin film material.

Film thicknesses needed for interpretation of electrical data may be obtained from optical techniques (e.g. ellipsometry), physical methods (e.g. talystep), or by electron microscopy (scanning or transmission) using cross-sectional samples.

2.6 Electrodes

Several challenges are presented in integrating FE material into memory circuits including selection of a suitable bottom electrode/ barrier layer and top electrode, control of any possible contamination problems and development of an etch process for the FE material of interest. Some of these issues are discussed in further detail below.

For a capacitive structure (figure 14a), the "plates" must be made of a conductive material: metal, polycrystalline silicon, silicide, or a conductive oxide are candidate materials [McMillan 1989]. Various layers and electrodes have been discussed in the literature (Table IV); the most widely used combinations involve Pt. One of the primary reasons for using Pt may simply be that it does not oxidize readily. In general, the formation of interfacial layers and substrate-layer interactions during the growth are important for film thicknesses in the sub-micrometer range as they tend to dominate the response of the material [Roy et al. 1990b]. In one study, sputtered films of PZT on Pt showed a greater tendency for electrical shorting and rougher microstructure when deposited on unheated substrates which suggested metal diffusion into the films may be dependent on the microstructure prior to the diffusion step [Roy et al. 1990b]. Additionally, it has been proposed that changes in the dielectric constant measured for lead titanate type films before and after annealing indicate that layers having a low dielectric constant form at the interface or grain boundaries during film growth [Roy et al. 1990]. When TiN_x was used as a barrier layer and bottom electrode for a 450 °C ion-beam sputtered PZT film, Rutherford backscattering (RBS) and AES analyses revealed an insulating barrier had formed at the electrode-FE interface [Ameen et al. 1990]. Further RBS studies indicated that after a 700 °C anneal, Pb had diffused from the PZT layer into the underlying TiN layer [Parikh et al. 1990]. At this annealing temperature, ZrN_x, TiO_x and ZrO_x were also inadequate as barrier layers [Parikh et al. 1990]. A study of TiN at NTEL found it to be unsuitable as an interlayer between the sputtered PZT thin films and Si substrates for the conditions investigated [Madsen and Weaver 1991], primarily because of its oxidation at the high deposition temperature used. Although other researchers have experienced difficulties with TiN [Parikh et al. 1990], it should not be dismissed as a feasible layer since adhesion was better than with several other materials studied. It has also been suggested that some interdiffusion occurs with titanium silicide, Pt on SiO_2 and platinum silicide at deposition substrate temperatures of 450 to 550 °C and for higher anneal cycles [Ameen et al. 1990]. When SiO_2 on Si was used as a substrate, shorting and lower dielectric constants were observed [Roy et al. 1990] due to cracking of the film [Emesh 1993].

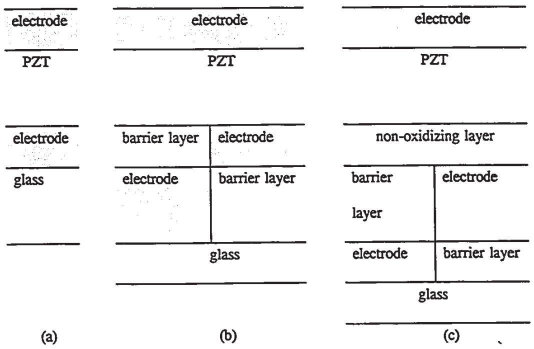

Figure 14: Possible arrangements for Capacitor Structure

Top electrode materials which have been used are Al, Pt, and Au (Table IV). The choice of material and deposition method can have significant effects on the electrical characteristics with ageing [Burfoot and Taylor 1979]. The usual manifestation of ageing is a gradual decrease in the amount of polarization switched per reversal. Pt top contacts established switching symmetry and eliminated the high loss of polarization observed with Au electrodes. A minimum top electrode thickness of 3000 Å was necessary to survive losses caused by diffusion into the FE [Sharma et

Table VII: Layers used as substrates, barriers and contacts with FE material.

Bottom Layers	References[a]
Si<100>	Boyer et al., Ramkumar et al., Peterson et al.
Pt on Si, on SiO_2/Si, on an unspecified barrier layer on SiO_2, on Ti/Si<100>, on MgO<100>, or on CaF_2	Ameen et al., Kwok et al., Ramkumar et al., Chiang et al., Hsueh and McCartney, Goral et al., Roy et al., Tuttle et al., Sudhama et al., Boyer et al., Naik et al., Goral et al., Matsubara et al., Saenger et al., Etzold et al.
Pt	Chiang et al.
Platinum silicide	Ameen et al.
TiO_x/SiO_2/Si	Parikh et al.
TiN_x/SiO_2/Si	Parikh et al.
TiN/MgO	Ameen et al.
Titanium silicide	Ameen et al.
ZrN_x/SiO_2/Si	Parikh et al.
ZrO_x/SiO_2/Si	Parikh et al., Myers and Myers
Cr, CrO_x	Myers and Myers
Zr	Myers and Myers
Ni, NiO_x	Myers and Myers
SiO_2/GaAs	Swartz et al.
Si_3N_4/GaAs	Swartz et al.
ITO/glass	Johnson et al.
glass	Ramkumar et al.
fused silica	Peterson et al., Boyer et al.
GaAs<100>	Boyer et al., Payne et al.
sapphire	Ainger et al.
Top Electrode	**References[a]**
Al	Johnson et al., Ameen et al.
Pt	Etzold et al., Sudhama et al., Saenger et al.
Au	Johnson et al., Desu et al., Kwok et al.

[a] All from the Mater. Res. Soc. Symp. Proc. **200** [1990] or presented at the Spring meeting [1990].

al. 1973]. Other researchers have found Pt with additives are best [see Scott 1989] and electrodes deposited by sputtering have shown better results than those made by evaporation [Haertling 1989].

Detailed information on the layers (top or bottom) associated with PZT of electrical devices with good performance characteristics are usually not reported [Shepherd 1990, Kalkur et al. 1990, Bondurant 1990].

The range of metals and other materials to consider from the silicon semiconductor industry are listed in Table VIII [Madsen and Weaver 1991]. Candidates not included in the above discussion (Table IX) [Madsen and Weaver 1991] are more difficult to integrate due to their limited or non-existent use in the semiconductor industry. Because of Pb's high mobility, a barrier material is often required below the PZT layer in addition to the electrode itself (Figure 14b). The electrode does not need to be protected from the PZT, providing neither its conductive properties nor the PZT's dielectric characteristics are adversely affected. For example, a barrier material X interposed between layers A and B acts as a diffusion barrier if the mixing or interaction of materials A and B is limited. Material X should satisfy the following requirements: the transport rate of A and B across X should be low; X should be thermodynamically stable with respect to A and B; X should have additional properties including good adhesion to A and B, a high electrical and thermal conductivity, and uniform thickness and structure [Nicolet and Bartur 1981]. Some barrier layers may require a top layer to prevent oxidation during the PZT deposition process or for incompatibility with the PZT film,

Table VIII: Conductive materials used in the silicon semiconductor industry

Material	Anneal/Dep. Temperature (°C)	Resistivity ($\mu\Omega$-cm)	Thermal Coefficient of Expansion (10^{-6}/°C)	Reference
Si	450-800	770	3.0-3.5	ASM 1989, Madsen & Weaver 1990, Wolf & Tauber 1986
Al	450-500	2.7-3.2	23.5	ASM 1989, Wolf & Tauber 1986
W	350-850	5-530	4.4-4.5	ASM 1989, Wolf & Tauber 1986, Levy & Green 1987, Pauleau 1984
$TiSi_2$	300-900	13-123	10.5	ASM 1989, Wolf & Tauber 1986, Pauleau 1987, Nicolet 1978, Murarka 1980
$MoSi_2$	400-1000	22-100	8.2	ASM 1989, Wolf & Tauber 1986, Pauleau 1987, Murarka 1980
TiN	300-1100	35-130	—	Chen et al. 1987, Nicolet 1978
Pt	—	9.85	8.9	ASM 1989, American Institute of Physics Handbook 1972
Ta	—	13-16	6.5	Wolf & Tauber 1986
Cu	150-390	1.67	17	Kaloyeros & Fury 1993, ASM 1989
Mo	400	4.8-10	5.9	ASM 1989
Ti	—	43-68	8.5	Wolf & Tauber 1986, Nicolet 1978
Au	—	2.35	14	ASM 1989
PtSi	300-800	28-35	—	Prabhaker et al. 1983
$CoSi_2$	600-900	18-28	—	Pauleau 1987, Murarka 1980
WSi_2	230-1000	14-70	6.2	ASM 1989, Wolf & Tauber 1986, Pauleau 1987, Murarka 1980
$TaSi_2$	540-580	8-55	8.8	ASM 1989, Wolf & Tauber 1986
ITO	400-950	200-400	—	Weigtens 1990, Venkatesan

Table IX: Conductive materials rarely used in the silicon semiconductor industry

Material	Anneal/Dep. Temperature (°C)	Resistivity ($\mu\Omega$-cm)	Thermal Coefficient of Expansion (10^{-6}/°C)	Reference
Pd	—	10.8	11.6	ASM 1989, American Institute of Physics 1972
Pd_2Si	350-400	30-35	—	Pauleau 1987, Majni et al. 1985
NiSi	—	—	15	Nicolet 1978
$NiSi_2$	< 900	50-60	—	Martinez-Duart & Albella 1989
RuO_2[a]	20-200	35-1500	—	H. Kezuka et al. 1993
TaN	—	135-1650	3.6	ASM 1989, Nicolet 1978
$TiAl_3$	—	—	—	Nicolet 1981
$TaAl_3$	400-500	—	—	Nicolet 1981
Ag	450	1.59	19	ASM 1989
TiW	700-900	50-95	—	Norström et al. 1990, Pramanik & Jain 1991
Cr	—	12.9-18.9	5.0	ASM 1989, American Inst. of Phys. Handbook 1972, Nicolet 1978
Ni	—	6.84	12.8	ASM 1989, American Inst. of Phys. Handbook 1972
also: GaAs, PtAl, $ZrBr_2$, TiB_2				

[a] This material has been added because it has become one of the leading candidates for electrodes.

producing a more complex structure (figure 14c).

2.7 Electrical Parameters

Two important parameters which should be measured are the hysteresis (the non-linear irreversible response due of the application of a large electrical field) and the small signal dielectric behaviour (the linear reversible response from the application of a small electric field). Device reliability in terms of signal retention and reversibility also need to be assessed. All methods for testing the electrical properties of ferroelectric devices involve switching the sample from one state to another while periodically measuring its properties. The applied voltage can be a series of electrical pulses or a continuous wave. The former more closely simulates the conditions a real memory device would undergo. However, due to the nature of the response signal, it is more difficult to obtain the polarization parameters [Burfoot and Taylor 1979] and the coercive force value becomes meaningless due to the lack of a reference point [Abt 1990]. Its usefulness is in terms of determining switching times by observation of the signal decay in the sample. Use of continuous wave switching with either a sinusoidal or triangular wave is a convenient technique for probing the intrinsic properties of ferroelectrics and extracting the pertinent hysteresis parameters. The two approaches may be used together; for example, the sample may be degraded with pulses and then examined with a continuous wave.

2.7.1 Large Signal Electrical Properties

The hysteresis associated with a ferroelectric material can be measured by applying a large oscillating electrical field using a Sawyer-Tower configuration (figure 15) [Johnson 1990]. For a 0.2μm thick film of PZT for example, the applied voltage peak-to-peak (V_{pp}) required is 1 V to observe apparent domain switching, 1 to 2 V for

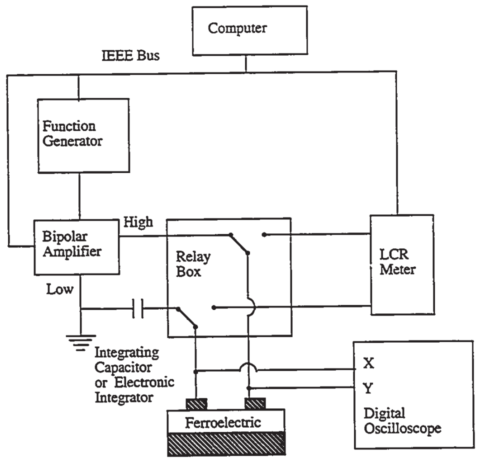

Figure 15: Sawyer-Tower Electrical Test Circuit

a marked increase in polarization response and greater than 5 V for saturation [Johnson 1990]. Parameters measured from the hysteresis loop (figure 2) are P_r, E_c, P_{sp} defined by the intercept of the extrapolation of the linear extreme of the loop, and P_s the maximum polarization observed. Where incomplete saturation or dielectric breakdown occurs, the saturation polarization can be defined as the value of polarization at three times E_c [Burfoot and Taylor 1979].

2.7.2 Small Signal Electrical Properties

The permittivity, ϵ, depends on the voltage and frequency of the applied signal, stress, temperature and other parameters [Burfoot and Taylor 1979]. By definition,

$$\epsilon = \epsilon_0 + \eta \qquad (2.18)$$

where ϵ_o = permittivity of free space

= 8.85×10^{-12} C-V^{-1}m^{-1},

and η = susceptibility

= P / E.

Here the polarization P is calculated from

$$P = q / A \qquad (2.19)$$

where q is the charge produced at the electrodes and A is the electrode area, and

$$E = V / d \qquad (2.20)$$

where V is the applied voltage and d is the dielectric thickness. Measurements using an A.C. bridge circuit necessarily involve the use of low E values (< 1 kV-m^{-1}) to

avoid irreversible switching effects.

In the paraelectric (cubic) phase ϵ obeys the expression given in eqn. 2.1. The Curie-Weiss constant is 110,000°C for $PbTiO_3$ (compared to 170,000°C for $BaTiO_3$) [Burfoot and Taylor 1979]. The T_c for $PbTiO_3$ is 490°C and decreases almost linearly with Zr content to ~250°C for $PbZrO_3$ [Jaffe et al. 1971]. These values of ϵ, C, T_o and T_c can be very sensitive to dopants and dislocations in single crystal material and can be greatly affected by the applied electric field [Burfoot and Taylor 1979].

Often the value given in the literature for a material is its dielectric constant ϵ' which ranges from 100-200 for thin films of $PbTiO_3$ [Swartz 1990, Sayer et al. 1992]. The susceptibility is related to the dielectric constant by

$$\epsilon' = \eta / \epsilon_o \qquad (2.21)$$

and by using the definition of capacitance, C = q / V, then

$$\epsilon' = (d\ C) / (\epsilon_o\ A) \qquad (2.22).$$

The resistivity ρ of the material can also be assessed through the measurement of parallel resistance, R_p:

$$\rho = R_p\ A / d \qquad (2.23).$$

This value is ~10^8 Ω-cm for $PbTiO_3$ ceramics and thin films values range from 10^8 [Greenwald et al. 1992] to 10^{13} Ω-cm [Katayama et al. 1991]. The dissipation factor is a measure of the electrical losses and is usually evaluated in terms of tan δ. Tan δ (a dimensionless quantity) is the ratio of the imaginary to real part of ϵ and correspondingly shows an anomalous increase at T_o. It is related to C and R by the following expression:

$$\tan \delta = 1 / (2\pi f C R_p) \qquad (2.24)$$

where f is the frequency in Hz.

For good insulators, this value is typically 0.01 to 0.3 [Burfoot and Taylor 1979].

2.7.3 Reliability

Three degradation effects have been identified in lead titanate type compounds: ageing- the loss of switchable polarization with time; fatigue- the loss of switchable polarization as a result of repeated polarization reversals [Shepherd 1990] and imprinting- the inability to switch states with time and/or reversals of polarization.

Ageing causes an exponential-type decrease in ϵ and tan δ. It is thought that ageing is due to relief of internal stress, locking of domains by a mobile space charge, and/or electrolytic migration of oxygen vacancies in the material under the influence of a D.C. field [Burfoot and Taylor 1979]. Material may be restored or "de-aged" to its original state by heating above T_c depending on the cause of the degradation [Stewart and Costentino 1970].

Although the root causes of fatigue in ferroelectric material are not well understood, strain relief and structural defects are believed to play a role [Johnson 1990]. Testing of sample degradation of good material can take from 17 min to greater than 3 years depending on the test frequency (Table X).

Table X: Fatigue testing times

Number of Cycles	Frequency		
	10 kHz	100 kHz	1 MHz
10^9	28 hrs.	2.8 hrs.	17 min.
10^{10}	11.6 days	28 hrs.	2.8 hrs.
10^{11}	116 days	11.6 days	28 hrs.
10^{12}	3.17 years	116 days	11.6 days

One of the more interesting aspects of these phenomena is how strain relief occurs and how structural defects play a role in the material and hence device degradation. Indications from recent talks presented at major ferroelectric conferences are that over fifty percent of the effort in ferroelectric memory applications is currently aimed at understanding and eliminating these effects, particulary for PZT material.

3.0 EXPERIMENTAL EQUIPMENT AND PROCEDURES

3.1 Chemical Vapour Deposition

3.1.1 System

A conventional horizontal hot-wall reactor CVD system was used for this work (figure 16). In its "traditional" configuration, this reactor had the capacity to hold 125 wafers, each 100 mm in diameter. Depending on the wafer spacing 14-25 wafers could be held vertically in each quartz boat fitted with a solid quartz lid. For research purposes, three to five test positions distributed over the length of each boat were normally used. The remaining positions would be filled with "dummy" wafers. Gases were delivered to the wafers via manifolds running the length of the furnace from the door towards the exhaust. In this configuration, the reactant gases were fed into one manifold, while the inert and oxidizing gases were fed into the other.

To enhance the deposition process, three major modifications were made to the hardware arrangement described above. The first change involved modifying the Ti source distribution system by having the liquid-source vapour (and its N_2 carrier) travel through a 6 mm stainless steel line to a 250 mm long quartz cylindrical tube, 100 mm in diameter. The end of this distribution tube was also made of quartz and was perforated with 49 holes. 1.5 mm in diameter (similar to a showerhead) to allow the gases to flow directly towards the wafer (figure 17a).

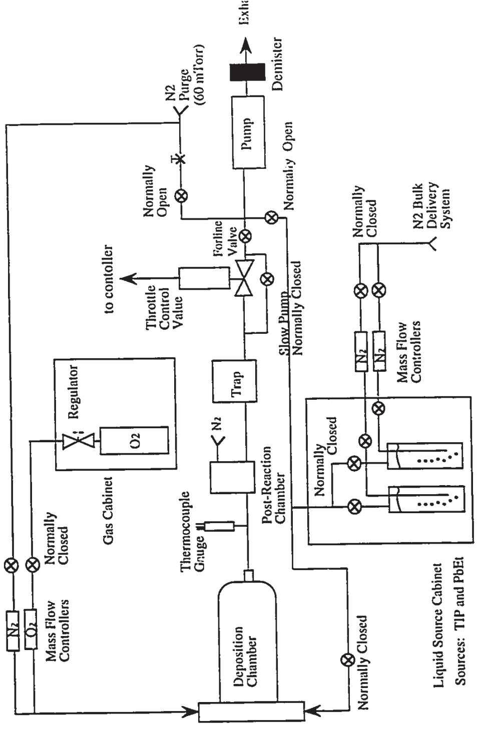

Figure 16: Schematic Diagram of the CVD system.

The second modification involved changing the heating arrangement such that only a single wafer was heated to the deposition temperature. Background heating was maintained at 100-200°C in the deposition chamber to prevent condensation of the gases. The substrate was mounted on a new stainless steel holder recessed 450 mm from the door of the furnace. A (miniature diffusion-pump) heater, either 75 or 80 mm in diameter, was positioned externally from the deposition chamber on the reverse side of the substrate holder. The modified Ti distribution system was again used with this configuration although the direction of the tube had to be reversed to accommodate the new arrangement.

The third modification involved the replacement of the quartz showerhead with a stainless steel diffuser plate with a larger number of small holes (~200) each 0.2 mm in diameter. This metal plate was then recessed from the end of the distribution tube (figures 17b and 18) and the remaining gases were also fed into the distribution tube.

The wafer chuck temperature was controlled with a thermocouple embedded into a 5 mm thick steel plate which held the wafer in position during deposition. The thermocouple was positioned off centre (by ~23 mm) and was directed outwards through the front side of the plate to make contact with the wafer. Calibration of the wafer temperature for both the 75 and 80 mm heaters was performed using k-type thermocouples attached at two locations on a Si wafer. These measurements were made at atmospheric conditions, not at the reduced pressures used for the deposition. The measurement thermocouples on the Si wafer were placed at the centre and 23 mm

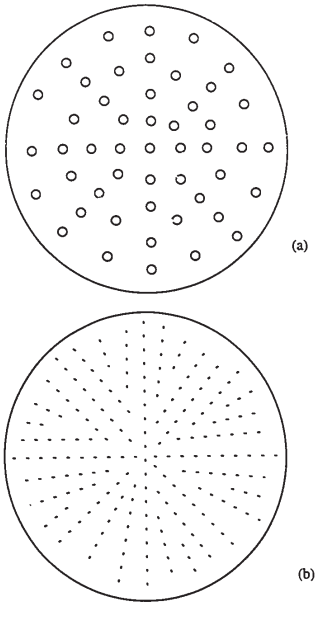

Figure 17: (a) Quartz showerhead with ~49 holes and (b) metal diffuser plate with ~200 holes.

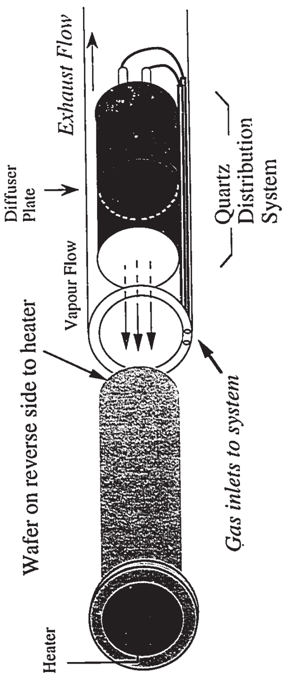

Figure 18: Configuration of heater, substrate, and gas distribution system in CVD set-up.

from the centre such that alignment with the control thermocouple could be made. The temperature dropped radially outwards from the centre (figure 19); for a target temperature of 400°C for the large heater, the temperature at the centre position was estimated to be 390°C. Furthermore for the same heater, it was estimated that the chuck was up to 80°C hotter than the wafer. As a result, the actual wafer temperature likely differed from the control thermocouple reading over the central 30 mm diameter region of interest in this study by ~10-80°C. Settings to a maximum of 515°C for the substrate temperature could be maintained with the 80 mm heater.

Pressure in the deposition chamber was monitored using a baratron gauge and was throttle-valve controlled to values ranging from 0.6 to 3 Torr in accordance with the selected deposition parameters. Two liquid sources, one for each of the major constituents Ti and Pb, along with gaseous O_2 and a carrier gas of N_2 to serve as a balance and purge gas, were connected to the system. Semiconductor grade TIP and PbEt were supplied by Morton International (Danvers, MA USA) and packaged in 250 or 450 cc stainless steel bubblers. The temperature of the compounds was controlled using Neslab temperature baths filled with a 50-50 ethylene glycol-water mixture for the Ti and Pb sources. To ensure the complete breakdown of compounds before they entered the exhaust system, a post reaction chamber (PRC) (Process Technology Limited, Oromocto, N.B.) was fitted to the system. The sequence of steps involved in the deposition process: the introduction of the gases, safety tests and purge cycles are outlined in Appendix A for the final hardware configuration.

Post-growth annealing was performed in a rapid thermal annealer (A.G.

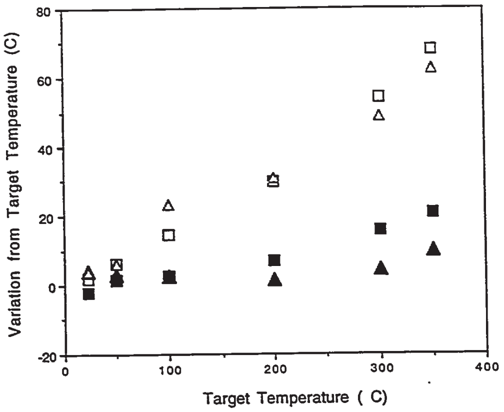

Figure 19: Variation of the measurement thermocouples from the control thermocouple for the 80 mm (▲,△) and 75 mm (■,□) heaters. Values reflect the average of two or more readings after the high and low measurements were discarded. Solid symbols (▲,■) show data from the centre thermocouple and open symbols (△,□) show data for the off-centre thermocouple.

Associates, model 410) for 40 s in air or pure O_2 atmosphere at atmospheric pressure. Calibration of the temperature controlling thermocouple in the RTA was done by attaching a meter to a thermocouple mounted on a full wafer (Appendix B).

3.1.2 Safety Considerations

For general safety, the laboratory was equipped with two exits, an eyewash, shower and fire extinguisher. Additionally, there were two emergency power shut-offs for the CVD system, one situated near the front panel of the furnace and another by the emergency exit door. Diagrams showing evacuation routes, location of safety shut-off values, the furnace configuration and gas line distribution were posted. Labelling of gas lines and sources were completed. Over-temperature alarms were fitted to each liquid source temperature bath. There was a telephone in the laboratory to contact the emergency response team, or alternately, if evacuation was necessary, an emergency red-coloured direct line telephone in the corridor outside. Safety inspections were carried out on a monthly basis and any problems were corrected as soon as possible. Before the start of each deposition cycle, the system was checked for vacuum leaks. Over-pressure sensors and automatic aborts of the deposition cycle were in place. System pump and post reaction chamber maintenance were carried out by qualified personnel wearing self-contained breathing apparatus. The gas and liquid supply cabinets, along with the furnace itself, were exhausted directly out of the building. As much of the work took place in isolation, the main door to the laboratory and the wall along the corridor had viewing windows.

Due to the increased danger of working with lead, all individuals spending more than one hour per month in the laboratory were monitored for Pb in their body by means of urine and blood analyses. Particulate control in the laboratory was maintained through the use of a contained processing area, negative laboratory pressure, and high efficiency vacuuming. Temperature was restricted to below 300°C for the CVD chamber at atmospheric pressure. Air monitoring, protective clothing and respirators were used. To guarantee conformance to liquid emission standards, the effluent from the tube washer was monitored regularly for Pb content.

Quartzware cleaning was done with an undiluted 5:3:3 nitric:acetic:hydrofluoric acid mixture. These chemicals required strict handling procedures; (refer to the applicable material safety data sheets). Also, the acid mixture was extremely slippery and care had to be taken to avoid splashing during the cleaning process. Sometimes the quartzware was replaced rather than cleaned as this approach was less dangerous and often more cost effective.

3.1.3 Titanium Oxide

100 mm substrates of Si <100> with or without a 100 nm SiO_2 layer were used. One substrate with additional layers, described as BNR Pt in §3.4 was also used.

Initially, the conventional CVD configuration described in §3.1.1 was used. The initial parameters were partially determined using information from published papers [Okada 1988-90, Kwak 1988, Swartz 1989], with some adjustments to suit a

large CVD furnace. Without a rudimentary knowledge and understanding of the deposition mechanisms, the range of the experimental variables to be tested might be so large that the optimum region for the process might be missed. To screen the area of interest, an experimental design of a fractional factorial type (with a centre point) was used [Box et al. 1978]. Parameters were selected for the deposition of TiO_2 using experimental designs for each matrix (Table XI). In the first matrix, the substrate temperature was varied from 300°C, a minimum temperature for many CVD processes, to a maximum of 600°C. Since in industrial practice the ferroelectric layers would be deposited after the regular device structures, it is desirable to minimize the thermal budget to reduce diffusion and prevent deterioration of the underlying layers. A realistic pressure range for this system was 0.2 to 5 Torr. The Ti source temperature was varied from 25°C (just above its melting point) to 45°C (or in terms of pressure from 133-629 mTorr). The raw experimental variables have been used rather than the adjusted data such as partial pressure. Conversions to other values are made at the appropriate points. The total flow of gases used was 400 to 1000 sccm; this range was related to the pressure values selected for the system. The Ti carrier flow was varied between 160 and 400 sccm such that the oxygen to Ti carrier flow rate could be varied from 0.5 to 1.5 (Table XII). In all experiments the balance gas used was N_2. The deposition time was fixed at 40 min.

As the CVD system was modified, new screening experiments were necessary. The information gained from the previous experiments along with the new constraints or options due to the hardware changes affected the ranges chosen in the subsequent matrices. Details of the precise experimental run conditions are given in Appendix C.

Table XI: Starting parameters for TiO_2 deposition

Parameters	Matrix One (conventional configuration)	Matrix Two (modified distribution system for Ti)	Matrix Three (heated substrate)
substrate temperature (°C)	300-600	300-400	300-400
system pressure (Torr)	0.5-1.5	0.5-3.0	0.6-2.0
total flow of gases (sccm)	400-1000	640-1200	500 (fixed)
Ti source temperature (°C)	25-45	35-45	35-45
Ti carrier flow (sccm)	160-400	160-300	300 (fixed)
oxygen to Ti carrier flow ratio	0.5-1.5	0.5-3.0	0 - 2/3
deposition duration (hr)	0.67	4.0	0.5-4.0

Table XII: Relationship between flow rates and ratio

ratio	O_2 flow (sccm)	Ti carrier flow (sccm)	N_2 balance gas flow (sccm)	Total gas flow (sccm)
0.5	80	160	160	400
	200	400	400	1000
1.0	280	280	140	700
1.5	240	160	0	400
	600	400	0	1000

3.1.4 Lead Oxide

Si<100> or SiO_2-coated Si wafers together with the final CVD system configuration described in §3.1.1 were used for this work. One film was deposited

onto a Pt layer (described in §3.4). To understand the effect of exchanging the PbEt for TIP, the source temperature was varied over a series of runs and then the relative proportion of oxygen to Pb vapour was varied for another set (Appendix D). To better understand the mechanisms involved with the deposition of lead oxide, changes to the substrate temperature and system pressure were also studied (Table XIII). The heater was upgraded to an 80 mm version prior to starting this phase of the work and hence a higher substrate temperature of 515°C was possible. The details of the experimental conditions for these runs are given in Appendix D.

Table XIII: Parameter limits on lead oxide experiments

setting	substrate temperature (°C)	pressure (Torr)	Pb source temperature (°C)	ratio of O_2 to Pb carrier flow
low	400	1	-15	0.167
high	515	3	+15	2

3.1.5 Lead Titanate

All the $PbTiO_3$ depositions were performed with the final hardware configuration of the system as described in §3.1.1. These runs were conducted with a substrate temperature of 515°C, a total flow of 900 sccm and a system pressure of 1.1 Torr for 20 min. or 1 hr. unless otherwise specified (Table XIV, details in Appendix E). The process development was carried out with Si <100> or SiO_2-coated wafers. In combining the lead and titanium oxide deposition together, the main goal was to obtain a 1:1 ratio between the Ti and Pb in the resultant film; that

is, to achieve stoichiometric $PbTiO_3$. Slight excess Pb has been considered advantageous by researchers [Dormans et al. 1991, Okuyama and Hamakawa 1985] who have studied the effects of post-growth annealing treatments.

Table XIV: Variation in deposition parameters for lead-titanium oxide films

TIP bubbler temperature (°C)	TIP carrier flow (sccm)	PbEt bubbler temperature (°C)	PbEt carrier flow (sccm)	O_2 flow (sccm)
35	50	0	50	300
45	300	20	300	550

The final set of films in this work were less than 0.5 μm thick to allow electrical characterization using the standard 5 V technology. These films were deposited onto the SiO_2-coated Si wafers or onto the Pt films described in §3.4. Ideally, such films would be achieved from a 20 to 30 min deposition period to allow sufficient time for stabilization of the process conditions while still obtaining reasonable throughput for subsequent implementation in a manufacturing environment. A range of TIP carrier flow rates and annealing conditions were used for the final set of $PbTiO_3$ samples (Table XV; details Appendix F).

3.2 Sol-Gel Films of Lead Titanate

Two precursors, lead acetate, $Pb(CH_3CO_2)_2{\cdot}3H_2O$ and TIP were used. These were mixed according to the procedure described elsewhere [Yi et al. 1988] in the same ratios as PZT simply with the omission of the Zr precursor. The substrates

were identical to those described in Table XVI. Prior to spinning the gel, these substrates were given an RTA of 400°C for 90 s in O_2 ambient. Two layers were spun in turn at 5000 rpm for 10 s and baked on a conveyor belt track at 100°C for 30 s in air and followed by a RTA at 400°C for 90 s in O_2 ambient. After the second layer was annealed, without removal from the system, the wafer was given a higher temperature anneal at 650°C for 30 s, again in an O_2 atmosphere.

Table XV: Parameters for $PbTiO_3$

Parameters	PbEt	TIP
Temperature (°C)	0	35
Partial Pressure (mTorr)	~200	297
Flow Rate (sccm)	300	175 to 190
Carrier Gas	N_2	N_2
Substrate Temperature (°C)	515	
Deposition Time (hr)	0.3	(60% of shortest time previously reported, Dormans et al. 1992)
Oxygen Source Gas	O_2	
Oxygen Flow Rate (sccm)	410-425	
Total Flow (sccm)	900	
System Pressure (Torr)	1.1	(30% of previously reported lowest pressure, Dormans et al. 1992)
Substrate	100 nm Pt on 50 nm of Ti on 100 nm of SiO_2 or Si(100) substrate	
Anneal	none or 490-698°C/40 s/O_2 or N_2 RTA	

3.3 Analytical Techniques

Analysis was carried out on the CVD films as-deposited and after an RTA of 615°C for 40 s unless otherwise specified.

The film composition was established by EMPA. This was carried out with an accelerating voltage of 6 or 15kV (depending on film thickness) at a beam current of 50 nA using a JEOL-8600 electron microprobe equipped with a Tracor Northern detector. Chemical analyses were obtained by wavelength dispersion analyses using the following standards and the α x-ray lines as specified: C (K), Ti (K), Pb (M), Pt (M) and Fe_2O_3 (K line for O). Data was averaged over ten locations and corrected using Tracor Northern's ϕPZ correction program. This program corrected for the combination of three factors: atomic number, absorption and fluorescence. The EDS technique was also used to determine the film composition and compared to the EMPA measurements. XRD, electron diffraction and Raman spectroscopy were used for phase identification. As a quick indicator of film thickness, the relative height of the Ti Kα peak to the Si Kα was assessed from the EDS spectra. Film thicknesses were measured using SEM and/or TEM cross-sections. The surface morphology of the films in terms of microcracking, porosity, and roughness was examined using SEM. The interfacial regions and film structure were examined using TEM in the imaging, diffraction and EDS modes.

3.3.1 X-Ray Diffraction (XRD)

X-ray diffraction data was collected on a Siemens D500 (Cu Kα source)

diffractometer in the θ-2θ and grazing incidence configuration. The θ-2θ mode was used for the powder samples described in §3.3.4, while the thin films were examined in the GA mode. The grazing incidence attachment was equipped with 0.1° divergence soller slits and a LiF (100) monochromator crystal and was used in parallel mode configuration. Operating parameters of 45 kV and 40 mA were used and acquisitions were carried out using a 1 to 4 s dwell time and a step size of 0.05°. A reflecting incident beam of less than 5° from the plane of the sample was used to irradiate the specimen. A fixed GA of 2° was used except where other values are specified. The samples analyzed were approximately 15 by 51 mm in size and were mounted in a customized jig for holding samples with the thickness of standard 100 mm diameter Si wafers.

The resultant spectra were compared against standards created from powders of known composition and patterns found in the JCPDS. The components considered when searching for a suitable match included Ti, Pb, O, Pt, Si, N, C and their compounds, totalling 245 patterns from the JCPDS database [1992]. Phase identification was aided through the use of the Siemens system and μPDSM (Fein-Marquart Associates) software packages in conjunction with the International Centre for Diffraction Data's JCPDS.

3.3.2 Scanning Electron Microscopy (SEM)

Two scanning electron microscopes were used in conjunction with this work. The first was a Cambridge Instruments, Stereoscan 360IXP, equipped with a four-

quadrant back-scattered detector and a Link EDS system. The microanalysis system (model QX2000) included an LZ-4 light element detector (with three positions for a choice of a standard 8 μm Be window, ultra thin (aluminized mylar) window, or windowless operating mode). The accelerating voltage was variable from 0.2 to 40kV and it operated with either a LaB_6 or W-filament electron source. The second instrument used was a Hitachi S-4500 field emission scanning electron microscope. It allowed for higher resolution to examine thin layers and low keV operation thereby enhancing the atomic number contrast.

Cross-sectional samples were prepared by the standard technique used in the semiconductor industry, namely, cleaving. To more readily see the TiO_2 interface some films were deposited first on SiO_2 (on Si) and a delineation etch of 6:1 buffered HF for 15 s was used. Each sample was mounted on a SEM stub using conductive carbon paint (SPI Supplies of Structure Probe, Inc., West Chester, PA 19381) and some were coated using an Emscope SC500 with 2-7 nm of Au/Pd to prevent charging. Images were normally recorded at various magnifications in secondary electron emission (SEI) mode and sometimes in backscattered electron emission (BSE) mode. The images were recorded on Polaroid 53S film.

Spectra from EDS analysis were recorded for different samples under various operating conditions as each purpose dictated, however when direct comparisons of any results were drawn the operating conditions were identical. The dead time for the analysis was maintained at a consistent and fairly low level (<20%) across all of the acquisitions. For example, the typical settings used were an accelerating gun

voltage of 12 or 20 keV and a probe current of 100 or 200 pA. For a probe current of 100 pA, the spot size would be ~10-15 nm.

3.3.3 Transmission Electron Microscopy (TEM)

Cross-sectional TEM samples were prepared using standard ion milling techniques [Chang et al. 1988]. As some of the samples delaminated, they were prepared using a modification of the above technique [Weaver and Mayer 1994, Reaney et al. 1994]. Plan-view samples were prepared by first mechanically polishing and finally ion thinning from the backside of the Si substrate. Ion thinning was performed from one side only until the near surface region was electron transparent. To look at regions farther into the film, some thinning from the front-side to remove the top few atomic layers was necessary. The samples were examined using a JEOL 2000 FX scanning transmission electron microscope (STEM). EDS spectra were acquired using an AN-10,000 Link system equipped with a high take-off angle detector and thin (Al-coated mylar) window. Selected area diffraction (SAD) and micro-diffraction were used to determine the crystalline phases present. d-spacings were calculated using eqn. (2.12) and the values given in Appendix G.

3.3.4 Raman Spectroscopy

Raman spectra were collected using an ISA MOLE S3000 Raman microprobe system. The Raman spectra were excited with the 457.9 nm line from a 5 kW Ar^+ laser. Powders prepared from bulk materials served as standards for Raman spectroscopy where references did not otherwise exist. Powder samples of PbO (litharge and massicot), PbO_2, Pb_3O_4, $PbSiO_3$, and $PbTiO_3$ were obtained from Johnson Matthey (Alfa Products, Ward Hill, MA USA). These samples were put into precision optical cells to avoid possible vapourization of the lead by the laser. The power at the powder samples was attenuated to ~200 mW and an acquisition scanning time of 50 s covering the wavenumber range from 105 to 2758 r-cm^{-1} was used. For examination of thin films, the power at the sample was attenuated to ~75mW and focused with the 100x (numerical aperature = 0.95) microscope objective. The probe beam diameter on the sample was ~2 μm. The intensities were normalized for the peak frequency of the Si optical phonon peak from the substrate wafer before contributions from the substrate were subtracted.

The effectiveness of Raman spectroscopy for phase identification of thin films of titanium and lead oxides and lead titanate was evaluated against and cross-correlated to the XRD results.

3.4 Electrical Characterization

Films fabricated with Pt bottom electrodes were electrically tested. In all cases, the Pt films were 100 nm thick on 50 nm of Ti with 100 nm SiO_2-coated Si substrates. Comparisons were drawn between Pt films deposited by different deposition methods and from different manufacturers (Table XVI). All the Pt films in this study were deposited without additional heating of the substrates. The MCNC wafers underwent a standard semiconductor clean to remove any particulates (solvent

clean followed by a wafer piranha*) before the *in situ* metal depositions. The total thickness of the MCNC Pt and Ti layers were measured as 147 nm using a profilometer (and later by TEM). The sheet resistance was 1.95 Ω/□ as measured with a four-point probe. The NTEL Pt substrates underwent a 400°C, 90 s anneal in O_2 prior to sol gel deposition to remove any organics which might be present on the surface.

Table XVI: Matrix of bottom electrodes

Ferroelectric Deposition Method	CVD			sol-gel
Pt Manufacturer	BNR	MCNC	NTEL	
Deposition Method for Pt layer	evaporation		sputtering	

Circular top electrodes of Au or Al were deposited by evaporation. Nominal diameters of the Au or Al electrical "dots" were 155 μm for fine dots, 369 μm for medium sized dots and 516 μm for large dots. Some of the electrodes were "hardened" at ~100°C for 30 minutes in an air furnace, which has been shown to improve the initial electrical measurements [Johnson 1990]. Unannealed Au electrodes have better fatigue characteristics and Al electrodes were better able to withstand the higher voltage testing [Johnson 1990].

---

* A standard semiconductor cleaning procedure.

An electrical set-up allowing measurement of ferroelectric (large signal) and dielectric (small signal) properties as a function of applied voltage amplitude, frequency, and number of polarization reversals was used. The ferroelectric measurements were made using a standard Sawyer-Tower circuit [Johnson 1990] (figure 15) composed of an HP8904A frequency generator for producing a switching signal, usually a sinusoidal wave amplified by a KEPCO 100-1M bipolar operational amplifier; an HP5316B counter for tracking cycles; a capacitor for integration of the charge collected on the device under test; and an HP54501A digital oscilloscope for concurrent observation of the results. The internal resistance of the oscilloscope was 1 MΩ and internal capacitance was 16 pF. An integration capacitor of 0.1 μF was used for high frequency measurements, while an electronic integrator was used instead for low frequency measurements.

A relay allowed the electrical set-up to be switched over for dielectric measurements. An HP4284A inductance-capacitance-resistance (LCR) meter with a frequency range of 20 Hz to 1 MHz was used. The entire system was computer controlled allowing versatility in measurements and recording of results on disc.

4.0 RESULTS AND DISCUSSION

4.1 Titanium Oxide

4.1.1 Traditional System Configuration

Using the conventional (hot-wall) set-up described in §3.1.1, the initial runs (which included matrix one) were performed. The film deposition rate rapidly decreased with increasing temperature because at elevated temperatures almost all the deposition occurred in the distribution manifold before reaching the wafers. For most of the 300°C runs, anatase was deposited (Table XVII); at 450°C (the one mid-point of the conditions used in matrix one), a Ti-rich film with some O and N incorporation was deposited; and at 600°C, either a Ti-rich film or no deposit occurred on the wafers. Ti-rich films were produced because the O_2 supply was insufficient for the complete oxidation of the Ti at the given rate of the reaction. Overall, the best results in terms of obtaining a pure TiO_x film were found at the conditions of low pressure, low substrate temperature and low total flow. The relative amounts of O_2 and TIP and the TIP source temperature were found to be unimportant in terms of the quality of the films produced in this study, using the ranges specified in Table XI (§3.1.3).

However, two problems introduced inconsistencies into the results. The first was the accumulation of TIP liquid in the lines as a result of excessive (400 sccm) flow through the bubbler forcing liquid along with vapour through the distribution network. It was difficult to remove the residue from the lines completely and this affected the thickness of film deposition in subsequent runs. A problem with the 450 cc cylinder of TIP which became gradually worse during the course of the experiments was the second issue affecting reproducibility. This problem was only identified at a late stage of this project and the manufacturers were unable to provide an explanation for its malfunction. The cause of the problem remained unresolved but was remedied by emptying the cylinder and re-filling it with new chemical before further use.

The results up to this point demonstrated a problem with the reaction kinetics preventing a reasonable thickness of deposit (on the substrates) which in turn initiated changes in the hardware configuration.

4.1.2 Modified Titanium Distribution

The modified Ti distribution was employed for the next series of runs (which included matrix two). At 300°C, deposition occurred on the wafers with a depletion effect being observed along the length of the furnace. The films deposited had an anatase crystal structure and were very thin (up to 200 nm) with fair uniformity both across-the-wafer and from wafer-to-wafer in the first boat. Reproducibility from run-to-run was much better than with the previous set-up.

Matrix two was conducted to explore the effect of different flow rates, temperatures and pressures. The effect of system temperature was more pronounced than in matrix one. All the runs at 400°C and the single run at 350°C resulted in no deposit on the wafers. At 300°C and low pressure, uniform films of anatase were deposited on the wafers in the first boat; however, at high pressure, a "bull's-eye" pattern indicating thickness non-uniformity and visually hazy films resulted. A series of runs were also conducted to explore the effect of temperature from 300 to 340°C. Increased temperature had the same effect as elevated pressures in that a "bull's-eye" pattern of colours was created and a haze attributable directly to greater film

thicknesses occurred. Also, different O_2 and N_2 flows were examined but no change in the deposition was discernable which supports the pyrolytic decomposition mechanism described in Okada's paper [1988]. The distance between the boats and the showerhead was varied and it was found that with greater spacing, the resulting film thickness was much less uniform. At a substrate temperature of 340°C, the spacing between the wafers was varied: more closely spaced wafers resulted in a loss of uniformity suggesting a transport limited regime where having equal flux is of primary importance. To explore this aspect further, a tunnel was created at the end of the showerhead before the first wafer. This resulted in a fairly uniform film in the central region with marked non-uniformity only very near the edges. This enhancement was incorporated in the subsequent diffuser plate configuration.

Table XVII: Characteristics of titanium oxide films

Matrix	Conditions	Thickness: SEM (μm)	Structure: XRD	Structure: Raman
1	conventional configuration	<0.1	anatase	anatase
-	new wafer configuration	0.119	anatase	anatase
2	single wafer	0.074	anatase	anatase
3	heated substrate	4.57	anatase	anatase
3	heated substrate	0.590	anatase	anatase
3	heated substrate	11.1	anatase	anatase
-	standard run	1.12[a]	anatase	anatase
-	repeat run	0.400	anatase	anatase
-	standard run	2.13	anatase	anatase
-	SiO_2 substrate	0.39[a]	anatase	anatase
-	Pt substrate	0.284[a]	amorphous	anatase

[a]TEM value was used instead of the SEM measurement

All the studies discussed (in §2.4.1) have involved cold-wall systems. The low film deposition rate associated with the pyrolytic decomposition of TIP suggests that a hot-wall system would not be feasible for this process.

4.1.3 Heated Substrate

A heated substrate (cold-wall reactor geometry) was used for the remainder of the runs to overcome the difficulties experienced at temperatures over 350°C with the hot-wall system. An initial set of experiments were carried out to explore the effects of spacing between the showerhead and wafer, substrate temperature, and adding O_2 into the tubular arrangement with the TIP rather than flowing the O_2 through a conventional manifold. With very close spacing (~1 cm) an imprint of the

showerhead was made directly on the wafer giving 49 spots of deposit (figure 20), while at larger spacings (≥4 cm), a "bull's-eye" pattern was produced with the thickest deposit in the central region. At 400°C, films up to 2.5 μm thick were deposited; these were considerably thicker than previous films obtained at 300°C. The change in O_2 arrangement may have resulted in greater turbulence and mixing of the gas flow before the showerhead. Unfortunately some of the results of these sets of experiments were inconclusive due to reproducibility problems caused by an empty TIP cylinder* and difficulty in accurately controlling the spacing between the showerhead and wafer. The latter problem was eliminated by affixing feet to the heater insert thereby making its support independent from that of the distribution tube, allowing placement of each independently.

The modification (described in §3.1.1) to the diffuser plate (figure 18) was added to the heated substrate and with this set-up, matrix three of the titanium oxide depositions (Table XI) was carried out. The new arrangement of a heated substrate permitted the use of temperatures up to 515°C. The dependence of TiO_2 growth rate was then investigated more thoroughly. An apparent activation energy of 71 ±6 kJ.mol^{-1} at 0.6 Torr was obtained for the deposition process using eqn. 2.5 (from §2.4) (figure 21). This value compares favourably with those given in the literature: 53 kJ.mol^{-1} for 2 Torr [Okada et al. 1989] and 63 kJ.mol^{-1} for 0.6 Torr [Siefering and

---

* Due to the physical arrangement there was no way in which to measure the cylinder contents without disconnecting the cylinder from the system. Without an accurate estimate of the chemical usage, it was not possible to gauge when the total consumption of the TIP liquid would occur. Unfortunately, there was not an abrupt end to the TiO_2 deposition, but rather a tapering off.

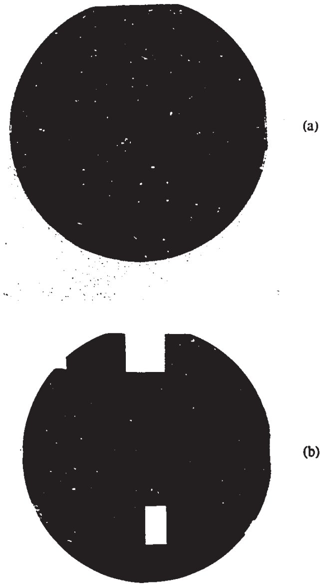

Figure 20: Two photographs of wafers deposited with TiO_2 showing the imprint of the showerhead's 49 holes. This effect is more pronounced in (b) where the distance between the wafer and showerhead was reduced. Some regions of wafer (b) were removed for SEM analysis.

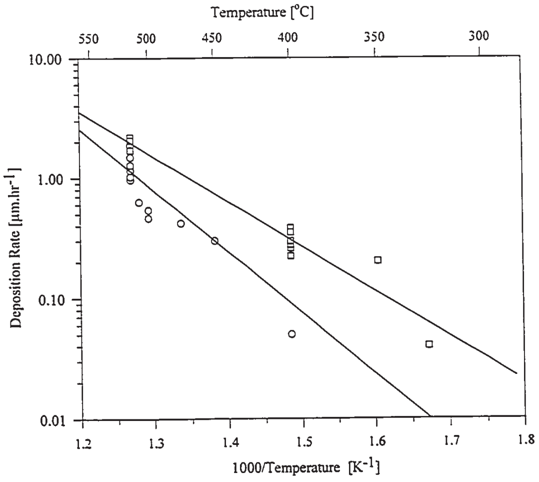

Figure 21: Arrhenius plot showing the inverse of substrate temperature versus the deposition rate for TiO_2 (□) and PbO_x (○). The apparent activation energies for TiO_2 and PbO_x deposition are 71 and 97 kJ-mol^{-1} respectively.

Griffin 1990]. At higher pressures, the growth rate was zero order and at lower pressures it was second order. These results (figure 22) correspond to those reported by Siefering and Griffin [1990a].

Film thicknesses varied from 38 nm to 15 μm. Films could be categorized according to their appearance: transparent, white haze (fully reflective), dull black or grey haze. These optical qualities were then related to film thickness: transparent films were <0.3 μm, white hazy films were ~0.4-0.7 μm, while opaque films were >4.5 μm thick.

Raman spectroscopy indicated that all the titanium oxide films had the anatase crystal structure. This result was verified in all but one case by XRD (Table XVII). XRD is less sensitive to the anatase structure and for the very disordered structure (in the case of the Pt substrate) only indicated that it was an amorphous phase. As Raman is insensitive to the presence of metals, XRD was also performed to check for pure Ti. All of the Ti was bound to oxygen and the formation of only anatase was verified. EDS also showed the films contained only Ti and O; the absence of C and N contamination was confirmed by AES.

Variations due to changes in O_2 flow, system pressure and TIP temperature were secondary to the effect of substrate temperature. Samples deposited at 400°C had an average deposition rate of 340 nm.hr^{-1} and no obvious preferred orientation when compared to the JCPDS anatase standard (21-1272), while the equivalent 515°C depositions resulted in almost 6 times the deposition rate, 1.922 μm.hr^{-1} and these films had a strong (211) reflection indicating a preferred orientation (figure 23).

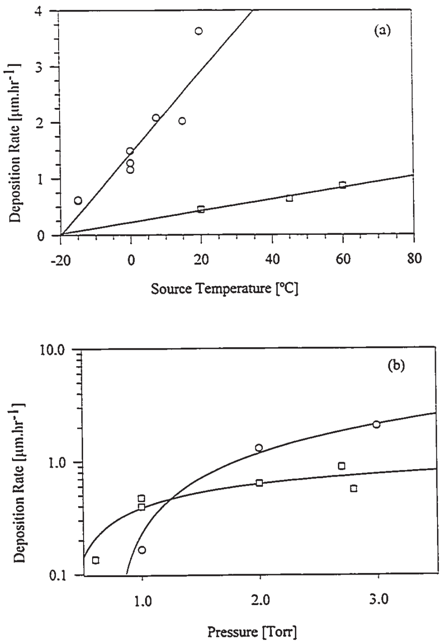

Figure 22: Deposition rate increases with (a) source temperature and (b) pressure for TiO_2 □ and PbO_x ○. The spread in the PbO_x data at 0°C indicates the variation of deposition rate with system changes (which caused minor fluctuations in the substrate temperature). To show the significant trends, data is only provided for runs executed in close succession.

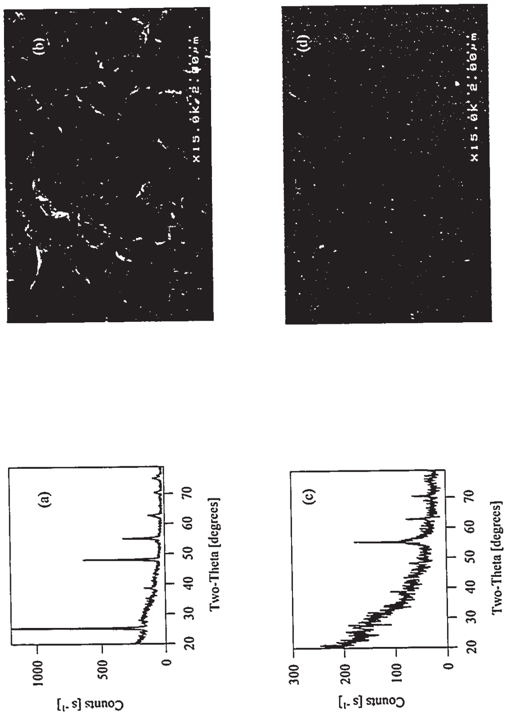

Figure 23: XRD indicates (a) no preferred orientation for the 400°C film and (c) a (211) preferred orientation for the 515°C film. The corresponding SEM images for the (b) 400°C and (d) 515°C films are shown.

The value of 76 obtained for the permittivity from measurements of the TiO_2 film annealed at 585°C for 40 s was in keeping with those quoted in the literature (Table XVIII). Permittivities of this magnitude have application in high dielectric capacitors where materials which are simple, familiar and 'safe' are desired. In comparison to Pb-based compounds which can give problems due to diffusion or lab handling procedures, TiO_2 is a 'safe' material.

It was not surprising that the films were anatase as-deposited, as other studies have found the same result for films deposited at low temperatures (~400°C) (§2.4.1). Rapid thermal annealing (RTA) in N_2 was done at progressively higher temperatures in 25°C increments for 40 s starting with a temperature of 515°C. Samples were cooled to at least 200°C between anneals. Even after annealing at 1061°C*, no indication of rutile formation was detectable by XRD (figure 24). The literature is quite contradictory but suggests that the transition from anatase to rutile could begin at temperatures as low as 200-650°C and is sometimes complete for temperatures in the range of 800-1100°C. Unlike furnace annealing; the shorter anneal times used here (40 s at 1061°C, or ~15 min cumulative at ≥515°C) may have been insufficient to cause the transition. In one study [Wicaksana et al. 1992], it was observed that the likelihood of forming rutile upon further annealing was decreased as a result of lower deposition temperatures used initially.

---

* This was the maximum temperature possible with the available RTA system.

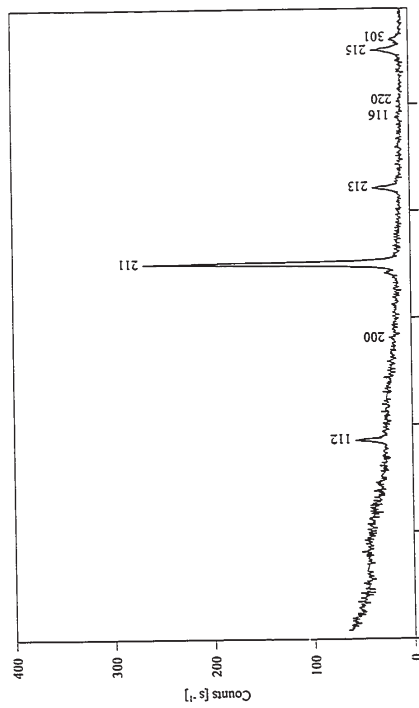

Figure 24: XRD spectrum of a TiO_2 sample annealed at 1061°C shows a dominance of anatase and no indication of rutile.

4.2 Lead Oxide

Primarily three types of lead oxide were deposited either singly or in combination with each other. The deposition parameters used in this work bridged the pressure-temperature region where previous work suggests either form of PbO (litharge or massicot) could be produced (figure 25). As well, some films had oxygen-rich compositions which resulted in PbO_2 (scrutinyite) being formed along with the litharge or massicot (figure 26).

Table XVIII: Values of permittivity- Comparison of literature with experimental results

Material	Literature	Frequency (Hz)	Measurement	Frequency (Hz)
SiO_2	3.78[a]	10^2-10^{10}	-	10^3
TiO_2	14-110[b]	10^6	76	10^6
PbO	25.9[b]	10^8	*	-
$PbTiO_3$ thin film	30-290[c-f]	10^3	58-155	10^3
$PbTiO_3$ commercial ceramic	210[c]	-	-	-
PZT thin film	~1000[f]	-	-	-
PZT commercial ceramic	700-3400[c,f]	10^3	-	-

[a] Hench 1990
[b] CRC 1980-81
[c] Swartz 1990
[d] Shimizu et al. 1991, Chen et al. 1992
[e] Kwak et al. 1992
[f] Sayer et al. 1992

* It was not possible to obtain a value for the PbO film because the porosity of the film resulted in shorting to the substrate.

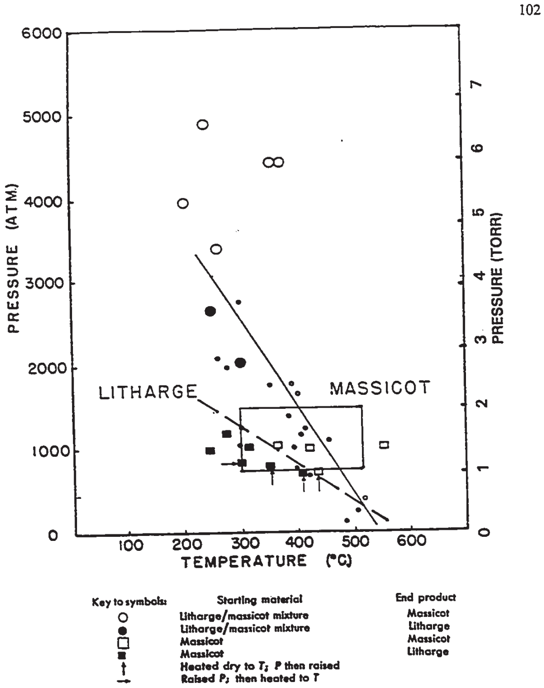

Figure 25: A pressure-temperature curve for the litharge-massicot reaction [White et al. 1961]. The solid line selected by the original authors indicates the division between the two compounds based on all their data. Added here is a second line, shown dashed, indicating an alternate division when the starting material is massicot. The outlined box highlights the major region examined herein. Reprinted with permission from the American Ceramic Society.

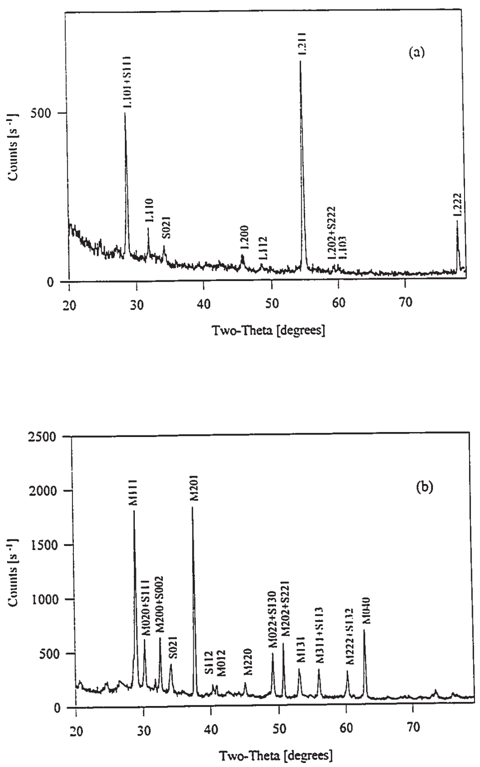

Figure 26: XRD spectra of (a) a sample of litharge (L) and (b) a sample of massicot (M), each containing a significant amount of PbO_2 (S-scrutinyite).

Using colour for identification of the type of lead oxide was only possible with very thick films (>2 μm). For films of 0.5-2 μm in thickness, their appearance varied from white haze to opaque grey, while films less than 0.5 μm thick usually had interference colour variation according to changes in film thickness and/or refractive index.

The deposition rate increased as either the substrate or PbEt temperature, or pressure rose (figures 21 and 22). An apparent activation energy of 97±15 $kJ.mol^{-1}$ at 2 Torr was calculated using eqn 2.5 (figure 21). This value is slightly higher than the value of 78 $kJ.mol^{-1}$ found by Okada [1989] at 6 Torr. It is difficult to compare deposition rates when the type of deposit and hence, the measured film thickness vary so markedly. It was expected from the literature [Okada et al. 1989] that the lead oxide deposition rate would increase significantly with O_2 flow since the reaction mechanism is believed to be oxidation (unlike the TiO_2 deposition process). This was indeed the case, until the O_2 flow was doubled to 600 sccm and then a marked decrease in deposition rate occurred. This change was also associated with a change in morphology. For all the deposition parameters examined, five distinct types of morphology were observed (figure 27). Two of these deposits were characterized most clearly by isolated regions of growth, however, it was apparent that with increased deposition time, the first observed pattern of the deposit would prevail (figure 28). Other researchers have observed that lead oxide showed "definite selective deposition" and found "lead [oxide] could not be deposited on SiO_2" but formed readily on metallic surfaces [Greenwald et al. 1992]. Further analysis of the

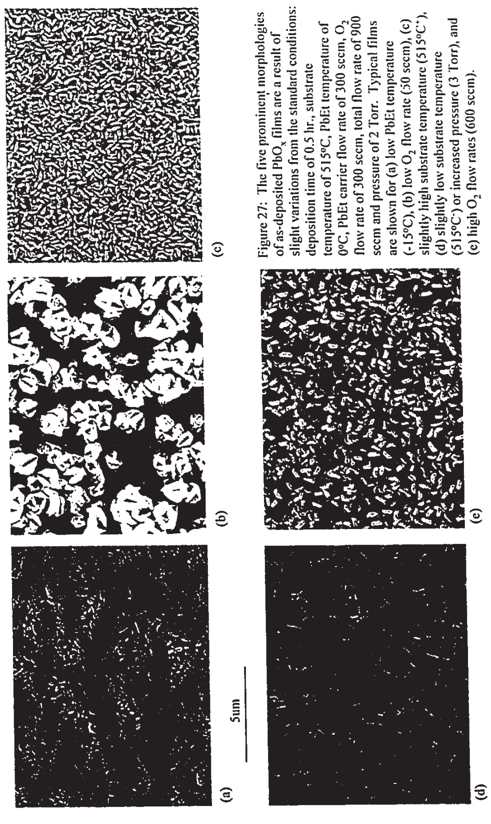

Figure 27: The five prominent morphologies of as-deposited PbO_x films are a result of slight variations from the standard conditions: deposition time of 0.5 hr., substrate temperature of 515°C, PbEt temperature of 0°C, PbEt carrier flow rate of 300 sccm, O_2 flow rate of 300 sccm, total flow rate of 900 sccm and pressure of 2 Torr. Typical films are shown for (a) low PbEt temperature (-15°C), (b) low O_2 flow rate (50 sccm), (c) slightly high substrate temperature (515°C⁺), (d) slightly low substrate temperature (515°C⁻) or increased pressure (3 Torr), and (e) high O_2 flow rates (600 sccm).

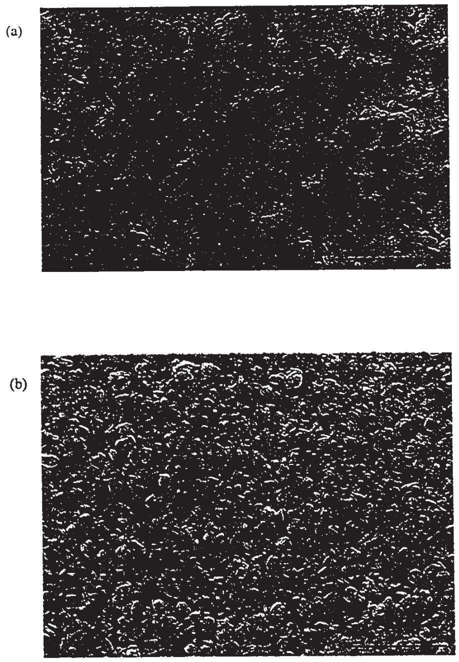

Figure 28: Variations in deposition parameters cause more complete coverage: (a) illustrates more complete coverage of figure 27a (at a higher PbEt temperature of +15°C) and similarly (b) corresponds to figure 27b and is the result of an increased O_2 flow rate.

films by SEM or TEM cross-sectional analysis indicated that layer growth often preceded island formation. In §2.4.2 island growth and layer plus island growth was discussed briefly. At the lower substrate temperatures, either very little deposit occurred or the irregular growth patterns shown in figure 27b or 27e were observed. Similarly at low PbEt temperatures (-15°C), growth was negligible or assumed the pattern depicted in figure 27a.

The increase in deposition rate with source temperature (for both TiO_2 and PbO_x films) was the result of a chain of reactions as described below. Increases in source temperature resulted in more vapour production and hence more vapour collection by the carrier gas. Consequently more material was deposited. As neither curve presented in figure 22 levelled off, the limit in terms of increasing the deposition rate had not been reached for the range of temperatures studied. This result means that both liquid source temperatures affected the deposition rate. Examination of the vapour pressure relationship for TIP [Siefering and Griffin 1990] and PbEt [CRC 1993] for temperatures mostly higher than those used in this study show a continued increase in vapour pressure with temperature (figure 29). These trends suggest higher deposition rates could easily be obtained for either TiO_2 or PbO_x by increasing the source temperature further. However, the fact that the partial pressure varies with the temperature implies a high sensitivity to source temperature fluctuations and hence potential problems in process control.

TEM cross-sectional examination indicated that interactions between the film and silicon occurred for both the oxide coated (figure 30) and uncoated wafers during

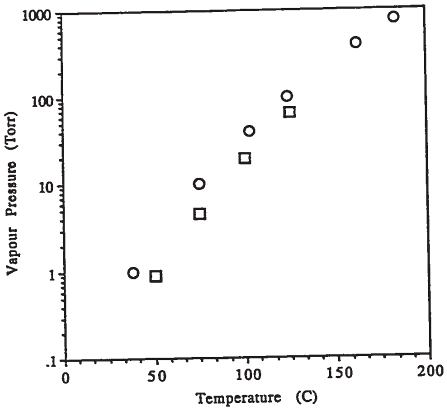

Figure 29: Vapour pressure relationship for TIP □ and PbEt ○.

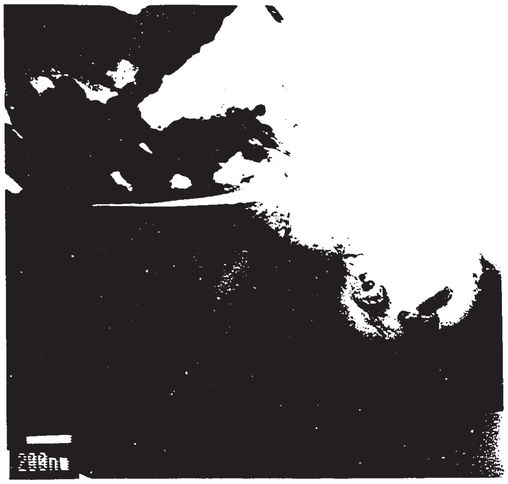

Figure 30: Interaction of the deposited film with a SiO_2-coated Si wafer is shown in this TEM image. This effect was also observed for uncoated Si substrates and was intensified by post-deposition annealing.

the PbO_x deposition. In both cases, the interface became uneven (or wavy) and when an SiO_2 layer was present, it was pitted with Pb-rich areas. This effect was further intensified by any post-deposition annealing.

As other researchers (see §2.4.2) had experienced difficulties with the quality of commercial lead oxide samples, XRD analyses was done on the powders being used for Raman standards. XRD indicated that the powder sample of litharge contained massicot impurities. However, it was still possible to obtain a defining Raman signature for comparison purposes as the difference in the excitation in spectral region of 289 r-cm^{-1} between massicot and litharge powders was sufficient to make a positive identification (Table XIX). This difference is quite pronounced for the thin film samples (figure 31).

Three specific samples are discussed in turn in the following sections; these samples represent the three types of lead oxide found: (i) litharge, (ii) litharge and scrutinyite mixture, and (iii) massicot and scrutinyite mixture.

4.2.1 Litharge

One sample examined by XRD was initially identified as α-PbO (JCPDS 35-1482) rather than litharge (as the former matched with the standard for several more reflections[1]) (figure 32). This result was contrary to the phase diagram, so the accuracy of the JCPDS standards was questioned. Using the lattice parameters given

---

[1] The number of matched reflections is a function of the error accepted on the d-spacings and whether split peaks are counted more than once.

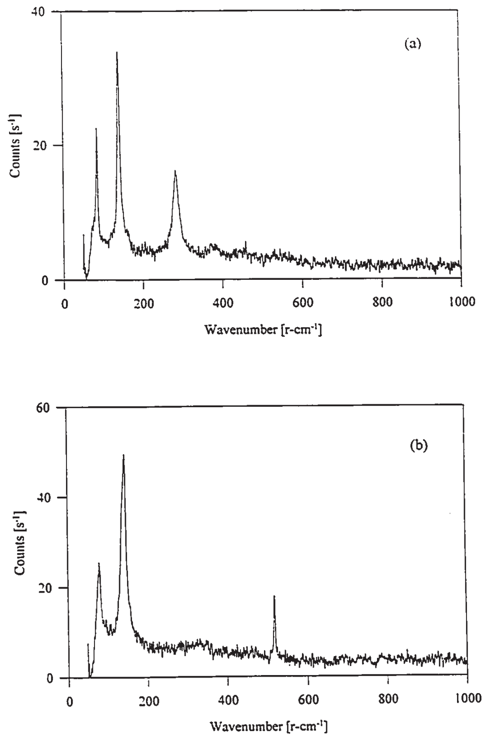

Figure 31: Raman spectra for the (a) massicot and (b) litharge thin film samples.

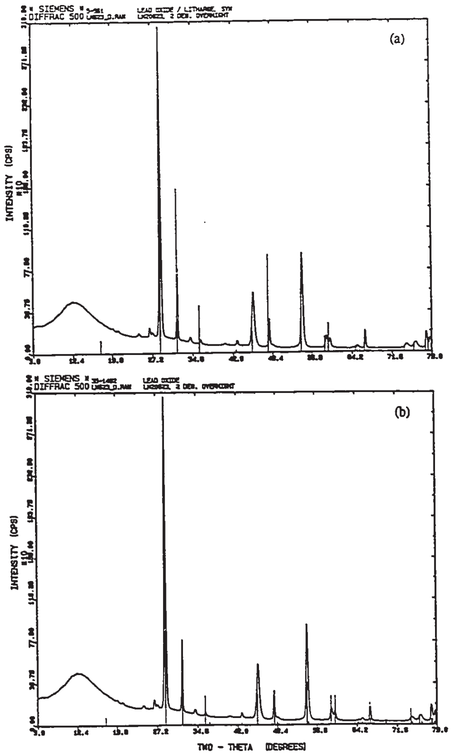

Figure 32: XRD spectrum of a lead oxide film which matches the standards for (a) litharge (5-561) and (b) α-PbO (35-1482).

in the JCPDS listing and the software package *Diffract* [*], the allowed reflections for both compounds were calculated. The simulated litharge pattern contained three additional reflections which reduced considerably the difference between the fits of the two oxides with the thin film (Appendix I). To eliminate these ambiguities, electron diffraction analyses of a cross-sectional TEM sample were carried out. Electron diffraction patterns from two zones were indexed as coming from the

Table XIX: Comparison of Raman response between litharge and massicot [Adams and Stevens 1977].

Raman Excitation (r-cm^{-1})	
Litharge	Massicot
	52 w
	72 s
~81.0	87 s
146.5	144 vvs
	171 sh
	217 vw
	250 vvw
321.5	289 vvs
~338.7	385 m
	424 m

where w=weak, s=strong, sh=shoulder and v=very

---

[*] Microdev Software, Hillsboro, Oregon, USA

<001> and <101> zones of litharge[*] (Table XX). These electron diffraction patterns compared favourably to those generated by *Diffract* (figure 33).

4.2.2 Litharge & Scrutinyite Mixture

The sample examined in depth here was grey and hazy in appearance. It was deposited at a rate of ~34 nm.min^{-1} for 30 min to form a 1.03 μm thick film. The film surface was rough due to the random placement of small, densely packed ellipsoids observed using SEM (figure 27c). This roughness was responsible for the hazy appearance of the film.

EDS indicated the presence of Pb and O and the absence of C. Atomic concentrations measured by EMPA analysis were: Si 3.84% (coming from the substrate by diffusion), Pb 45.30%, Ti 0.14%, O 50.70% all with a standard deviation of less than 1% across the sample (Appendix J). Since coating of the EMPA samples precluded further analysis for C, the EDS result had to be confirmed by AES analysis. No C was present within the detection limits of AES (>0.1 at.%) [Ingrey et al. 1982]. The level of Ti contamination found was very low in this sample so it would not be a serious obstacle for making reproducible $PbTiO_3$ films, if the assumption that other films would show similar trends held true. It is believed that the Ti came from cross-contamination of the reactant line due to previous TiO_2 depositions. A Pb:O ratio of 1:1.12 translates to an 88% PbO and 12% PbO_2

---

[*] These patterns could also be indexed in terms of α-PbO as <001> and <112>, however XRD indicated that neither of these zones were very prevalent in the film.

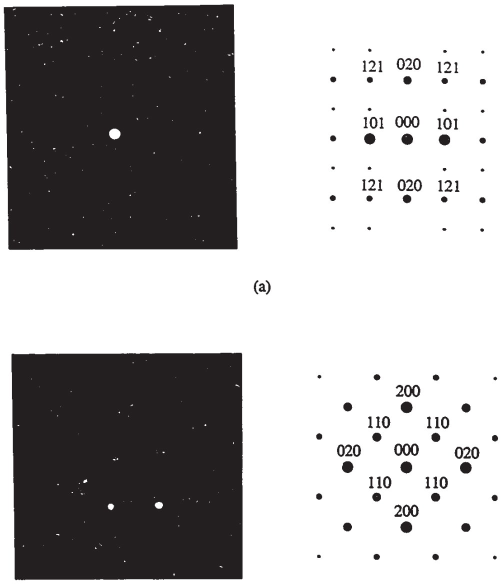

(a)

(b)

Figure 33: Experimental and simulated micro-diffraction patterns from litharge (a) <011> and (b) <001>

composition for the film if the Si and Ti are neglected.

Depth profiling using XRD for this sample produced a very complex array of reflections (figure 34). The GA mode was used at the following angles: 0.5, 1, 1.5, 2, 5, 7.5, 15, 30 and 45 degrees, although the term "glancing angle" is strictly no longer applicable at the higher angles. Furthermore the interpretation of any line splitting at larger angles (10° or more) has to be done with care due to the geometric arrangement of the experimental set-up [Geohner & Eatough 1992]. Since Pb and some Pb-based compounds are strongly absorbing, the presence of the substrate was not evident at even the highest "glancing" angles and could only be seen in θ-2θ mode. The θ-2θ analysis indicated a predominance of litharge. The electron diffraction patterns analyzed (figure 35), along with the peak heights observed using

Table XX: Comparison of diffraction patterns to the standard for litharge (JCPDS: 5-561). Average values of the measurements taken from the micro-diffraction patterns are shown.

Zone	Reflection	Angle (°)		d-spacing [nm]	
		Standard	Pattern	Standard	Pattern
<011>	{020}	32.52	31.8	0.19850	0.197
	{121}	57.48	57.5	0.16739	0.165
	{101}			0.31143	0.314
<001>	{200}	45	45.1	0.19850	0.197
	{110}			0.28072	0.275

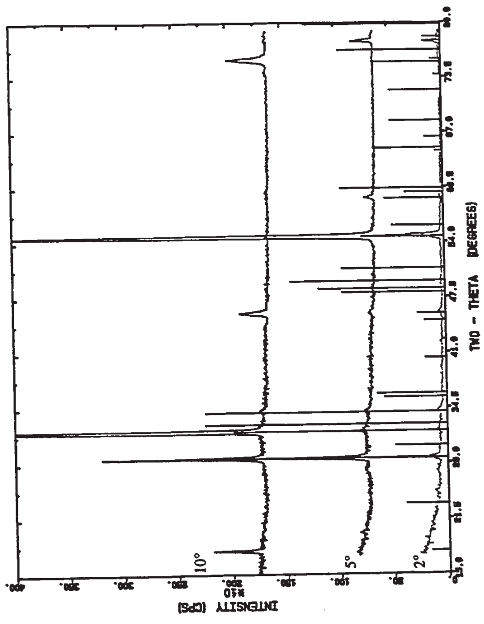

Figure 34: XRD spectra taken at glancing angles of (a) 2°, (b) 5° and (c) 10°; all indicated a mixture of litharge and scrutinyite.

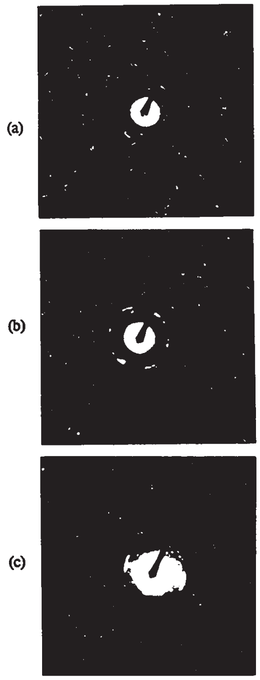

Figure 35: Electron diffraction patterns of the litharge-scrutinyite sample with the specimen tilted (a) -30°, (b) 0° and (c) +30° show preferred orientation.

GA-XRD, indicated a strong preferred orientation of the lead oxide layers. Litharge and PbO_2 were clearly identified, although in highly oriented forms. Due to overlapping peaks at one or more 2θ values (Table XXI) and strong preferred orientation, it was difficult to identify the phase changes throughout the film. The possibility of massicot and anatase was noted. Raman spectroscopy was able to verify part of the XRD findings by confirming the presence of litharge [Madsen and Weaver 1993].

Table XXI: 2θ reflections are indicated for three different glancing angles.

Glancing Angle		2° (2θ values)	5° (2θ values)	10° (2θ values)
Overlapping Reflections		**28.7**	**28.7**, 59.3	**28.7**, 75.6
Defining Reflections	PbO (litharge)	**31.8**, 45.7, **48.6**, **54.8**, 78.1	**31.8**, 45.7, **54.8**, 77.9	17.8, **31.9**, 45.8, **54.9**
	PbO_2	**34.2**	**34.3**	**32.4**, **34.2**

Major reflections (>20% maximum intensity for standards) are indicated with **bold type.**

This film, like many others, was multi-layered. The growth mode described by Joyce [1974] with a layered structure followed by an island growth was evident here. In SEM cross-section, two columnar layers producing a fairly uniform film were observed with a total thickness of ~1μm (figure 36). With TEM, an additional thin layer of 18 nm at the silicon interface was found (figure 36). The top layer, 960 nm thick, was columnar and very porous with Pb, O and Si constituents. The layer below had a thickness of 120 nm and was more uniform and much less porous in

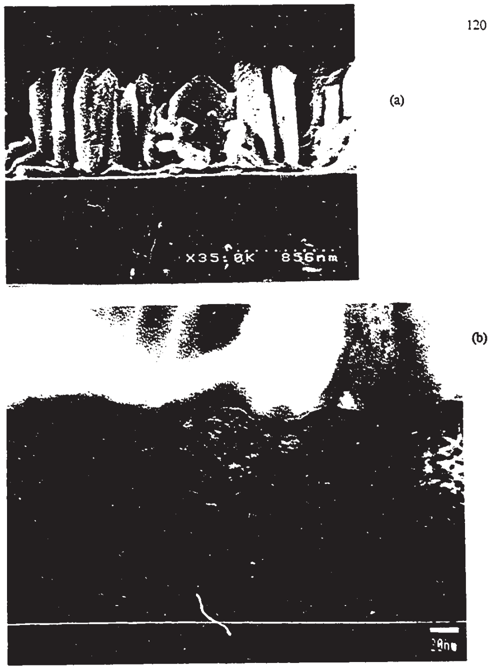

Figure 36: An SEM image in cross-section (a) shows the total film thickness of ~1 μm. A Ti-rich layer at the interface of the lead oxide samples can be seen as indicated in this TEM micrograph (b). A significant amount of radiation damage occurred as a result of the ion beam thinning techniques used in the TEM sample preparation which caused the formation of a high density of dislocation loops.

nature. The bottom layer was analyzed using EDS (figure 37) and in agreement with the EMPA results, this layer was found to contain Ti. The information obtained from AES confirmed the TEM EDS findings, namely, a thin Ti rich layer had formed on the Si substrate and the main film contained Pb, O and some Si. The Ti-rich layer had apparently served as a barrier to Pb diffusion into the substrate but did not prevent Si from diffusing outwards. This result suggests that Ti could be considered in part as a barrier structure. However, it would have to be stable (or controlled) at the temperatures required with its adjacent layers and another film would be needed for prevention of Si diffusion and reaction. Ti is commonly used in barrier structures for its adhesive properties, often obtained in part by its reaction with neighbouring layers. This reaction if controlled (or limited) is not necessarily detrimental and can alleviate problems of adhesion between highly stressed layers.

4.2.3 Massicot and Scrutinyite

Massicot films were easily identified by their yellow, opaque appearance when thick. The deposition rate found to produce massicot was quite high, 11-19 $\mu m.hr^{-1}$ compared to less than 6 $\mu m.hr^{-1}$ for other types of PbO_x films. Microscopically these films were composed of loosely packed platelets with a "tuftiness" from preferential growth sites (figure 27d). From XRD analysis it was apparent that scrutinyite often existed as a secondary phase (figure 26b).

Upon further examination of figure 25 (White et al. 1961) a second line (shown dashed) was drawn for the massicot-litharge system based on the starting

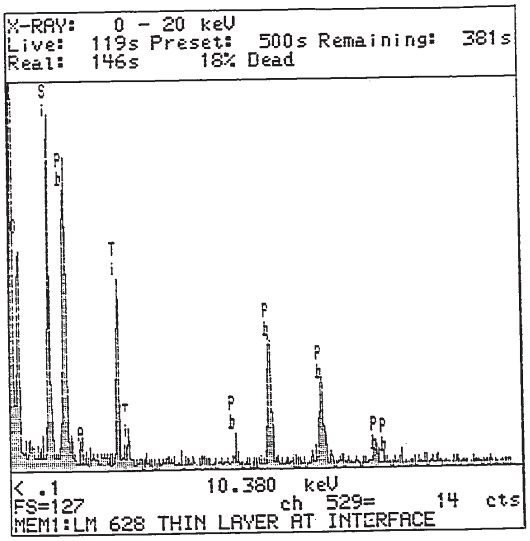

```
X-RAY:   0 - 20 keV
Live:   119s Preset:   500s Remaining:   381s
Real:   146s      18% Dead
```

```
< .1              10.380  keV
FS=127                ch  529=        14   cts
MEM1:LM 628 THIN LAYER AT INTERFACE
```

Figure 37: EDS spectra showing the presence of Ti as a contaminant, Si from the substrate, and O and Pb from the lead oxide film.

material. White and his colleagues drew one line separating the phase formation into two distinct areas on a process pressure-temperature diagram. Although they looked at two different starting materials, pure massicot and a massicot-litharge blend, they did not separate their results in terms of these two "precursors". The dashed line shown in the diagram (figure 25) indicates another pressure-temperature transition condition with massicot as the starting material. For less severe temperature-pressure conditions, massicot is the final product when the starting material is massicot. This result shows there is a tendency for the material not to transform. It is suggested that in this experiment, a small fluctuation of the substrate temperature (due to a change in the heater) at the start of the deposition process might have affected the initial film formation which in turn determined the final product. In other words, a lower starting temperature induced the initial formation of a massicot phase which promoted confirmed growth of the film as massicot.

4.3 Lead Titanate

4.3.1 Process Development

To form stoichiometric PbTiO$_3$ films with the perovskite structure, it is necessary to balance the amount of Pb and Ti incorporation in the oxide layer. As discussed in §2.4.3, this task is most easily accomplished with up to 10 at% excess Pb. The composition of the films can be manipulated through changes in the deposition temperature, system pressure, source flow rate and source temperature. The sensitivity of the deposition process of the individual oxides (TiO$_2$ and PbO$_x$) to

source temperature variations was discussed in §4.2. Other researchers have found their PbTiO$_3$ processes to be very sensitive to small fluctuations of ±0.1°C in source temperatures [Greenwald et al. 1992, de Keijser 1993]. In this study, the source temperature deviation was always less than ±0.05°C, so instead the process control is probably limited by the substrate temperature variation. Initially, the films were examined by EDS to obtain qualitative information on the film composition. After some experimentation, the following parameters were selected for further study: a deposition time of 1 hr., TIP source temperature of 35°C, PbEt source temperature of 0°C, O$_2$ flow of 300 sccm, total flow of 900 sccm, a system pressure of 1 Torr and a substrate temperature of 515°C. The two variables remaining were the TIP and PbEt (carrier gas[1]) flow rates. Using these conditions thicker films (than normally used for electrical testing) of 0.7-1.4 μm in thickness were formed in order to simplify the subsequent physical analyses and minimize the influence of interactions with the substrate[2]. The TIP flow rate was varied from 100-300 sccm and the PbEt flow rate was varied from 200-300 sccm. The as-deposited films were examined by EMPA to obtain the ratio of Ti to Pb (figure 38). The settings of 175 sccm for the TIP carrier

---

[1] Carrier flows are implied for the liquid precursors although not always explicitly stated. Ideally one would be able to provide the exact amount of the precursor flow, however, this approach has been avoided due to the inaccuracies possible with this method.

[2] The process development was carried out with SiO$_2$ coated or uncoated Si substrates rather than the more stable but expensive Pt-coated substrates. Often the deposited films, particulary the Pb-rich ones, interacted with the Si and formed silicates at the oxide or Si interface during the deposition process. This effect was intensified by any post-deposition annealing.

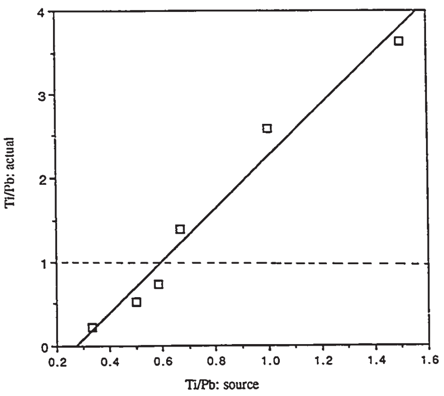

Figure 38: The ratio of the PbEt to TIP carrier flows plotted against the ratio of the composition obtained by EMPA of the resultant films. The solid line fitted to the data, y= -0.851 + 3.095 x, has an R^2 value of 0.97. The dashed line shows the desired 1:1 composition of the film.

flow rate and 300 sccm for the PbEt flow rate produced a slightly Pb-rich $PbTiO_3$ film. To bracket the optimum region, the PbEt flow rate was fixed at 300 sccm while TIP flow rates of 175, 180 and 190 were used to produce films for a more in-depth examination. Apart from the low pressure of 2 Torr used in this study, these parameters fall into the ranges used by other researchers (Table III, §2.4.3). Little investigation though, of films deposited at temperatures <550°C has been carried out in previous studies.

To help in understanding the effect of each of the reactant gases, the individual oxides were grown again using the same deposition conditions as the final $PbTiO_3$ process by substituting either TIP or PbEt with N_2. The Ti-O run resulted in an anatase film which was very columnar and had a (211) preferred orientation. The deposition rate was found to be lower than for the corresponding $PbTiO_3$ film. The Pb-O run produced a film of massicot, litharge and PbO_2 at a much higher deposition rate than for the corresponding $PbTiO_3$ run. These findings demonstrate that the interaction between the two precursors significantly alters the kinetics involved and subsequently affects the overall $PbTiO_3$ film deposition rate. These results can be contrasted to those of Okada and his colleagues [1989] since they developed their process for $PbTiO_3$ by choosing conditions from the individual oxides (TiO_2 and PbO) which gave the same deposition rate. At atmospheric pressure they found the resulting $PbTiO_3$ film thickness to be only 35-59% of the expected thickness from the individual oxides and attributed the decrease to gas phase nucleation. At a reduced pressure of 6 Torr, they found a one to one correspondence between the growth of

individual oxides (TiO_2 + PbO) and that of $PbTiO_3$ for temperatures from 450-600°C. Their experimental conditions and analysis methods differed from those used here.

The growth of $PbTiO_3$ has been qualitatively described (see §2.4.3). However it is apparent that the reaction sequence is more complicated than originally proposed in the literature since more complex phases of lead oxide are often formed. It is not possible to distinguish between the reaction sequence and changes due to the substrate heating. It is clear however that the deposition temperature is inadequate to achieve complete formation of the desired perovskite phase. This matter is discussed in more detail in §4.3.2 and 4.3.3.

4.3.2 Characterization of SiO_2-based Samples

A 400°C, Pb-Ti-O run produced a predominantly TiO_2 film. AES and initial SEM EDS analyses could not detect even a trace of Pb incorporation into the bulk of the film (figure 39). XRD analyses indicated a pure anatase film had formed, although the topology of the film observed by SEM was curiously unlike any of the other TiO_2 films (figure 40). In the SEM cross-section, dark areas observed near the surface appeared to correlate to this change in morphology (figure 40) and EDS analysis revealed Pb was present. In previous PbO_x work, this type of contrast was associated with Pb-rich regions. The only conclusion that could be drawn was that a marked reduction of Pb incorporation into the film occurred at this reduced substrate temperature. Other researchers who have investigated these very low temperatures

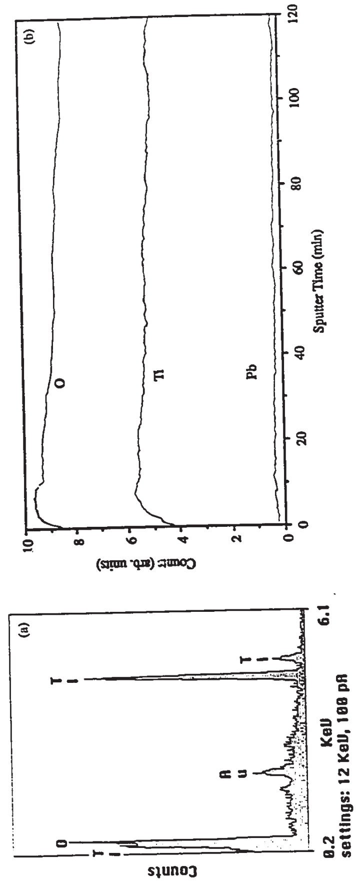

Figure 39: EDS (a) and AES (b) spectra show no evidence of Pb.

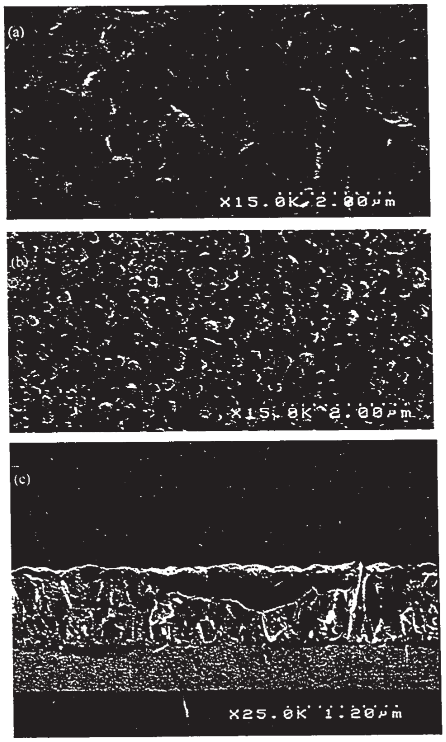

Figure 40: FE-SEM micrographs show the morphology of (a) a typical TiO_2 film and (b) a more rounded surface created with the addition of PbEt. In cross-section (c) there are dark regions near the surface of the latter film.

[Chen et al. 1992, Shimizu et al. 1991, Okada et al. 1988] have varied their deposition parameters until stoichiometric $PbTiO_3$ films have formed or have increased their substrate temperatures considerably.

Films deposited at 515°C with close to a 1:1 Pb:Ti ratio were predominantly macedonite before post-deposition annealing (figure 41). Forming perovskite films during the deposition phase is a useful feature of using an MOCVD process which is not possible with most sputtered or sol-gel processes. Temperatures of 450°C [Swartz et al. 1989], 500°C [Kwak et al. 1988], 550°C [Erbil et al. 1992], 600°C [Katayama et al. 1992] or 700°C [de Keijser et al. 1991] were used in CVD processes by other researchers to obtain the perovskite structure. To put this into perspective, the nominal setting of 515°C used in this study translates into an actual wafer temperature of 435-505°C (§3.1.1). XRD analyses suggested massicot was more likely to be present than pyrochlore ($Pb_2Ti_2O_6$) as a secondary phase (Table XXII). EMPA analyses also indicated that excess Pb was present in the films, supporting this finding.

Table XXII: d-spacing values (nm) from lead titanate films not attributable to the macedonite standard (6-452) are compared to other standard patterns.

Thin Films d-spacings (nm)	Standard for Massicot	Massicot Δ	Standard for $Pb_2Ti_2O_6$	Pyrochlore Δ
.29754 ± .00005	.29459	-.0029	.302	+.0045
.30785 ± .00005	.3068	-.0011	.315	+.0072

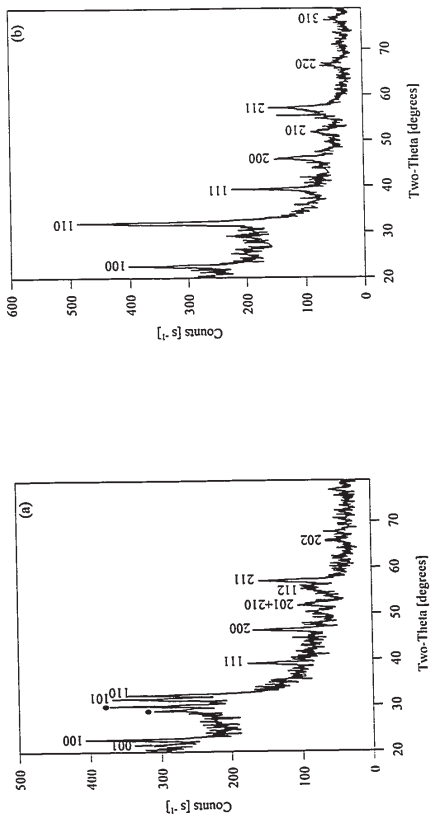

Figure 41: XRD spectra from (a) an as-deposited film with some impurities (marked ●) matches the macedonite 6-452 standard and (b) an annealed film shows a match to the cubic $PbTiO_3$ 40-99 standard.

After annealing the films deposited on Si or SiO_2 substrates, XRD indicated that films very close to a 1:1 Pb:Ti ratio transformed to the high temperature $PbTiO_3$ cubic phase (40-99) (figure 41) and remained cubic even upon cooling, while those films off stoichiometry by a greater factor were macedonite when examined after cooling. It is suggested that the interaction of the films with Si prevented the transformation back to the tetragonal phase upon cooling. The effect of contaminants on phase transitions and domain movement has been observed in other studies. For example, the stabilization of domain structures, that is the locking or pinning of the motion of domain wall boundaries, has been shown to be highly dependent on the defect structure [Lines and Glass 1972, Lambeck and Jonker 1986]. In addition, contaminants, particularly Si, raise the transition temperature of pyrochlore to that of perovskite (PZT) [Wright and Francis 1993], or inhibit the transition altogether [Madsen and Weaver 1992, Megaw 1952]. Films with large amounts of excess Pb may not have undergone the phase transformation at 615°C or the extra Pb could have served as a partial protectant from Si contamination allowing them to return to their initial tetragonal phase.

4.3.3 Pt-based Samples

Six samples were selected for an in-depth examination from the final set of $PbTiO_3$ films (Table XXIII). These six $PbTiO_3$ films represented two of the Ti:Pb ratios and all three types of Pt multi-layered substrates (§ 3.4). They were chosen such that changes in film composition and the influence of the quality of the bottom

electrode could be assessed. Visually, all $PbTiO_3$ wafers displayed the same pattern of colours (figure 42). As noted earlier (§3.1.1), the radial ring pattern was caused by the thermal gradient across the heated chuck. An additional colour variation was a result of the pattern of gas flow within the system, predominantly associated with the fact that the exhaust flow worked in opposition to the injected flow (figure 18). Wafers from 80 consecutive $PbTiO_3$ deposition runs varied little in their appearance (figure 42). Only the central 30 mm diameter region of each wafer was used in this study (due to the across wafer temperature variation). In general, uniform heating is not a problem with equipment designed for cold-wall substrate-heated systems, so this problem could be overcome with a commercial system. The average thickness of the $PbTiO_3$ films as measured by SEM or TEM was 405 nm with ±20 nm variation in the mean value from sample to sample (Table XXIII). These films typically had 30 nm sized grains with a rough topology which gave an overall typical thickness variation of ±80 nm (figure 43). This is similar to the topology observed in other studies [Okada et al. 1988, Dormans et al. 1992, Greenwald et al. 1992, Swartz et al. 1989], although one exception where smooth, non-columnar and non-fibrous films were formed has been reported [Chen et al. 1992].

XRD analysis indicated that the major phase of the films was macedonite, with a = 0.3901 nm and c = 0.41521 nm (Appendix K). There were no significant differences between these lattice parameters and those obtained from bulk ceramics (see §2.5). Macedonite accounted for over 85% of the crystalline material in the deposited film. A preferred orientation of macedonite was found for primarily the

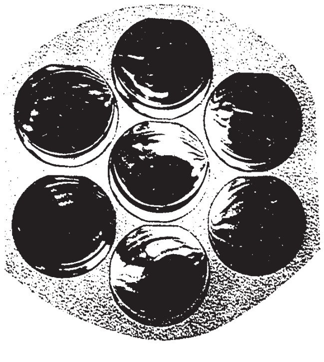

Figure 42: Photographs of seven wafers selected from over 80 depositions runs show an unusual but consistent pattern of colour (signifying variations in film thickness). Centre thicknesses vary by up to 5% from run-to-run.

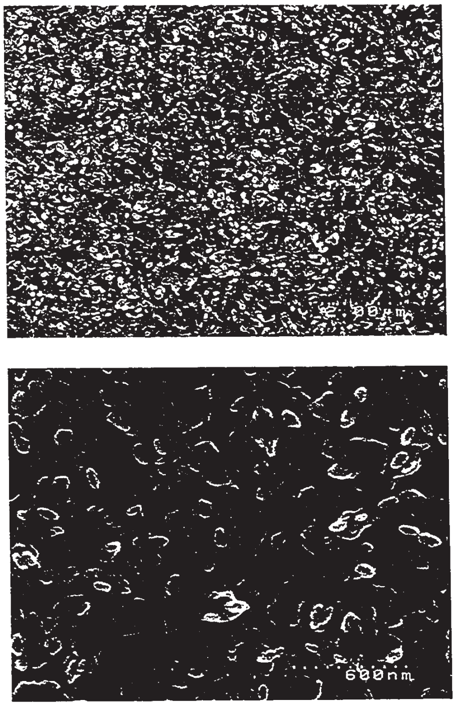

Figure 43: FE-SEM micrographs obtained using 10kV and taken at (a) 15,000 times and (b) 50,000 times are representative of the as-deposited $PbTiO_3$ films.

Table XXIII: Description of analyzed samples from the final set of films. (All deposition parameters were identical except for the TIP carrier flow which was varied as specified below).

TIP carrier flow (sccm)	Pt Source	$PbTiO_3$ film thickness (nm)
175	BNR	385 ± 35
175	MCNC	400 ± 50
175	NT	425
190	BNR	400 ± 80
190	MCNC	424 ± 72
190	NT	395 ± 35

(110), (210) and (202) families in some of the films and for the (111) family in all of the films. A glancing angle of 1.5° was used to assess the preferred orientation and avoid contributions from the underlying Pt (or Pt_3Ti) reflections at similar positions (Table XXIV). The texture coefficients for one film obtained from eqn. 2.11 are shown below (in Table XXV) where values ≤ 1 indicate no preferred orientation and values > 1 show a preferred orientation. Often c-axis oriented films are desired in order to maximize the P_r value of the films. The orientation of the substrate can be transferred to the $PbTiO_3$; for example, epitaxial films have been deposited on $KTaO_3$, $SrTiO_3$ and MgO [Chen et al. 1992. Erbil et al. 1992] and (111) oriented films have been deposited on (0001) sapphire [Katayama et al. 1992]. This is not always the case, as films with (100) preferred orientation have been formed on Pt [Swartz et al. 1989] and fused quartz [Kwak et al. 1992] and (h00) and/or (001) oriented films have also been deposited on Pt [Dormans et al. 1992]. In this study, the films were deposited onto polycrystalline Pt and consequently, the $PbTiO_3$ films

were also polycrystalline. XRD studies showed that the preferred orientation of the Pt films varied somewhat across the samples.

Table XXIV: Comparison of d-spacings values with similar values for $PbTiO_3$, Pt and Pt_3Ti.

d-spacings / hkl		
$PbTiO_3$ 6-452	Pt 4-802	Pt_3Ti 17-64
0.2297 / 111	0.2265 / 111	0.2244 / 111
0.1950 / 200	0.19616 / 200	0.1946 / 200
0.13841 / 003 0.13787 / 220	0.13873 / 220	0.1379 / 220

Several weaker reflections which were not macedonite were also observed from each of the films (Table XXVI). Unlike many lead titanate type sol-gel films [Hsueh and MeCartney 1992, Myers and Chapin 1990], these reflections were again not attributable to pyrochlore (Table XXVII). MOCVD films do not appear to go through the same formation sequence as sol-gel or sputtered films, so pyrochlore is rarely observed. However, $PbTi_3O_7$ and TiO_2 have been noted for films prepared with NO_2 [Katayama et al. 1991]. EDS and EMPA indicated that the following elements could be present in the region analyzed by XRD: O, Si, Ti, Pb and Pt. Detailed EMPA showed C was not present (Appendix L). The most likely candidates for the minor phase/s are a titanium oxide and a lead or platinum based compound (Table XXVII). With so few reflections, it was not possible to make a definitive match by XRD. The different formation sequence associated with MOCVD permits lower temperatures to be employed for the deposition process and high post-deposition temperatures are not necessary either since the obstacle presented by pyrochlore-type phases does not exist.

Table XXV: Observed XRD intensities (I) and calculated texture coefficients (TC) of an as-deposited $PbTiO_3$ thin film on BNR Pt.

(hkl)	I_o (6-452)	I	TC
001	25	3	0.1
100	50	35	0.7
101	100	95	1.0
110	55	72	1.3
111	40	70	1.8
200	30	27	0.9
210	12	17	1.5
112	20	13	0.7
211	40	35	0.9
202	14	15	1.1

Too little attention to secondary phase formation has been paid by other researchers in general. For example, other film qualities, such as interfacial states and film defects are associated with the degradation of the switching properties and lower dielectric permittivities than with bulk ceramics [Yoo et al. 1993]. Analytical equipment limitations could account for the lack of reported results in this area since without glancing-angle capabilities for XRD, it can be difficult to obtain sufficient intensity from the layer of interest to identify these phases [Huang 1990].

TEM analyses indicated a very fine-grained lead oxide film was present on the surface of the $PbTiO_3$ film (figure 44). EMPA readings agreed with these results and suggested the layer was of the order of 1.5 nm in thickness (Appendix L). Due to this surface layer, it was difficult to obtain absolute values of the Pb to Ti ratios within the bulk of the $PbTiO_3$ layer. Naturally any excess Pb present on all perovskite films will oxidize if exposed to an O_2 rich atmosphere. At the end of each deposition run, the reactive gas flow was automatically stopped. Later the heater was manually turned off and the wafer and heated chuck cooled slowly (over the period of one or more hours) to ≤300°C before the wafer was removed from the system. It seems quite plausible that a layer of PbO_x will exist on all perovskite films (prepared by CVD) in accordance with the amount of excess Pb.

Table XXVI: Minor reflections present in the XRD spectra from the analysis of the $PbTiO_3$ layer. No match can be made to the pyrochlore compound: $Pb_2Ti_2O_6$.

d-spacing (nm)	nearest pyrochlore 26-142 reflection	Reflections observed in thin films					
		30359	30361	30363	30396	30405	30407
1.4298- 1.4300	1.4570				X		X
1.8122- 1.8174	1.8400	X	X	X		X	
2.2256- 2.2525	2.0060	X		X		X	
2.3331- 2.3367	2.3900	X				X	
2.9712- 2.9766	2.6100	X		X	X		X
2.9821- 2.9843	2.6100		X			X	
3.0760- 3.0830	3.0200					X	X

Figure 44: TEM plan-view image of the very fine-grained lead oxide surface coating on a $PbTiO_3$ sample. Inset shows a diffraction pattern from the same area.

The TEM micrographs from this film taken in plan-view (figure 45) show three different features, varying in size: dislocations, possibly associated with low angle sub-boundaries; overlapping crystals or thickness variations, and Moiré fringes. Similar micrographs can be found in the literature for $Pb(Sc_{0.5}Ta_{0.5})O_3$ thin films [Baba-Kishi et al. 1990]. No evidence of macro twin formation was found. This result was not unexpected because these films had small grains (due to the low deposition temperature) and a minimum grain size of the order of 0.3 μm is required for macro-twinning (§2.5).

Table XXVII: Possible matches of minor reflections.

d-spacing (nm)	compounds	JCPDS
1.4298- 1.4300	$PbPt_x$, PtTi	6-574, 23-1310
1.8122- 1.8174	$(Pb_{0.8}Ti_{0.2})Ti_3$	6-578
2.2256- 2.2525	Pt, Pt_3Ti, PtTi Ti_6O_{11}	4-802, 17-64, 23-1310 18-1401
2.3331- 2.3367	Ti_6O_{11}, Ti_5O_9, Ti_9O_{17}, $PbPt_x$	18-1401, 11-193, 18-1405, 6-574
2.9712- 2.9766	Ti_6O_{11}	18-1401
2.9821- 2.9843	$(Pb_{0.8}Ti_{0.2})Ti_3$	6-578
3.0760- 3.0830	Ti_5O_9, Ti_9O_{17}	11-193, 18-1405

Figure 45: Plan-view TEM micrograph shows three features: (a) dislocations, possibly with low-angle sub-boundaries, (b) overlapping crystals or thickness variations, and (c) Moiré fringes. Inset shows a <111> diffraction pattern.

Prior to the deposition of the $PbTiO_3$ film, the $Pt/Ti/SiO_2$ layers were distinct with relatively clean interfaces (figure 46). XRD analyses of the Pt films indicated that the BNR and NTEL films had a (111) and/or (220) preferred orientation while the MCNC films had a (220) preferred orientation. As well, the XRD reflections for the sputtered Pt film (NTEL) were shifted to the left in comparison to the evaporated Pt films (BNR and MCNC). It is believed that the observed shift in the reflections present for the unannealed NTEL Pt films are due to the high uniform stress of the film [Tu and Rosenberg 1988, Cullity 1978, Ho 1993]. (The diffractometer used in this study was not equipped to ascertain the degree of stress induced in the film, nor was a wafer stress gauge available). Studies using the appropriate instrumentation need to be carried out for further explanation of the reactions and stresses involved. Only then, can the impact of these Pt film differences on the electrical properties be properly assessed. There were no other significant differences between the Pt layers produced by different methods and/or companies.

During the CVD process, the annealing caused the Ti to react with the Pt and O and consequently, a new layer was formed between the original Pt and Ti layers (figure 47). X-ray diffraction analyses suggested that Pt_3Ti (cubic) may have formed. Further EDS analysis using the TEM indicated some interaction had also occurred between the Pb and Pt (figure 47).

4.3.4 Characterization of Etched and Annealed Films

To improve the top electrode contact (and eliminate the electrical testing

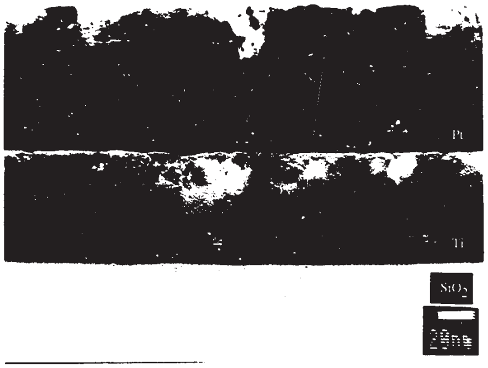

Figure 46: TEM micrograph shows a cross-section of unannealed $Pt/Ti/SiO_2$ layers.

Figure 47: TEM micrograph shows that after the CVD of $PbTiO_3$, new layers are formed in the $Pt/Ti/SiO_2$ layered structure.

difficulties believed to be associated with the lead oxide surface layer §4.3.5), nitric acid was examined as an etch to remove the PbO_x layer on the $PbTiO_3$. Films produced by other methods do suffer from this problem to a lesser degree and it is felt that the top electrode contact could be improved through mild etching [Griswold 1993]. There are two approaches one can adopt; either (i) develop a process that leads to Pb-poor films which can cause pyrochlore phases to form, or (ii) develop a process that gives Pb-rich films which require either high annealing temperatures for excess Pb elimination or acceptance of the degradation in performance due to secondary phases.

Initially, the etching behaviour of pure PbO films was studied. By measuring the change in film thickness by SEM XS, a dilute solution of nitric acid (1:5000 HNO_3:H_2O) was found to etch PbO at a rapid rate of ~8 μm.min^{-1}. A much stronger solution (1:9 HNO_3:H_2O) had no significant effect on $PbTiO_3$ films after a 30 s etch beyond removing most of the surface lead oxide. These films were examined by SEM in cross-section to check for thickness variation and the surfaces of the films were also examined to check for any marked changes in the morphology. Comparing SEM EDS spectra, it can be seen that the Pb content is slightly lower in the etched samples (figure 48). Although TEM studies showed a very thin layer of PbO_x was retained; it was quickly removed by further ion milling. An earlier etching study involving various acids found HNO_3 etched PZT at the slowest rate [Trolier at al. 1986]. It is significant that the etch rates varied so markedly between the compounds as it allows one a wide margin in etching times to remove unwanted surface layers.

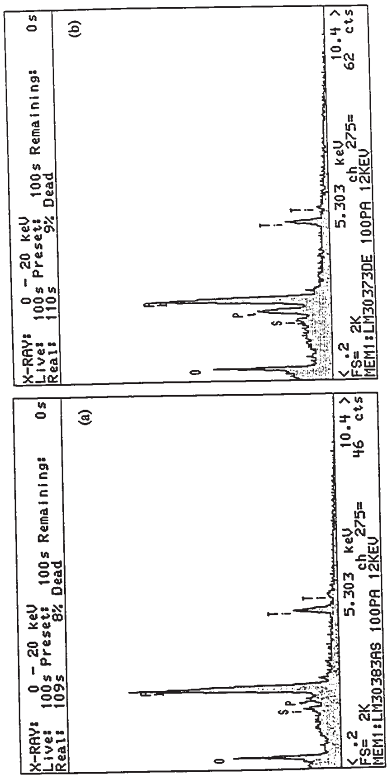

Figure 48: SEM EDS spectrum of an as-deposited film (a) contains more Pb than an etched film (b).

Annealing was done at four temperatures: 490, 515, 585 and 698°C in an O_2 ambient. These anneals were done to study the changes in the film quality, ferroelectric properties and multi-layered substrate. All of the extra reflections observed in the as-deposited samples disappeared upon heating the sample to 585°C (figure 49) suggesting that incomplete mixing or oxidation of the material was present when the films were deposited at the lower temperature (of <515°C). This finding suggests a lower limit on film deposition for MOCVD of $PbTiO_3$ if further annealing will not take place. For similar materials, such as PZT where the T_c value is lower by >100°C, this limit could be correspondingly lower. As well, the likelihood of significant $PbPt_x$ formation can be discounted as one would expect any interaction between the layers to increase with annealing.

Twinning, not evident in the as-deposited samples, was prevalent after annealing above 490°C (figure 50). Each twin was ~20 nm wide and 85-100 nm in length. The domain widths observed fit the general classification scheme developed for domain structures in §2.5. Usually these twins were found side-by-side in groups of 3 to 5, making the total width of the twinned structure (that is, the grain) to be about 95 nm. This twin formation follows the (textured) polycrystalline examples (cf. figure 13a). However, the more ordered (epitaxial) films discussed in §2.5 contained a more ordered array of twins. No obvious voids or secondary phases were observed by TEM in the films studied here, however the presence of some very fine-grained material was noted. It was estimated that this material corresponded to the amount of excess lead in the films (5% or more).

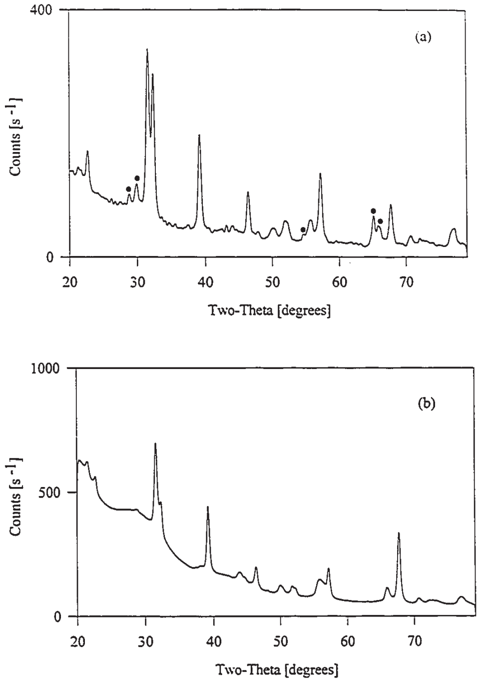

Figure 49: An XRD spectrum (a) from an unannealed $PbTiO_3$ film shows some secondary phases (marked ●), while (b) the spectrum of an annealed $PbTiO_3$ film on Pt shows reflections corresponding to the macedonite standard (6-452).

Figure 50: TEM micrograph taken in plan-view of an annealed $PbTiO_3$ film showing twins.

In a previous study on La-modified $PbTiO_3$ [Demczyk et al.1987], the experimentally observed minimum grain size (of 0.3 μm) where twinning was observed was compared to theoretical calculations. The minimum particle (grain) size for twinning is given by [Tanner and Ashby 1969]:

$$d^* = 2\,\gamma^T\,t_{min} / \epsilon \qquad (4.1)$$

where d^* is the diameter of the particle, γ^T is the twinning shear, t_{min} is the minimum twin thickness and ϵ is the strain given by

$$\epsilon = (c - a) / a \qquad (4.2)$$

where a and c are the lattice parameters of the compound of interest.

For the La-modified $PbTiO_3$ material, the minimum grain size was calculated to be of the order of 20 nm (actually 22 nm) based on geometrical considerations alone using the following values in eqns. 4.1 and 4.2: $c/a = 1.025$, $\gamma^T = 1$, and $t_{min} = 0.27984$ nm ($= d_{110}$: the interplanar spacing of the composition plane). However it was noted that the inclusion of interfacial or strain energy terms would increase this value [Demczyk et al. 1987]. To relate Demczyk's work to $PbTiO_3$, it is necessary to adjust the c/a ratio and d_{110} parameters. The smaller 0.2 μm grains found in this study do not contradict this calculation since the geometrical minimum size for $PbTiO_3$ is of the order of 10 nm. Of all the perovskite compounds, $PbTiO_3$ possesses the highest c/a ratio (1.0652). Since the value of minimum grain radius is inversely proportional to the c/a value, the grain size is considerably lower for pure $PbTiO_3$ than the La-modified compound. To compare these materials further is beyond the scope of this work as it involves bulk measurement values such as hardness.

A good correlation was obtained between an observed diffraction pattern from a twinned region and a simulated pattern (figure 51). For the simulation, a precipitate of macedonite the same size as a typical twinned region observed in the TEM, was used. This 20 nm wide (100), 85 nm tall (010) and 95 nm long (001) precipitate was rotated by 180° about the $[01\bar{1}]$ in a macedonite matrix. An angle 2ψ can be used to describe the angular difference between adjacent twinned regions. The relationship between this value and the lattice parameters [Demczyk et al. 1990] is as follows:

$$\tan(45° + \psi) = c / a \qquad (4.4)$$

Fairly good agreement between the theoretical and measured angular positions was found in this study. From the diffraction pattern, an angle of $\sim 6°$ was measured giving $\psi = 3$. For $PbTiO_3$ with a c/a value of 1.0652, a value of 1.8° is calculated using eqn. 4.4.

This twin formation plays an important role in stress reduction. Twin formation relieves strain generated by the cubic to tetragonal phase transformation. Also, studies of bulk $PbTiO_3$ [Matsuo and Sasaki 1966, Rice and Pohanka 1979] have shown that it is mechanically weak as a result of grain boundaries stresses from incompatible expansion of individual grains owing to the variation in the coefficients of thermal expansion in different crystallographic directions. This effect is minimized with small grains.

TEM cross-sectional analysis generally showed post-deposition annealing resulted in better adhesion of the $PbTiO_3$ film to the underlying Pt layer (figure 52). This improvement in adhesion was a major factor in producing better electrical results

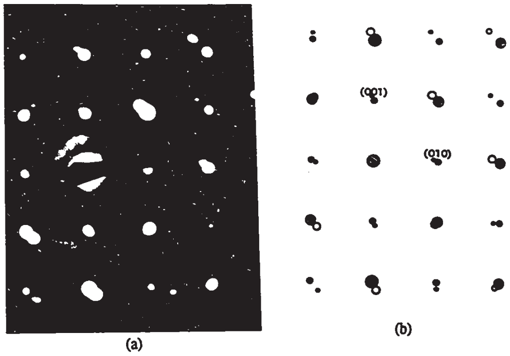

(a) (b)

Figure 51: Electron diffraction pattern (a) and simulated pattern (b) shows twin relationship.

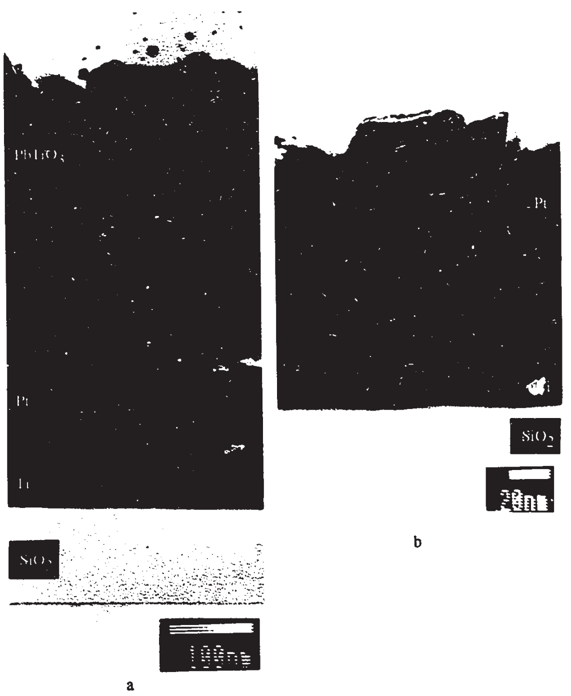

Figure 52: Micrographs of TEM cross-sections often exhibited poor adhesion for (a) unannealed $PbTiO_3$ samples and better adhesion (b) after annealing at 585°C. Although the TEM sample preparation process can magnify adhesion problems, this trend held across all the $PbTiO_3$ Pt-based samples.

since air gaps were removed. There was no significant differences between the results obtained from the three different Pt manufacturers, nor were there significant differences between the sputtered and evaporated Pt films. Even at the lowest RTA temperature used (490°C), TEM XS and EDS analysis revealed that further diffusion of the Ti into the Pt layer had occurred. Using GA-XRD, the Pt_3Ti cubic phase was identified as the most likely compound to have formed. SEM examination of the surface indicated no hillock formation had occurred and no Ti-O interaction was detected during TEM cross-sectional EDS except at the SiO_2 interface. In this study, limited diffusion of O through Pt was noted by either GA-XRD or cross-sectional TEM EDS.

In other studies where furnace annealing was performed (at 200-500°C), a Ti-Pt layer formed and was believed to act as a diffusion barrier and thereby limit further reactions [Tisone and Drobeck 1971]. They identified the layer formed at the interface as Ti_3Pt by electron diffraction and farther into the Pt and along the Pt grain boundaries, they found TiPt. In general, dislocations represent line defects along which accelerated diffusion (pipe diffusion) can take place [Tisone and Drobeck 1971]. Low angle grain boundaries are composed of arrays of dislocations and therefore also provide areas for rapid diffusion. In another study, diffusion of Ti into the Pt layer was evident after annealing at 500°C for 30 min. [Olowolafe et al. 1992]. From the XRD analysis, either Pt_3Ti (cubic phase assumed) or Pt was present. AES analysis showed Ti diffusion into the Pt had occurred, and also O diffusion through the Pt layer. XRD confirmed the presence of unspecified TiO_2 phases.

At the higher RTA temperatures used in this study (515-698°C) TEM cross-sectional examination showed that the Ti layer was completely consumed. It appears that once this occurs, further reactions do not occur even as the temperature is increased. Presumably if the choice of Pt:Ti film thicknesses selected gave a ratio less than one, then no unaffected Pt at the surface of the layers would remain. In another study, the inward diffusion of Pb (from a surface $PbTiO_3$ layer) and the interdiffusion of Pt and Ti was noted at 550°C [Greenwald et al. 1992]. Other researchers, also having a 2:1 ratio of Pt:Ti reported that a minimal layer of Pt remained on the surface even after furnace annealing at 800°C [Olowolafe et al. 1992]. These findings contrast to those of Sreenivas and his colleagues [1994] where the surface of the Pt was encapsulated by titanium oxide after an RTA at 700°C for 2 min. It is suggested that the porosity of their Pt layers and the elevated Pt sputtering temperatures (of 200-500°C) could account for these differences. Other studies have reported diffusion of $PbTiO_3$ type films through pinholes in the Pt or porous Pt [Kingon 1992]. Higher quality Pt films may alleviate or eliminate this problem. Also, hillock formation has been associated with ion beam sputter deposition of Pt followed by ion beam sputter-deposited $PbTiO_3$-type films [Al-Shareef et al. 1992]. Hillocking of the Pt was not an issue for any of the films examined in this work.

4.3.5 Comparison to Sol-Gel Films and Electrical Results

Generally, it is not possible to form the perovskite structure at temperatures as low as 515°C from a sol-gel process [Merklein et al. 1993, Grill et al. 1993,

Schwartz et al. 1993]. This is in part due to the necessity to "drive-off" excess material left from the precursor solutions and in part due to the formation sequence, commonly through a pyrochlore-type material. The former accounts for the porosity in sol-gel films, although development of more refined sol-gel methods are diminishing this problem [Lockwood et al. 1993]. The need for higher temperatures to prevent the pyrochlore phase limits the bottom electrode to materials which can withstand high temperature processing.

The sol-gel films in this study were created by an adaption to a standard PZT process (see §3.2) and consequently they contained trace amounts of Zr (3% according to EMPA). These films were pale green in colour with radial streaking from the spinning process. The colour observed comes from the refraction of light in the thin films, and therefore is not indicative of the material's inherent bulk colour. From SEM studies, the film was composed of regions of ~100 nm in diameter, squarish or round in appearance and closely packed together (figure 53). By cross-sectional SEM it was apparent that these features did not constitute islands, however electrical shorting at increased voltages suggested they represented weak points nonetheless. TEM PV indicated the film was fairly dense (figure 54). The two spun layers were distinct, but of two different thicknesses: 119 nm for the top layer and 88 nm for the layer below. Seven layers, as opposed to the expected five (2 sol-gel, 2 metal, and 1 oxide layer) were observed by TEM (figure 54) indicating considerable interaction between layers had occurred during the annealing steps associated with the sol-gel deposition process. XRD identified the sol-gel films as macedonite (figure 55)

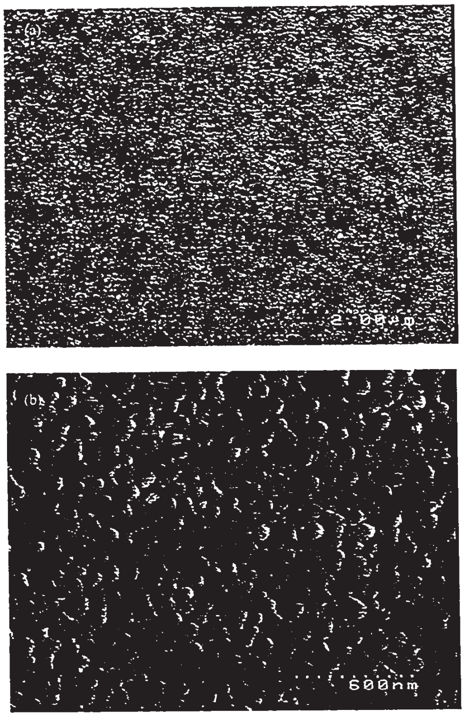

Figure 53: FE-SEM micrographs obtained using 10kV and taken at (a) 15,000 times and (b) 50,000 times are representative of the sol-gel $PbTiO_3$ film.

Figure 54: TEM micrograph taken in plan-view of a sol-gel $PbTiO_3$ sample (a). TEM cross-section shows layers below the $PbTiO_3$ (b).

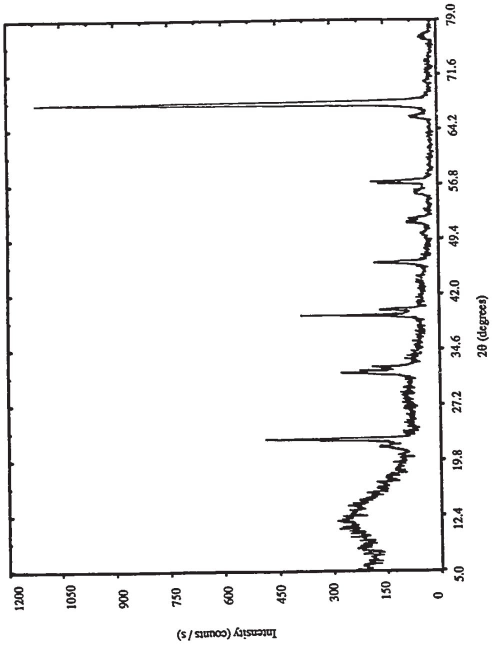

Figure 55: GA XRD pattern of sol-gel $PbTiO_3$ sample.

and the underlying layers as Pt_3Ti (cubic) or Pt, and Si.

The electrical characteristics of the CVD and sol-gel films were measured using the test arrangement described in §3.4. In total, six sets of electrical test measurements were made over a nine month period. The necessary test apparatus to do reliable basic testing (small signal and hysteresis) and advanced reliability testing was located in the Physics department of Queen's University. As noted earlier, the properties of $PbTiO_3$ films are inferior to PZT for memory applications.

These sol-gel samples had two different contact materials, Au and Al, and two sizes of electrodes, small and medium (§3.4) deposited onto them. The results from these films gave the following values at small applied voltages: ϵ' was inconsistent; usually quite low (9-18) at 1 kHz dropping to about half this value at high frequencies but at other times a value as high as 190 was measured; ρ was again quite variable, $\sim 3 \times 10^{11}$ Ω.cm at 1 kHz and dropping quickly with increasing frequency; and tan δ values were somewhat larger than usually reported: ranging from .06 at low frequencies to .03 at high frequencies. The large signal response evaluated at 1 kHz was primarily linear but there was a tendency for shorting of the electrodes to occur above 3 V. The PZT samples made by the Queens University's "standard" sol-gel process [Yi et al. 1988] and tested at the same time as these $PbTiO_3$ films, produced good hysteresis loops. This check ensured that the top electrode deposition process and electrical set-up were sound. However, it is not surprising that the $PbTiO_3$ material gave only a linear response as better results in comparison to PZT are not usually achieved from sol-gel processing.

The next two sets of tests involved CVD $PbTiO_3$ films, both as-deposited and after annealing in an N_2 atmosphere[*]. For these samples only small Au electrodes were used as the sol-gel study revealed no significant differences between 'small' and 'medium' sized electrodes and previous studies at Queen's University had shown these electrodes gave only slightly better results. A small dot size is favoured as less material is tested at one time and defective areas are more easily avoided. For highly defective material, a large dot size can result in 'global shorting' and hence eliminate the ability to make any measurements at all. The small signal results from these measurements were similar to those of the sol-gel films. It proved difficult to measure the hysteresis properties since the usual input voltages (2-6 V) produced no output signal, signifying an open circuit or the formation of extra unwanted barrier layers.

The TEM investigation of the surface of the $PbTiO_3$ films had revealed that the excess Pb had oxidized producing a thin very fine-grained layer (§4.3.4). The electrical results obtained were consistent with poor contacts. It is difficult to detect this surface layer by other analytical methods and indeed estimation of the layer thickness was difficult to make. After detailed EMPA studies involving changes of the accelerating voltage to probe different depths of the film, it was possible to give an approximate thickness estimation of 1.5 nm (§4.3.3). It was believed that these films were difficult to test electrically because the top surface layer of fine-grained

---

[*] These were the only films annealed in a N_2 rather than an O_2 ambient and this change was due to equipment limitations at that time.

lead oxide provided an inferior electrical contact and the lower interface had poor adhesion to the Pt (see §4.3.4) with the net result being a near open circuit. Reliable and consistent small signal electrical measurements were difficult to make and large signal properties were only possible at increased voltages (> 10 V). Pieces of each film were annealed to improve the $PbTiO_3$ film quality and the adhesion between the underlying areas. The electrical tests were repeated with similar results and again the problems were attributed to the poor top electrode contact.

The fourth set of electrical testing was performed on films which had this thin lead oxide layer removed. This was achieved by etching the films in a strong nitric acid solution for 30 s as described earlier (§4.3.4). Unlike the previous set of (unetched) samples, most areas tested produced a signal at reasonable voltages (.05 - 7 V). (A small percentage of untestable area is usual for material processed in class 1000^+ environments[*]).

At 1 kHz, the capacitance was measured to be 62 pF (Appendix M). Using the film thickness of 405 nm and eqn. 2.16 (§2.7.2), ϵ' was found to be 150 (Table XXVIII), well within the range of acceptable values for $PbTiO_3$ thin films and fairly close to the reported bulk ceramic value of 210 (Table XIX). The resistivity values expected for $PbTiO_3$ are of the order of 10^8 Ω.cm (bulk value), however, values ranging from $1x10^8$ Ω.cm [Greenwald et al. 1992, Dormans et al. 1992] to as high as

---

[*] Semiconductor processing areas (or clean rooms) are classified according to their particulate levels where a class 10 clean room is restricted to less than ten particles of 0.5 μm per ft^3, while a class 1000 has less than 1000 particles [Donovan 1990]. The room predominately used in this study would be classified as 10,000 or higher.

$1x10^{13}$ Ω.cm [Katayama et al. 1992] have also been reported for thin films. It is suggested that some of the unexpectedly high resistivity values reported in the literature may result from poor adhesion on the microscopic level between the $PbTiO_3$ and the underlying film/s (figure 52). As mentioned earlier, these films were predominantly deposited below the $PbTiO_3$ Curie temperature which may account for the observed linear dielectric properties. It is not generally known if improved electrical properties are obtained by the transition through the Curie temperature since most thin films and ceramics are formed above T_c. There are two reasons for this situation: (i) high temperatures are needed for making ferroelectric thin films if MOCVD is not used, and (ii) $PbTiO_3$ has the highest T_c, and therefore most compounds, PZT included, have a T_c below even MOCVD processing temperatures.

Table XXVIII: Electrical properties of an etched $PbTiO_3$ sample with no post-deposition anneal.

Frequency [kHz]	ϵ'	Resistivity [Ω.cm]	tan δ	Hysteresis properties
1	150	$3x10^{10}$	0.04	linear
10	143	$3x10^9$	0.03	linear
100	137	$5x10^8$	0.04	linear
1000	134	$3x10^8$	0.06	N.A.

The fifth set of tests was carried out on annealed samples. The values obtained for the 585°C annealed films (Appendix M) indicated a decrease in capacitance and resistance values from the unannealed sample. These changes from the unannealed case were mainly attributed to improved adhesion of the $PbTiO_3$ film

to the underlying Pt layer (figure 52). The tan δ values increased (Table XXIX), particularly at the low frequencies (1 kHz). However, hysteresis properties were now observed at these low switching frequencies (Table XXIX). These hysteresis properties were attributed to increased grain size, complete transformation of single oxides (for example PbO and Ti_6O_{11}) to $PbTiO_3$, complete transition through the Curie temperature or a combination of these factors. Generally these trends held true for samples annealed at both lower (515°C) and higher (698°C) temperatures with the exception of the measured resistance which was higher for some of the other annealing conditions. The trends observed were: (i) only a slight decrease in capacitance at higher frequencies, (ii) a decrease in resistance inversely proportional to frequency, and (iii) large tan δ values only at low frequencies.

The lack of improvement with annealing was confusing at first, but concurrent TEM studies indicated that the Au top electrodes were too thin to provide a continuous layer (figure 56). The evaporated Au was only ~2 nm in thickness and other studies have found that a thickness of 5 - 10 nm is required for a continuous coverage [Scott-Thomas 1994]. Indeed, results obtained with the electrical test probe directly on the surface of the $PbTiO_3$ film differed little from those where the probe was placed on a Au electrode. Since, the highly dense, consistent nature of the films indicated that large Al electrodes were a viable alternative, this approach was tried next.

The final set of electrical tests involved as-deposited and post-deposition annealed $PbTiO_3$ films with large Al top electrode 'dots'. A sub-set of the original

Figure 56: TEM plan view (a) where small dark circular regions are Au and cross-section (b) showing Au regions on the surface.

Table XXIX: Electrical properties of the 585°C annealed sample.

Frequency [kHz]	ϵ'	Resistivity [Ω.cm]	tan δ	Hysteresis properties
1	53	2x10^{10}	0.17	yes
10	41	6x10^{9}	0.06	no*
100	40	1x10^{9}	0.04	no*
1000	40	2x10^{8}	0.03	N.A.

*switching frequency is too high for the material; this effect has been observed by others.

matrix of annealing and etching conditions was studied. These films were tested over a range of voltages (0.05-15) at the usual testing frequencies (1 kHz - 1 MHz).

The measured capacitance values were fairly constant with a deviation of typically 1.3% over the frequency range of 1-1000 kHz. For most practical applications, a constant value over a wide range of frequencies is desired [Burfoot and Taylor 1979]. These results are much better than those from the sol-gel samples where the capacitance values dropped markedly by 13% from 1 kHz to 1 MHz. Usually a decrease in capacitance is not found until the frequency reaches 10^{8}- 10^{11} Hz [Burfoot and Taylor 1979]. ϵ' varied from 60-155, but it was difficult to make comparisons as some of the material tested was from outside the optimum region*. ϵ' is typically 1-10 for non-polar materials and significantly higher for most polar materials [Burfoot and Taylor 1979]. Other studies have found ϵ' to vary from 30-290 for CVD PbTiO$_3$ films (Table XIX).

---

* The optimum region in the centre with 30 mm diameter (described in §3.1.1) had been used for the SEM, EMPA, and TEM analyses and for the initial electrical testing.

The tan δ values were quite good, typically 0.01, except at 1 MHZ where increases up to 0.1 were noted (figure 57). This type of increase at the higher frequencies is often observed [Amm 1994]. The loss values for the sol-gel films were not as good, ranging from 0.03 to 0.06. High tan δ values have been linked to high leakage currents in device structures [Burfoot and Taylor 1979]. The CVD values obtained here compare favourably with those reported for other CVD films where values range from 0.020- 0.026 in the best cases [Katayama et al. 1991, Yoon et al. 1989] to higher values such as 0.040 - 0.19 in other instances [Shimizu et al. 1991, Katayama et al. 1992].

The measured resistance and hence the resistivity varied as expected with frequency (figure 57). The resistivity value at 1 kHz was similar to dc values reported for other CVD thin films (Table XIX) and to those values obtained for the sol-gel films; e.g., the resistivity ranged from 1.1 x 10^{11} to 1.7 x 10^{11} Ω.cm at 1 kHz.

At low frequencies and up to 10 kHz, hysteresis characteristics were observed (figure 58) for all the films examined, except the one annealed at 698°C which showed mainly linear properties. Apart from the 698°C sample, no appreciable difference was observed between the as-deposited and post-deposition annealed films. The hysteresis loops were not saturated indicating that problems with poorly contacting electrodes might still exist [Burfoot and Taylor 1979]. Problems at higher frequencies indicate the basic limitation on the speed at which the domains can be switched [Burfoot and Taylor 1979] and also, in this instance reflect the high loss

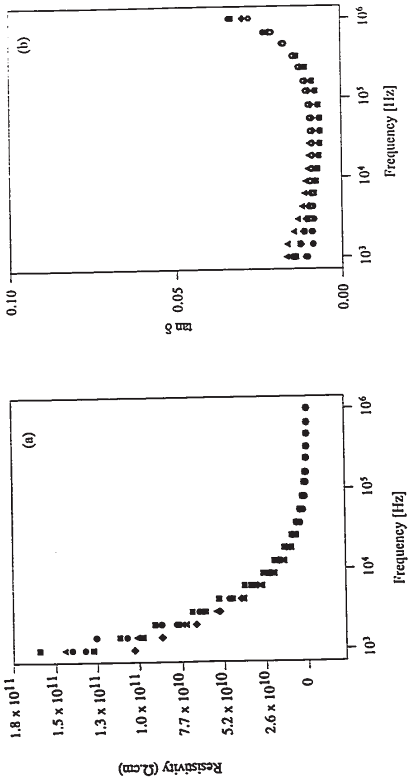

Figure 57: Resistivity as calculated from the parallel resistance and capacitance measurements is plotted against frequency (a). Values from two measurements over the frequency range for three different samples are shown. The minimum value shown on this graph corresponds to 5x10^{7} μΩ.cm at 1 MHz. Tan δ values are shown as a function of frequency (b).

Figure 58: Photograph of an oscilloscope trace of a hysteresis loop.

Table XXX: Hysteresis Measurements from CVD $PbTiO_3$ Films

Reference	ϵ_r	Frequency (Hz)	P_r ($\mu c/cm^2$)	E_a (kV/cm)	E_v (kV/cm)
Dormans et al. 1991	a	10,000	55	a	100
Okuyama et al. 1991	110-200	a	24	a	280
Yoon et al. 1989	130	60	14.1	340	20.16
this study	60-155	10,000	12 - 28	247	346
Kim et al. 1992	a	a	10	a	25
this study	60-155	10,000	5 - 10	247	123
this study	60-155	1,000	5 - 7	247	86
Okuyama et al.1985	10-200	60	0.5-27	670	~125-300
Kojima et al. 1983	100-130	a	0.16	72.3	14.5
Nakayama et al. 1982	100	a	0.16	a	14.5
Shimizu et al. 1991	30-290	a	a	a	a
Greenwald et al. 1991	a	10,000	a	a	a

[a] Value not provided

values at increased frequencies. The hysteresis properties observed for these films are compared to other values reported in the literature for $PbTiO_3$ CVD films (Table XXX). (The listing in Table XXX is made according to the remanent polarization values.) The highest P_r value reported by Dormans and his colleagues of 55 $\mu C.cm^{-2}$ was a surprise to them and was not well understood [Dormans et al. 1992]. The best value measured in this study was only 20% of this value. Generally low coercive fields and high frequencies are desirable for memory applications, along with high remanent polarization. Superior properties can be achieved with PZT material [Dormans et al. 1992]. It was observed that breakdown usually occurred at less than 250 $kV.cm^{-1}$ in this study. Other researchers have noted breakdown below 500 $kV.cm^{-1}$ [Katayama et al. 1991] or 200 $kV.cm^{-1}$ [Dormans et al. 1991] and have stated that the poor breakdown strength of the films remains a problem to be solved [Katayama et al. 1991, Dormans et al. 1991].

5.0 CONCLUSIONS

1. The MOCVD process developed for TiO_2 produced films of anatase, regardless of the deposition temperature used over the range of 300-600°C, §4.1. After annealing at temperatures up to 1060°C, anatase remained as the dominant phase. The pyrolytic decomposition mechanism for TiO_2 deposition, $Ti(OC_3H_7)_4 \rightarrow TiO_2 + 2H_2O + 4C_3H_6$ proposed by Okada and his colleagues [1988] was supported (§4.1.2). With the cold-wall system used in this study, the deposition process had an apparent activation energy of 71 $kJ.mol^{-1}$ (§4.1.3). Raman spectroscopy and XRD were compared as techniques for structure determination of titanium oxides. Anatase is extremely Raman active and was detectable using Raman spectroscopy when XRD indicated only an amorphous material.

2. The MOCVD process for lead oxide deposition produced various compounds: litharge, massicot, scrutinyite, and pure lead as identified by Raman spectroscopy, XRD and electron diffraction (§4.2). The reaction was found to be oxidation controlled with an apparent activation energy of 97 $kJ.mol^{-1}$.

3. A low temperature (515°C maximum), low pressure (1.1 mTorr) MOCVD process was developed for the growth of $PbTiO_3$ thin films (§4.3.1). There are no previous studies of $PbTiO_3$ MOCVD processes using pressures of less than 2 mTorr, and few results from low temperatures (without plasma or photo enhancements) have been reported.

4. At low deposition temperatures (<515°C), the formation of the perovskite phase was incomplete and oxides of TiO_x and PbO_x were present (§4.3). It appears that the formation sequence associated with MOCVD films does not involve pyrochlore-type phases, unlike sol-gel films where they have been reported.

5. Silicon contamination was shown to interfere with the phase transition from the high temperature cubic phase to the room temperature tetragonal, ferroelectric phase [Madsen and Weaver 1993].

6. The morphology of the $PbTiO_3$ films was similar to those reported in the literature (§4.3.3). The polycrystalline nature and preferred orientation of the underlying layer (Pt) was retained (§4.3.3). TEM examination of the films indicated no formation of macro-domains had occurred at the deposition temperature. The lattice parameters of the tetragonal $PbTiO_3$ films determined from XRD measurements were a = 0.3901 nm and c = 0.41521 nm (Appendix K).

7. The first report of PbO_x formation on Pb-rich films was made (§4.3.3). Using nitric acid as the basis for an etch solution, this surface PbO_x layer was rapidly removed, while the $PbTiO_3$ film was not significantly affected (§4.3.4). This etching procedure was shown to improve the electrical characteristics (§4.3.5).

8. After post-deposition annealing at 585°C, twinning was readily observed. The size of the twins was found to fit the classification scheme developed (§2.5). The overall size of the grains was found to be quite small, on the order of 0.1-0.2 μm. and they were found to agree with simple theoretical calculations based on the lattice parameters of $PbTiO_3$ (§4.3.4).

9. The underlying layers of Pt and Ti reacted with each other even at the deposition temperatures! Apart from the internal stresses of the Pt films, little differences was noted between films from different suppliers. At 698°C, the Ti layer was completely consumed by a reaction with O and Pt. No hillock formation or surface TiO_x was found.

10. The sol-gel films examined as comparison samples in this study were processed at 650°C. Interaction between the various layers had occurred resulting in a sample with seven instead of the expected 4 or 5 layers (§4.3.5).

11. In terms of the small signal electrical characteristics, the CVD films were more consistent than their sol-gel counterparts (§4.3.5). The top electrode adhesion and thickness was found to be important for making reliable electrical measurements. The capacitance values deviated less than 1.3% over the frequency range of 1kHz to 1 MHz. ε' was found to fall within the range reported for $PbTiO_3$ CVD thin films. The resistivity of the films were very good, $\sim 10^{11}$ Ω-cm at 1 kHz. The tan δ values were best at intermediate frequencies (5-100 kHz). The higher loss values found at high frequencies were attributed to the difficulties of switching the domains so quickly.

12. Slight hysteresis characteristics were observed for all the films examined apart from the one annealed at 698°C. No other appreciable differences were noted between the as-deposited and post-deposition annealed films. The best value for P_r measured was only $\sim 28\ \mu C.cm^{-2}$ and breakdown often occurred at less than 250 $kV.cm^{-1}$.

6.0 BIBLIOGRAPHY

M.F. Abadir, A.M. Gadalla and Y.M. El-Agamawi, Trans. & J. Brit. Cer. Soc. 75, 68 (1976).

N. Abt, "Electrical Measurement of Ferroelectric Capacitors of Ferroelectric Capacitors for Non-Volatile Memory Applications" Mater. Res. Soc. Symp. Proc. **200**, 303-312 (1990).

D.M. Adams and D.C. Stevens, "Single-crystal Vibrational Spectra of Tetragonal and Orthorhombic Lead Monoxide" J. Chem. Soc., 1096 (1977).

F. W. Ainger, C. J. Brierley, M.D. Hudson, C. Trundle and R.W. Whatmore, "Ferroelectric Thin Films by Metal Organic Chemical Vapour Deposition" Mater. Res. Soc. Symp. Proc. **200**, 37-47 (1990).

K.A. Aitchison, J.D. Barrie, and J. Ciofalo, "Deposition of Ceramic Films by a Novel Pulsed-Gas MOCVD Technique, Mater. Res. Proc., Spr. Mtg. (1992).

H. Al-Shareef, K.D. Gifford, P.D. Hren, S.H. Rou, O. Auciello and A.I. Kingon, "Bottom Electrodes for Ferroelectric Thin Films", Intl. Symp. on Integr. Ferroelectrics, 181-196 (1992).

M.S. Ameen, T.M. Graettinger, S.H. Rou, H.N. Al-Shareef, K.D. Gifford, O. Auciello, and A.I. Kingon, "Processing and Structural Characterization of Ferroelectric Thin Films by Ion Beam Sputtering", Mater. Res. Soc. Proc. **200**, 65-76 (1990).

American Institute of Physics Handbook, 3rd Ed., McGraw-Hill (1972).

D. Amm, private communication (1994).

ASM Engineering Materials Reference, ASM Intl., Ohio, pp 216-217 (1989).

K. Aykan, "A Novel Lead Titanate, $PbTi_3O_7$", J. Am. Ceram. Soc. **51**(10), 577-582 (1968).

K.Z. Baba-Kishi, I.M. Reaney and D.J. Barber, "Transmission electron microscopy of second-phase particles in $Pb(Sc_{½}Ta_{½})O_3$ Ferroelectric Ceramics", J. Mats. Sci. **25**, 1645-1655 (1990).

C.S. Barrett and J.B. Massalski, Structure of Metals, Pergamon, Oxford (1980).

D.B. Bondurant, "Fabrication and Characterization of Ferroelectric PLZT 7/65/35 Ceramic Thin Films and Fibers" Ferroelectrics 112(B), 273-282 (1990).

D. Bondurant and F. Gnadinger, "Ferroelectrics for Nonvolatile RAMs", IEEE Spectrum, 30-33 (July 1989).

G.E.P. Box, W.G. Hunter and J.S. Hunter, Statistics for Experimenters, Wiley, Toronto (1978).

C. J. Brierley, L. Considine, R. Sethi and R. Whatmore, "An Investigation into the Growth of Lead Titanate by MOCVD using a Pyrolytic and Sputter Assisted Plasma Process" MRS 1986 Fall Mtg. **79**, 779-786 (1987).

C.J. Brierley, C. Trundle, L. Considine, R.W. Whatmore and R.F. Ainger, "The Growth of Ferroelectric Oxides by MOCVD", Ferroelectrics **91**, 181-192 (1989).

J.C. Burfoot and G.W. Taylor, Polar Dielectrics and Their Applications, University of California, Berkeley & Los Angeles (1979).

V.M. Burlakov and M.R. Yakheev, "Raman Scattering in Ferroelectric $TlGaSe_2$" Phys. Stat Sol. (b) **151**, 337-346 (1989).

G. Burns and B.A. Scott, "Raman Studies of Underdamped Soft Modes in $PbTiO_3$", Phys. Rev. Lett. 25(3), 167-170 (1970).

I.D. Calder, J. Ellul, I. Emesh and L.D. Madsen, NTEL internal report (1993).

R.N. Castellano, "Ion Beam Deposition of Ferroelectric Thin Films Sputtered from Multicomponent Targets". J. Vac. Sci. Technol. 17(2), 629-633 (1980).

C.D. Chandler, M.J. Hampden-Smith and R.W. Schwartz, "Ferroelectric Thin Films via Sol-Gel Processing of Single-Source Precursors", Mater. Res. Soc. Symp. Proc. **310**, 357-362 (1993).

P.-H. Chang, M.D. Coviello and A.F. Scott, "Cross-Sectional TEM Sample Preparation for Multilayer Electronic Materials", Mater. Res. Soc. Symp. Proc. **115**, 93-97 (1988).

S. Chen, C.S. Wei and R.K. Shukla, "The Use of TiN Produced by Rapid Thermal Annealing in the First Level Metallization for VLSI Devices", V-MIC Conf. (June 1987).

X. Chen, H. Yamane and K. Kaya, "Synthesis and Properties of Highly C-Axis Oriented $PbTiO_3$ Thin Films Prepared by an MOCVD Method", J. Phys. III France, 2(8) 1439-1444 (1992).

C.K. Chiang, L.P. Cook, P.K. Schenek, P.S. Brody and J.M. Benedetto, "Lead Zirconate-Titanate Thin Films Prepared by the Laser Ablation Technique", Mater. Res. Soc. Symp. Proc. **200**, 133-140 (1990).

F.A. Cotton, G. Wilkinson and P. Gaus, Advanced Inorganic Chemistry, 4th Ed., Wiley & Sons, Toronto, p. 695 (1980).

F.A. Cotton, G. Wilkinson and P. Gaus, Basic Inorganic Chemistry, 2nd Ed., Wiley & Sons, Toronto, pp. 60 & 338 (1987).

A.H. Cottrell, An Introduction to Metallurgy, Edward Arnold, London, U.K., pp. 143-145 (1968).

CRC Handbook of Chemistry and Physics, 74th Ed., edited by D.R. Lide, CRC, Ann Arbor, Michigan, USA (1993).

A. Croteau, S. Matsubara, Y. Miyasaka, and N. Shohata, "Ferroelectric $Pb(Zr,Ti)O_3$ Thin Films Prepared by Metal Target Sputtering", Proc. 6th Mtg. Ferroelec. Mater. & Appl., Kyoto (1987); Jpn. J. Appl. Phys. **26**, 18-21 (1987).

A. Croteau and M. Sayer, "Growth and Characterization of $Pb(Zr, Ti)O_3$ Films Deposited by Reactive Sputtering of Metallic Targets", Proc. 6th IEEE Integr. Symp. on Applic. of Ferroelec., 606-609 (1986).

B.D. Cullity, Elements of X-Ray Diffraction 2nd Ed., pp. 13 & 135, Addison-Wesley, Don Mills, Ontario Canada (1978).

W.A. Deer, R.A. Howie and J. Zussmann, Rock Forming Minerals, vol. 5, pp. 48-55, Wiley, New York (1962).

B.G. Demczyk, A.G. Khachturyan and G. Thomas, "On a Minimum Grain Size for Domain Formation in Lanthanum-Modified Lead Titanate Ferroelectric Ceramics" Scripta Metalurgica **21**(7), 967-969 (1987).

B.G. Demczyk, R.S. Rai and G. Thomas, "Ferroelectric Domain Structure of Lanthanum-Modified Lead Titanate Ceramics" J. Am. Ceram. Soc. **73**(3), 615-620 (1990).

A. de Wilton, NTEL internal report (1988).

G.J.M. Dormans, M. de Keijser & P.J. van Veldhoven, "$PbTiO_3$ Thin Films Grown by Organometallic Chemical Vapour Deposition" Intl. Symp. Integr. Ferroelectrics, 598-611 (1991).

G.J.M. Dormans, M. de Keijser and P.J. van Veldhoven, "Ferroelectric $PbZr_xTi_{1-x}O_3$ Thin Films Grown by Organometallic Chemical Vapor Deposition" Mater. Res. Soc. Conf. Proc. **243**, 203-212 (1992a).

G.J.M. Dormans, P.J. van Veldhoven and M. de Keijser, "Composition-controlled Growth of $PbTiO_3$ on $SrTiO_3$ by Organometallic Chemical Vapour Deposition" J. Crystal Growth **123**, 537-544 (1992b).

A. Erbil, W. Braun, B.S. Kwak, B.J. Wilkens, L.A. Boatner and J.D. Budai, "Oxide Ferroelectric Materials Grown by Metalorganic Chemical Vapour Deposition", J. Crystal. Growth **124**, 684-689 (1992).

I. Emesh, private communication (1993).

I. Emesh, I. Calder, V. Ho, G. Jolly and L.D. Madsen, "Method for Fabricating a High Density Capacitor for Memory Applications", US patent no. 5330931 (July 19, 1994); Canadian filing to follow.

E.T. Fitzgibbons, K.J. Sladek, and W.H. Hartwig, "TiO_2 Film Properties as a Function of Processing Temperature", J. Electrochem. Soc. 119(6), 735-739 (1972).

H. Funakubo, K. Imashita, N. Kieda and N. Mizutani, "Formation of Epitaxial $Pb(Zr,Ti)O_3$ Film by CVD", Nippon Seramikkusu Kyokai Gakujutsu Ronbunshi **99**(3), 248-250 (1991).

Y. Gao, G. Bai, K.L. Merkle, Y. Shi, H.L.M. Chang, Z. Shen and D.J. Lam, "Microstructure of $PbTiO_3$ Thin Films Deposited on (001)MgO by MOCVD" J. Mater. Res. **8**(1), 145-153 (1993).

D.J. Gardiner and P.R. Graves, ed., Practical Raman Spectroscopy, Springer-Verlag, New York, NY (1989).

R.P. Goehner and M.O. Eatough, "A Study of Grazing Incidence Configurations and Their Effect on X-Ray Diffraction Data", Powder Diffraction 7(1), 2-5 (1992).

P.J. Goodhew and F.J. Humphries, Electron Microscopy and Analysis, 2nd Ed., Taylor and Francis, New York (1988).

J.P. Goral, M.M. Al-Jassim, and M. Huffman, "TEM Investigation of the Ferroelectric Domain Structure in Sputtered PZT Thin Films" Mater. Res. Soc. Symp. Proc. **200**, 225-230 (1990).

A.C. Greenwald, J.T. Daly and N.M. Kalkhoran, "Chemical Vapour Deposition of

Lead-Titanate", Mater. Res. Soc. Symp. Proc. 243, 229-234 (1992).

A. Grill, D. Beach, C. Smart and W. Kane, "Bottom Electrodes for High Dielectric Oxide Compounds: Effects on Crystallization of Lead Containing Ferroelectrics" Mater. Res. Soc. Symp. Proc. **310**, 189-194 (1993).

E. Griswold, private communication (1993).

G.H. Haertling, presentation Intl. Symp. Integr. Ferroelec., Colorado Springs, CO (1989).

L.L. Hench and J.K. West, Principles of Electronic Ceramics, Wiley, Toronto, ch. 6 (1990).

P.B. Hirsch, A. Howie, R.B. Nicholson, D.W. Pashley and M.J. Whelan, Electron Microscopy of Thin Crystals, Butterworth, Toronto, Ont. (1965).

M.L. Hitchman and K.F. Jensen, in Chemical Vapour Deposition: Principles and Applications, ed. by M.L. Hitchman and K.F. Jensen, Academic, Toronto, ch.1 & 4, (1993).

V. Ho, private communication (1993).

C.-C. Hseuh and M.L. McCartney, "TEM Analyses of Sol-Gel Derived and Sputtered PZT Thin Films" Mater. Res. Soc. Symp. Proc. **200**, 219-224 (1990).

T.C. Huang, "Surface and Ultra-Thin Film Characterization by Grazing-Incidence Asymmetric Bragg Diffraction", Adv. in X-Ray Anal. 33, 91-100 (1990).

M. Huffman, private communication (1993, 1991).

S. Ingrey, M.B. Johnson, R.W. Streater and G.I. Sproule, "Artifacts Observed during auger profiling of Ta, Ti, and W Metals, Nitrides and Oxynitrides", J. Vac. Sci. Technol. **20**(4), 968-970 (1982).

H. Itoh, K. Kashihara, T. Okudaira, K. Tsukamoto and Y. Akasaka, IEDM 91, 831-834 (1991).

B. Jaffe, W.R. Cook and H. Jaffe, Piezoelectric Ceramics, Academic, London and New York (1971).

JCPDS-Joint Committee on Powder Diffraction Standards, International Centre for Diffraction Data, 1601 Park Lane, Swarthmore PA, USA 19081-2389 (1992).

K.F. Jensen, in Chemical Vapour Deposition: Principles and Applications, ed. by

M.L. Hitchman and K.F. Jensen, Academic, Toronto, ch.2 (1993).

D.J. Johnson, "Electrical Characterization and Fatigue of Ferroelectric Thin Films", Master's Thesis, Queen's University, Kingston Ont. (1990).

F. Jona and G. Shirane, Ferroelectric Crystals, Pergamon, Oxford (1962).

B.A. Joyce, "The Growth and Structure of Semiconducting Thin Films" Rep. Prog. Phys. **137**, 363-420 (1974).

T.S. Kalkur, G. Argos, L. Kammerdiner, "Characteristics of Metal/PZT/p-Si Capacitors", Mater. Res. Soc. Symp. Proc. **200**, 313-318 (1990).

A.E. Kaloyeros and M.A. Fury, "Chemical Vapour Deposition of Copper for Multilevel Metallization", Mater. Res. Soc. Bull. **XVIII**(6), 22-29 (1993).

T. Katayama, M. Fujimoto, M. Shimizu and T. Shiosaki, "Growth and Properties of $PbTiO_3$ Thin Films by Photoenhanced Chemical Vapour Deposition", Jpn. J. Appl. Phys. **30**(9B), 2189-2192 (1991).

T. Katayama, M. Shimizu and T. Shiosaki, "Photoenhanced Chemical Vapour Deposition of $PbTiO_3$ and $Pb(Zr,Ti)O_3$ Thin Films", Intl. Symp. Integr. Ferroelectrics, 382-391 (1992).

A. Kavanaugh and J.O. Williams, "The Preparation and Characterization of (Pb,La)(Zr,Ti) Thin Films" Brit. Ceram. Proc. No.41, 59-66 (1989).

M. de Keijser, G.J.M. Dormans, J.F.M. Cillessen, D.M. de Leeuw, and H.W. Zandbergen, "Epitaxial $PbTiO_3$ Thin Films Grown by Organometallic Chemical Vapor Deposition", Appl. Phys. Lett. **58**(23), 2636-2638 (1991).

M. de Keijser, P.J. van Veldhoven and G.J.M. Dormans, "Organometallic Chemical Vapor Deposition of Lead Zirconate-Titanate Thin Films", Mater. Res. Soc. Conf. Proc. **310**, 223-234 (1993).

W. Kern and V.S. Ban in Thin Film Processes, ed. J.L. Vossen and W. Kern, Academic, Toronto, pp. 257-331 (1978).

H. Kezuka, R. Egerton, M. Masui, T. Wada, T. Ikehata, H. Mase and M. Takeuchi, "Electrical Resistivity of RuO_x Thin Films prepared by Ion Beam Sputter Deposition", Appl. Surf. Sci. **65/66**, 293-297 (1993).

Y.B. Kim and S.G. Yoon, "Ferroelectric Properties of Lead Titanate Films deposited by Low Pressure Chemical Vapor Deposition", J. Electrochem. Soc. **139**(9), 2559-2562 (1992).

A.I. Kingon, presentation at Intl. Symp. on Integr. Ferroelectrics, CA USA (1992).

A.I. Kingon, K.Y. Hsieh, L.L.H. King, S.H. Rou, K.J. Bachmann and R.F. Davis, "$PbTiO_3$ Thin Films by Chemical Beam Deposition", Mater. Res. Soc. Symp. Proc. **200**, 49-56 (1990).

B.S. Kwak, E.P. Boyd and A. Erbil, "Metalorganic Chemical Vapour Deposition of $PbTiO_3$ Thin Films" Appl. Phys. Lett. **53**(18), 1702-1704 (1988).

P.V. Lambeck and G.H. Jonker, "The Nature of Domain Stabilization in Ferroelectric Perovskites" J. Phys. Chem. Solids **47**(5), 453-461 (1986).

R.A. Levy and M.L. Green, "Low Pressure Chemical Vapour Deposition of Tungsten and Aluminum for VLSI Applications", J. Electrochem. Soc. **134**, 37c-49c (1987).

M.E. Lines and A.M. Glass, Principles and Applications of Ferroelectrics and Related Materials, Clarendon, Oxford (1977).

S.J. Lockwood, R.W. Schwartz, B.A. Tuttle and E.V. Thomas, "Solution Chemistry Optimization of Sol-Gel Processed PZT Thin Films", Mater. Res. Soc. Symp. Proc. **310**, 275-280 (1993).

P.G. Lucuta, "Ferroelectric-Domain Structure in Piezoelectric Ceramics" J.Am. Ceram. Soc. **72**(6), 933-937 (1989).

L.D. Madsen and L. Weaver, "Examination of Titanium Oxides, Lead Oxides and Lead Titanates using X-Ray Diffraction and Raman Spectroscopy", Mater. Res. Soc. Symp. Proc. **310**, 385-390 (1993).

L.D. Madsen and L. Weaver, "Examination of Barrier Layers for Lead Zirconate Titanate Thin Films", J. Electronic Mater. **21**(1), 93-97 (1992).

L.D. Madsen and L. Weaver, "Examination of Barrier Layers for Lead Zirconate Titanate Thin Films", presented at the Electronics Mater. Conf., Boulder, CO, USA (1991).

L.D. Madsen and L. Weaver, "Properties of *In Situ* Doped Polycrystalline Silicon Thin Films deposited from Phosphine and Disilane" Mater. Res. Soc. Symp. Proc. **182**, 43-48 (1990).

G. Majni, F. Panini, and G. Sodo, "Lateral growth of Pt and Pd Silicides on an SiO_2 Layer", Thin Solid Films **125**, 313-320 (1985).

F.W. Martin, "A Metastable Cubic Form of Lead Titanate observed in Titania Nucleated glass Ceramics", Phys. and Chem. of Glasses **6**(4), 143-146 (1965).

J.M. Martinez-Duart and J.M. Albella, "Micrometalization Technologies" in Reduced Thermal Processing for ULSI, pp.269-294, Plenum, New York (1989).

H.T. Martirena and J.C. Burfoot, "Grain-size Effects on Properties of Some Ferroelectric Ceramics", J. Phys. C:Solid State Phys. **7**, 3182-3192 (1974).

Y. Matsuo and H. Sasaki, "Effect of Grain Size on Microcracking in Lead Titanate Ceramics", J. Am. Ceram. Soc. **49**(4), 229-230 (1966).

L.D. McMillan, "Ferroelectric Materials: Processing and Testing", Symp. on Integr. Ferroelec., Colorado Springs (1989).

L.D. McMillan, C.A. Paz de Araujo, T. Roberts, J. Cuchiaro, M. Scott, "Liquid Source CVD", presented Intl. Symp. Ferroelectrics, Colorado (1991).

H.D. Megaw, "Origin of Ferroelectricity in Barium Titanate and Other Perovskite-Type Compounds" Acta Cryst. **5**, 739-749 (1952).

H.D. Megaw, "Crystal Structure of Double Oxides of the Perovskite Type" Proc. Phys. Soc. **58**(2), 133-152 (1946).

S. Merklein, D. Sporn and A. Schönecker, "Crystallization Behaviour and Electrical Properties of Wet-Chemically Deposited Lead Zirconate Titanate Thin Films" Mater. Res. Soc. Symp. Proc. **310**, 263-268 (1993).

C. Michel, "Observations of Domains in Ferroelectrics and Ferromagnetics with a Scanning Electron Microscope" Phillips Tech. Rev. **36**(1), 18-25 (1976).

T. Mitsuhashi and O.J. Kleppa, "Transformation Enthalpies of the TiO$_2$ Polymorphs" J. Am. Ceram. Soc., **62**(7-8), 356-357 (1979).

R.L. Moon and Y.-M. Huong, in Chemical Vapour Deposition: Principles and Applications, ed. by M.L. Hitchman and K.F. Jensen, Academic, Toronto, ch.6, (1993).

S.P. Murarka, "Refractory Silicides for Integrated Circuits", J. Vac. Sci. Technol. **17**(4), 775 (1980).

E. Myers, private communication (1993).

S.A. Myers and L.N. Chapin, "Microstructural Characterization of Ferroelectric Thin Films for Non-Volatile Memory Applications", Mater. Res. Soc. Symp. Proc. **200**, 231-236 (1990).

T. Nakagawa, J. Yamaguchi, M. Okuyama and Y. Hamakawa, "Preparation of PbTiO$_3$ Ferroelectric Thin Film by Chemical Vapor Deposition", Jpn. J. Appl. Phys. **21**(10), L655-L656 (1982).

M.A. Nicolet, "Diffusion Barrier in Thin Films", Thin Solid Films **52**, 415-443 (1978).

M.A. Nicolet and M. Bartur, "Diffusion Barriers in Layered Contact Structures", J. Vac. Sci. & Technol. **19**(3), 786-789 (1981).

H. Norström, K. Maex, J. Vanhellemont, G. Brijs, W. Vandervorst and U. Smith, "Simultaneous Formation of Contacts and Diffusion Barriers for VLSI by Rapid Thermal Silicidation of TiW", Appl. Phys. A **51**, 459-466 (1990).

M. Okada and K. Tominaga, "Preparation and Properties of (Pb,La)(Zr,Ti)O$_3$ Thin Films by Metalorganic Chemical Vapour Deposition" J. Appl. Phys. **71**(4), 1955-1959 (1992).

M. Okada, K. Tominaga, T. Araki, S. Katayama and Y. Sakashita, "Metalorganic Chemical Vapour Deposition of c-Axis Oriented PZT Thin Films", Jpn. J. Appl. Phys. **29**, 718-722 (1990).

M. Okada, S.Takai, M. Amemiya and K. Tominaga, "Preparation of c-Axis Oriented PbTiO$_3$ Thin Films by MOCVD under Reduced Pressure", Jpn. J. Appl. Phys. **28**, 1030-1034 (1989).

M. Okada, H. Watanabe, M. Murarka, A. Nishiwaki and K. Tomita, "Preparation of PbTiO$_3$ Thin Films by MOCVD under Atmospheric Pressure", J. Ceramic. Soc. Jpn. Intl. Ed. **96**, 676-682 (1988).

M. Okuyama and Y. Hamakawa, "Preparation and Basic Properties of PbTiO$_3$ Ferroelectric Thin Films and their Device Applications", Ferroelectrics **63**, 243-252 (1985).

M. Oikawa and K. Toda, "Preparation of Pb(Zr,Ti)O$_3$ Thin Films by Electron Beam Evaporation Technique", Appl. Phys. Lett. **29**(8), 491-492 (1976).

J.O. Olowolafe, R.E. Jones, A.C. Campbell, P.D. Maniar, R.I. Hegde and C.J. Mogab, "Analyses of Pt/Ti Electrodes for PLZT Capacitors", Mater. Res. Soc. Symp. Proc. **243**, 355-360 (1992).

B. Oliver, NTEL internal report (1989).

R.H. Packwood, private communication (1994).

R.H. Packwood and G. Remond, "The Interpretation of X-Ray and Electron Signals generated in Thin or Layered Targets", Scanning Microscopy **6**(2), 367-384 (1992).

L.H. Parker and A.F. Tasch, "Ferroelectric Materials for 64Mb and 256Mb DRAMs", IEEE Cts. and Dev. Mag., 17-26 (Jan. 1990).

N.R. Parikh, J.T. Stephen, M.L. Swanson, and E.R.Myers, "Study of Diffusion Barriers for PZT Deposited on Si for Non-Volatile Random-Access Memory Technology", Mater. Res. Soc. Proc. **200**, 193-198 (1990).

Y. Pauleau, "Interconnect Materials for VLSI Circuits", Solid State Technol., 155-162 (Apr. 1987).

Y. Pauleau, "Chemical Vapour Deposition of Tungsten Films for Metallization of Integrated Circuits", Thin Solid Films **122**, 243-258 (1984).

D.A. Payne, K.D. Budd, R.W. Swartz and S. Dey, "Sol-Gel Processing of Thin-Layer Ferroelectrics" Symp. on Integr. Ferroelec., Colorado Springs (1989).

C.H. Peng and S.B. Desu, "$Pb(Zr^xTi_{1-x})O_3$ Thin Films by Hot-Wall MOCVD", Intl. Symp. Integr. Ferroelec. 460-472 (1992).

W.T. Petuskey, D.A. Richardson and S.K. Dey, "Chemical Aspects of Pb-Zr-Ti Oxide Thin Film Syntheses by PE-MOCVD below 500°C" Intl. Symp. Integr. Ferroelec. 571-597 (1991).

D.A. Porter and K.E. Easterling, Phase Transformations in Metals and Alloys, Van Nostrand Reinhold (1981).

D. Pramanik and V. Jain, "Barrier Metals for ULSI: Processing and Reliability" **34**(5), 97-102 (1991),

P.S. Prevey, "X-Ray Diffraction Residual Stress Techniques" from Metals Handbook Ninth Ed., **10** (Mater. Characterization), American Soc. for Metals, Ohio; pp.381-392 (1986).

K. Ramakumar, J. Lee, A. Safari and S.C. Danforth, "Ferroelectric Thin Films Deposited by Laser Ablation", Mater. Res. Soc. Symp. Proc. **200**, 121-126 (1990).

C.A. Randall, D.J. Barber and R.W. Whatmore, "A TEM Study of a modified PZT-ferroelectric Ceramic" Inst. Phys. Conf. Ser. **78**(13), 531-534 (1985).

I.M. Reaney, K. Brooks, R. Klissurska, C. Pawlaczyk, and N. Setter, "Use of Transmission Electron Microscopy for Characterization of Rapid Thermal Annealed, Solution-Gel, Lead Zirconate Titanate Films", J. Am. Ceram. 77(5), 1209-1216 (1994).

R.W. Rice and R.C. Pohanka, "Grain-Size Dependence of Spontaneous Cracking in Ceramics", J. Amer. Ceram. Soc. **62**(11-12), 559-563 (1979).

R.S. Roth, "Classification of Perovskite and Other ABO_3-Type Compounds", J. Res. Nat. Bur. Stand. **58**, 75-78 (1957).

R.A. Roy, K.F.Etzold, J.J. Cuomo, and T.J. Watson, "Lead Zirconate Titanate Films Produced by 'Facing Targets' RF-Sputtering", Mater. Res. Soc. Symp. Proc. **200**, 77-82 (1990a).

R.A. Roy, K.F.Etzold and J.J. Cuomo, "Ferroelectric Film Synthesis, past and present: A Select Review", Mater. Res. Soc. Symp. Proc. **200**, 141-152 (1990b).

K.L. Saenger, R.A. Roy, K.F. Etzold and J.J. Cuomo, "Lead Zirconate Titanate Films Produced by Pulsed Laser Deposition", Mater. Res. Soc. Symp. Proc. **200**, 115-120 (1990).

Y. Sakashita, T. Ono, H. Segawa, K. Tominaga and M. Okada, "Preparation and Electrical Properties of MOCVD-deposited PZT Thin Films" J. Appl. Phys. 69(12), 8352-8357 (1991).

M. Sayer, C.V.R. Vasant Kumar, D. Barrow, L. Zou, and D.T. Amm, "Integrated Piezoelectric and Pyroelectric Devices from Thin Film Ferroelectrics", Mater. Res. Soc. Symp. Proc. **243**, 39-48 (1992).

R.W. Schwartz, D. Dimos, S.J. Lockwood, and V.M. Torres, "Electrical Properties of Sol-Gel PZT Thin Films for Decoupling Capacitor Applications" Mater. Res. Soc. Symp. Proc. **310**, 59-64 (1993).

J.F. Scott, "Ferroelectric Thin-Film Memory Devices" Symp. on Integr. Ferroelec., Colorado Springs (1989).

A. Segmüller and M. Murakami, "X-Ray Diffraction Analysis of Strains and Stresses in Thin Films" in Analytical Techniques for Thin Films **27** (Treatise on Mater. Science and Technology), Academic Press, Toronto (1988).

J. Scott-Thomas, "Electrical Fatiguing and Piezoelectric Measurements of Thin Film PZT" presentation given at NTEL by NRC (February 1994).

B.S. Sharma, "Retention in Thin Ferroelectric Films", Ferroelectrics **5**, 69-75 (1973).

W.H. Shepherd, "Fatigue and Aging in Sol-Gel Derived PZT Thin Films", Mater. Res. Soc. Proc. **200**, 277-288 (1990).

M. Shimizu, M. Fujimoto, T. Katayama, T. Shiosaki, K. Nakaya, and M. Fukagawa, presentation at Spr. Mater. Res. Soc. Mtg. (1993).

M. Shimizu, T. Katayama and T. Shiosaki, "growth of $PbTiO_3$ Films by Photo-MOCVD" Vacuum **42**(16), 1069 (1991).

Y. Shintani, K. Sato, M. Sakamoto, H. Fukuda, and O. Tada, "$Pb(Zr,Ti)O_3$ Films by rf Sputtering in PbO Vapour", Jpn. J. Appl. Phys. **17**(3), 573-574 (1978).

G. Shirane, R. Pepinsky, and B.C. Frazer, "X-ray and Neutron Diffraction Study of Ferroelectric $PbTiO_3$" Acta. Cryst. **9**, 131-140 (1956).

G. Shirane, S. Hoshino, and K. Suzuki, "X-Ray Study of the Phase Transition in Lead Titanate" Phys. Rev. **80**, 1105-1106 (1950).

K.L. Siefering and G.L. Griffin, "Kinetics of Low-Pressure Chemical Vapor Deposition of TiO_2 from Titanium Tetraisopropoxide", J. Electrochem. Soc. **137**(3), 814-818 (1990a).

K.L. Siefering and G.L. Griffin, "Growth Kinetics of CVD TiO_2: Influence of Carrier Gas", J. Electrochem. Soc. **137**(4), 1206-1208 (1990b).

K.J. Sladek and H.M. Herron, "Titanium Oxide Coatings", Ind. & Eng. Chem., Prod. Res. & Dev. **11**, 92 (1972).

K. Sreenivas, I. Reaney, T. Maeder, N. Setter, C. Jagadish and R.G. Elliman, "Investigation of Pt/Ti Bilayer Metallization on Silicon for Ferroelectric Thin Film Integration", J. Appl. Phys. **75**(1), 232-239 (1994).

W.C. Stewart and L.S. Costentino, "Some Optical and Electrical Switching Characteristics of a Lead Zirconate Titanate Ferroelectric Ceramic", Ferroelectrics **1**, 149-167 (1970).

S.L. Swartz, "Topics in Electronic Ceramics", IEEE Trans. Electrical Insulation **25**(5), 935-987 (1990).

S.L. Swartz, D.A. Seifert, and G.T. Noel, "Characterization of MOCVD $PbTiO_3$ Thin Films", Ferroelectrics **93**, 37-43 (1989).

E.V. Sviridov, VI.M. Mukhortov, V.P. Dudkevich and E.G. Fesenko, "Ferroelectric Properties of $Pb(Zr,Ti)O_3$ Films grown by rf Cathode Sputtering" Sov. Phys. Tech. Phys. 30(5), 576-577 (1985).

L.E. Tanner and M.F. Ashby, "On the Relief of Ordering Strains by Twinning" Phys. Stat. Sol. **33**, 59-68 (1969).

T.C. Tisone and J. Drobeck, "Diffusion in Thin Film Ti-Au, Ti-Pd, and Ti-Pt Couples", J. Vac. Sci. & Technol. 9(1), 271-275 (1971).

M.F. Toney, T.C. Huang, S. Brennan and Z. Rek, "X-Ray Depth Profiling of Iron Oxide Thin Films", J. Mater. Res. 3(2), 351-356 (1988).

S. Trolier, C. Geist, A. Safari, R.E. Newnham and Q.C. Xu, "Etched Piezoelectric Structures" IEEE, 707-710 (1986).

K.N. Tu and R. Rosenberg (eds.), Analytical Techniques for Thin Films, Treatise on Mat. Sci. and Technol. **27** (1988).

M. Venkatesan, S. McGee and U. Mitra, "Indium Tin Oxide Thin Films for Metallization in Microelectronic Devices" Thin Solid Films **170**(2), 151-162 (1989).

J.A. Voigt, B.A. Tuttle, T.J. Headley, M.O. Eatough, D.L. Lamppa and D. Goodnow, "Oriented Lead Zirconate Titanate Thin Films: Characterization of Film Crystallization", Mater. Res. Soc. Symp. Proc. **310**, 15-21 (1993).

C.C. Wang, K.H. Zaininger and M.T. Duffy, "Vapor Deposition and Characterization of Metal Oxide Thin Films for Electronic Applications" RCA Review **31**(4), 728-741 (1970).

L. Weaver, L.D. Madsen and E. Griswold, "Structural Characterization of Nb-doped Lead Zirconate Titanate Ferroelectric thin films", Inst. of Physics Conf. Ser. **117**(6), 383-388 (1991).

L. Weaver and D. Mayer, presented Cdn. Microscopy Conf., Montreal (1994).

C.H.L. Weightens and P.A.C. van Loon, "Low Resistive, Ohmic Contacts to Indium Thin Oxide", J. Electrochem. Soc. **137**(12), 3928-3930 (1990).

E.W. White and J.J. Johnson,Jr., X-Ray Emission and Absorption and Wavelength and 2-Theta Tables, 2nd. Ed., ASTM, PA, USA (1970).

W.B. White, F. Dachille and R. Roy, "High-Pressure - High-Temperature of Polymorphism of the Oxides of Lead", J. Am. Cer. Soc. 44(4), 170-174 (1961).

D. Wicaksana, A. Kobayashi and A. Kinbara, "Process Effects on Structural Properties of TiO_2 Thin Films by Reactive Sputtering" J. Vac. Sci. Technol. A **10**(4), 1479-1482 (1992).

S. Wolf, Silicon Processing for the VLSI Era, Vol.2: Process Integration, Lattice, Sunset Beach CA USA, pp. 268-269 (1990).

S. Wolf and R.N. Tauber, Silicon Processing for the VLSI Era, Vol.1: Process Technology, Lattice, Sunset Beach, CA USA (1986).

W. Wong-Ng, T.C. Huang, L.P. Cook, P.K. Schenck, M.D. Vaudin, C.K. Chiang and P.S. Brody, Mater. Res. Soc. Proc. **243**, 423 (1992).

J.S. Wright and L.F. Francis, "Phase Development in Si Modified Sol-Gel Derived Lead Titanate", J. Mater. Res. 8(7), 1712-1720 (1993).

G. Yi, Z. Wu and M. Sayer, "Preparation of $Pb(Zr,Ti)O_3$ Thin Films by Sol-gel Processing: electrical, optic, and electro-optic properties", J. Appl. Phys. 64(5), 2717-2724 (1988).

I.K. Yoo, S.B. Desu and J. Xing, "Correlations among Degradations in Lead Zirconate Titanate Thin Film Capacitors", Mater. Res. Soc. Symp. Proc. **310**, 165-177 (1993).

S.G. Yoon, J.D. Park, J.H. Choi and H.G. Kim, "Preparation, Properties and Characterization of Thin Ferroelectric Films of Lead Titanate", J.Vac. Sci. Technol. A9(2), 281-285 (1991).

S.G. Yoon and H.G. Kim, "Characterization and Electrical Properties of Chemical Vapor Deposited Ferroelectric Lead Titanate Films on Titanium", IEEE Trans. Ultrasonics 37(5), 333-338 (1990).

S.G. Yoon, H.Y. Lee and H.G. Kim, "Compositional Analysis of Lead Titanate Thin Films by Auger Electron Spectroscopy and their Electrical Properties" Thin Solid Films **171**, 251-262 (1989).

S.G. Yoon and H.G. Kim, "Preparation and Deposition Mechanism of Ferroelectric $PbTiO_3$ Thin Films by Chemical Vapour Deposition", J. Electrochem. Soc. **135**, 3137-3140 (1988).

T. Zheleva, P. Tiwari and J. Narayan, "Textured $Pb(Zr_{0.54}Ti_{0.46})O_3$ Thin Films with $YBa_2Cu_3O_{7.5}$ and Yttria-Stabilized Buffer Layers on (001) Si" Mater. Res. Soc. **310**, 215-220 (1993).

APPENDIX A: Sequence of steps for depositions

Table A.I: Furnace Sequence Description

Interval	Description	Duration
0	standby mode: wafer loading	
1	dummy step: no change in conditions	1 s
2	door seal, slow pump activated	13 min
3	purge: 300 sccm N_2	1.5 min
4	evacuation and pumpdown	6 min
5	leak check: maximum increase 60 mTorr/min	1 min
6	temperature stabilization to ±5°C of setpoint/s (heater manually turned on during this interval)	not preset: until condition is met
7	introduction of non-reactive gases (N_2, O_2)	0.5 min
8	introduction of TIP (if required)	0.5 min
9	deposition stage and introduction of PbEt (if required)	as specified (0.33 - 4 hr)
10	O_2 flow only	0.5 min
11	evacuation	2 min
12	purge until temperature <300°C (heater manually turned off during this interval)	manual
13	vent: 9900 sccm N_2	5 min
14	idle with full vent	manual

APPENDIX B: Calibration of RTA control thermocouple

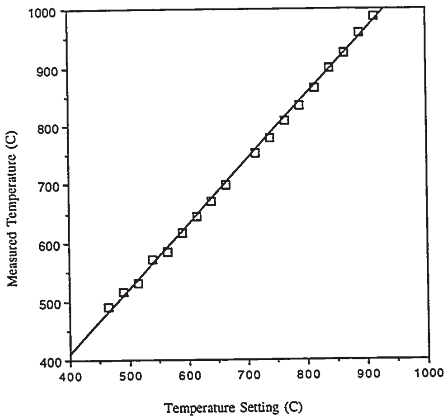

Figure B.1: Calibration of the RTA control thermocouple. The line drawn is $y = -32.585 + 1.1046\,x$ where x is the temperature set on the RTA system and y is the measured (actual) temperature. This line represents the best fit through the data (with an R^2 value of 0.999).

APPENDIX C: TiO_2 Matrices Run Conditions

Matrix One used for the screening experiment with the conventional configuration (Table C.I). The general outline of the experimental conditions was given in §3.1.3 in Table XI. The deposition duration was fixed at 40 min. Five runs were conducted prior to starting the matrix to find the system limitations. The matrix was generated using ECHIP software (Expert in a Chip, Inc., Hockessin, DE USA). Adjustments to the planned matrix were made on two accounts: (i) due to flow limitations, the deposition conditions at 1000 sccm total flow were modified to 750 sccm after run number 10709 and (ii) some of the replicate runs were eliminated on the basis of the results. The final experimental matrix is shown (Table C.I).

Table C.I: Matrix One

substrate temperature (°C)	pressure (Torr)	Ti source temperature (°C)	total flow (sccm)	ratio of O_2 to Ti carrier	run ref. number[a]	comments
300	1.5	45	1000	1.5	10706	
450	1.0	35	700	1.0	10707	centre point
300	0.5	25	400	1.5	10708	
300	0.5	25	1000	0.5	10709	
300	0.5	45	400	0.5	10710	
600	1.5	45	750	0.5	10711	
600	0.5	25	400	0.5	10812	
300	1.5	25	400	0.5	10813	
300	1.5	45	750	1.5	10814	
600	0.5	45	750	1.5	10815	
600	1.5	45	400	1.5	10816	
600	1.5	25	750	1.5	10817	
300	0.5	45	750	0.5	10818	added[b]
300	0.5	25	1000	1.5	10819	added
300	0.5	25	1000	1.5	10820	added

[a] The run reference numbers are encoded as follows: the first digit comes from the year, i.e. 1993 → 3, the next 2 digits indicate the month (04 for April) and the last two numbers are the last 2 digits from the run number, i.e run 329 → 29. For example, run number 329 executed in April of 1993 would be listed as 30429.

[b] Added runs from another fraction of the experiment were used to verify the findings. For additional information on experimental designs see Box et al. [1978].

Matrix two of the screening experiment with the modified distribution for the Ti vapour is shown (Table C.II). The total flow was fixed at 640 sccm and the duration at 4 hr.

Table C.II: Matrix Two

substrate temperature (°C)	pressure (Torr)	Ti source temperature (°C)	Ti carrier flow (sccm)	Ratio of O_2 to Ti carrier	run ref. numbe r	comments
300	0.5	45	16	0.5	11037	
400	3.0	35	30	3.0	11038	
300	3.0	35	16	0.5	11039	
300	0.5	45	16	0.5	11040	replicate
400	0.5	35	16	0.5	11041	
400	3.0	45	30	0.5	11042	
400	3.0	45	16	3.0	11043	
400	3.0	35	30	3.0	11044	
300	3.0	45	30	3.0	11045	
300	0.5	35	30	0.5	11046	
300	0.5	35	16	3.0	11047	
300	3.0	35	16	0.5	11048	
350	1.75	40	23	1.75	11049	
300	0.5	45	16	0.5	11050	replicate

Matrix three was carried out with the heated substrate configuration (Table C.III). The total flow of gasses in the system was set at 500 sccm with a Ti carrier flow of 300 sccm.

Table C.III: Matrix Three

substrate temperature (°C)	pressure (Torr)	Ti source temperature (°C)	O_2 flow (sccm)	duration (hr)	run reference number
400	2	45	0	4	20379
400	0.6	35	0	4	20380
300	2	45	200	4	20381
300	2	35	0	4	20382
300	2	45	200	4	20383
300	0.6	45	0	4	20384
400	0.6	35	0	4	20385
400	2	35	200	4	20386
400	0.6	45	200	4	20388
300	0.6	35	0	4	20489
300	0.6	35	200	4	20490
400	2	45	200	4	20491
300	0.6	45	0	4	20492
400	2	45	0	0.5	20493
400	0.6	35	0	0.5	20494
400	0.6	35	0	4	20495
400	0.6	45	200	0.5	20496
400	2	35	200	0.5	20497
400	2	45	200	0.5	20498

APPENDIX D: Lead oxide run conditions

A listing of the lead oxide runs performed are given in Table D.I, arranged in chronological order. The total flow used for these runs was 900 sccm including 300 sccm of Ar to substitute for the flow of TIP. All runs were 30 min. in duration unless otherwise specified. See Appendix B for explanation of run reference numbers.

Table D.I: Lead Oxide Runs

substrate temperature (°C)	pressure (Torr)	Pb source temperature (°C)	ratio of O_2 to Pb carrier flow	run reference number
515	2	-15	1	20506
[a]515	2	0	1	20507
515	2	+15	1	20508
[a]515	2	0	1	20509
515	2	-15	1	20510
[a]515	2	0	1	20622-4
400	2	0	1	20625
450	2	0	1	20626
515	1	0	1	20627
515	3	0	1	20628
515	2	0	2	20629
[b]515	2	0	1	20630
515	2	0	0.5	20631
515	2	+7.5	1	20632
[a]515	2	0	1	20633
[c]515	2	0	1	20634
515	2	0	0.167	20635
[b]475	2	0	1	20636
[a]515	2	0	1	20738
[c]515	2	0	1	20739

[a] Standard lead oxide run [b] 4 hr. duration [c] 2 hr. duration

APPENDIX E: Development of a $PbTiO_3$ process

Table E.I: Runs conducted using a substrate of Si or SiO_2-coated Si with a temperature of 515°C and a system pressure of 1 Torr for 20 or 60 min with a total flow of 900 sccm. See Appendix B for explanation of run reference numbers.

TIP bubbler temperature (°C)	TIP carrier flow (sccm)	PbEt bubbler temperature (°C)	PbEt carrier flow (sccm)	O_2 flow (sccm)	run reference number/s
35	30	0	600	270	21104
35	50	0	300	550	21102
45	50	0	300	550	21089, 21103
35	100	0	300	500	21110, 21112 21113, 21223 30130
35	150	0	300	450	21114, 21119 21224, 21227
35	175	0	300	425	21115, 21225 30129, 30132 30135
35	200	0	200	300	21101, 21116 21118, 21220 30131
35	300	0	300	300	21099, 21107 21109, 21111 21221, 21226
35	300	0	200	300	21100, 21117 21222, 30128
45	300	0	100	500	21087
35	50	10	300	550	21090
35	200	10	200	500	21092
35	300	10	100	500	21091
35	50	20	300	550	21095
35	300	20	300	300	21094
35	300	20	100	500	21096, 21097 21098
35	300	20	50	550	21093

APPENDIX F: Final set of films

The run reference numbers (see Appendix C for explanation) are indicated for each TIP carrier flow and substrate.

Table F.I: Final $PbTiO_3$ Films

TIP carrier flow (sccm)	substrates			
	SiO_2	Pt: BNR	Pt: MCNC	Pt: NT
175	30129 30132 30356 30364 30369 30375-6 30382 30389 30397-9	30358* 30368* 30379* 30386 30396 30403* 30425-6	30359 30374 30378 30387 30395 30404	30357 30367 30377 30405 30411-2
180	30391 30393 30424	30415 30417 30421* 30423	30414 30418-9 30422	30416 30420
190	30360 30366 30370 30380-1 30384 30400-2	30242 30361 30371 30385 30390* 30392 30410*	30362 30373 30393 30388 30406-7	30363 30365 30372 30408-9 30413

*photographed (figure 42)

Annealing

(i) 175 and 190 TIP flows, all Pt choices

in a N_2 ambient for 615°C, 40 s,

run reference numbers: 30405, 30407, 30359, 30361, 30363, 30396

(ii) 190 TIP flow, MCNC Pt

in an O_2 ambient for 490°C, 40 s - run reference number: 30373

in an O_2 ambient for 515°C, 40 s - run reference number: 30388

in an O_2 ambient for 585°C, 40 s - run reference number: 30362

in an O_2 ambient for 698°C, 40 s - run reference number: 30383

Table F.II: Corresponding set of titanium and lead oxide films

TIP carrier flow (sccm)	PbEt carrier flow (sccm)	SiO_2	Pt: BNR
175	0	30139	30428
0	300	30138	30429

APPENDIX G: Indexing of Electron Diffraction Patterns

d-spacings were calculated from equation (2.11) where λ is 0.0251 Å for an operating voltage of 200 kV. The nominal values of 60, 80, 100 and 120 cm used as camera lengths were adjusted to the measured values (Table G.I). Eqn. 2.11 may be rewritten as follows:

$$d = 2\ (0.0251)\ L\ /\ D$$

$= x / R$ where x was the calculated amount for the numerator (Table G.I) and R was the measured ring radius.

Table G.I: Parameters for calculating d-spacings

Nominal value for L (cm)	Measured value for L (cm)	Corresponding value for x (Å.cm)
60	59.5	1.494
80	81.2	2.038
100	100.1	2.513
120	121.8	3.057

APPENDIX H: Data on Deposition Rates

Table H.I: Deposition rate dependence on substrate temperature. Conditions of deposition (i) TiO_2: system pressure 0.6 Torr, total flow 500 sccm with 300 sccm of TIP and 200 sccm of N_2, TIP temperature of 35 °C, duration 20 to 240 min; and (ii) Pb-O: system pressure 2 Torr, total flow 900 sccm with 300 sccm PbEt, 300 sccm O_2 and 300 sccm Ar or N_2, PbEt temperature of 0 °C, duration 30 to 240 min.

Substrate Temperature (°C)	TiO_2 Deposition Rate (μm.hr^{-1})	Run Reference Numbers	PbO_x Deposition Rate (μm.hr^{-1})	Run Reference Numbers
325	0.04	20743	-	
350	0.2034	20613	-	
400	0.261,0.383,0.279, 0.353,0.224,0.299, 0.534	20747,20742,20750 20752,20502,20612 21086	<0.1	20625
450	-		0.30	20626
475	-		0.42	20636
500	-		0.465, 0.542	20739, 20738
508	-		0.630	20633
515	1.695,2.172, 2.049	20611,20619, 20620	0.965, 1.024, 1.862, 1.488, 1.155, 1.275	20507, 20509, 20623, 20624, 20630, 20634

Table H.II: Deposition rate dependence on TIP temperature. Conditions of deposition of TiO_2: substrate temperature 400 °C, system pressure 2.0 Torr, total flow 500 sccm with 300 sccm of TIP and 200 sccm of O_2, duration 20 to 240 min.

TIP Temperature (°C)	Deposition Rate of TiO_2 (μm-hr^{-1})	Run Reference Number
20	0.445	20618
35	0.099	20856
45	0.635	20854
60	0.865	20751

Table H.III: Deposition rate dependence on PbEt temperature. Conditions of deposition of lead oxide: system pressure 2 Torr, total flow 900 sccm with 300 sccm PbEt, 300 sccm O_2 and 300 sccm Ar or N_2, duration 30 min.

PbEt Temperature (°C)	Deposition Rate of Pb-O (μm-hr^{-1})	Run Reference Number
-15	0.600	20506
-15	up to 0.618	20510
0	1.30 ± 0.56	see Table H.I
7.5	2.08	20632
15	2.02	20508

Table H.IV: Deposition rate dependence on system pressure. Conditions of deposition (i) TiO_2: substrate temperature 400 °C, total flow 500 sccm with 300 sccm of TIP and 200 sccm of O_2, TIP temperature of 45 °C, duration 20 to 240 min; and (ii) Pb-O: substrate temperature of 515 °C, total flow 900 sccm with 300 sccm PbEt, 300 sccm O_2 and 300 sccm Ar or N_2, PbEt temperature of 0 °C, duration 30 - 120 min.

Pressure (Torr)	TiO_2 Deposition Rate (μm-hr^{-1})	Run Reference Number	Pb-O Deposition Rate (μm-hr^{-1})	Run Reference Number
0.6	0.135	20855	-	
1.0	0.473,0.398	20614,20749	up to 0.165	20627
2.0	0.635	20854	1.30 ± 0.56	see Table H.I
2.8	0.560	20616	-	
3.0	-		2.06	20628

Table H.V: Deposition rate dependence on oxygen flow. Conditions of deposition (i) TiO_2: substrate temperature 400 °C, system pressure of 2 Torr, total flow 500 sccm with 300 sccm of TIP, O_2 as specified, and balance of N_2 or Ar, TIP temperature of 45 °C, duration 20 to 240 min; and (ii) Pb-O: substrate temperature of 515 °C, system pressure of 2 Torr, total flow 900 sccm with 300 sccm PbEt, O_2 as specified, and balance of Ar or N_2, PbEt temperature of 0 °C, duration 30- 120 min.

Oxygen flow (sccm)	TiO_2 Deposition Rate (μm-hr^{-1})	Run Reference Number	Pb-O Deposition Rate (μm-hr^{-1})	Run Reference Number
0	0.825	20613	-	
50	-		1.015	20635
100	0.700	20748	-	
150	-		1.102	20631
200	0.635	20854	-	
300	-		1.30 ± 0.56	see Table H.I
600	-		0.756	20629

APPENDIX I: X-ray diffraction of a lead oxide thin film

A comparison was made between the x-ray spectra of a thin film lead oxide, two JCPDS standards: 5-561 (litharge) and 35-1482 (α-PbO), and the Diffract simulations for each of the oxides as described in §2.4.2. Table I.I shows d-spacings in nm and the bold type indicates the most significant additional reflections in the simulated litharge pattern. The criteria selected for a match was a d-spacing difference of less than 0.002 nm. Separation in peak values of less than 0.05° would not be noticeable with the acquisition conditions used (0.1° slits and 0.05° steps) and hence the peak splitting noted for the standard patterns could not be observed. Although the match is better for the α-PbO sample than for the litharge sample, this could be due to a systematic shift in the collected spectrum from a small system alignment or sample height error. An offset of this order of magnitude would not normally cause any confusion in "peak matching" and could be corrected in samples containing a known phase. To eliminate the ambiguity, electron diffraction analysis was done.

Table I.I: Comparison of d-spacings

Thin Film	litharge		α-PbO	
Spectrum	JCPDS	Diffract	JCPDS	Diffract
.30960	.3115	.31157	.31037	.31037
.27988	.2809	.28093	.28042	.28043
			.28018	.28018
.26184				
.24909	.2510	.25109	.24946	.24947
.22243				
.21113	.2124	.21225	.21113	.21114
.20499				
.19764	.1988	.19865	.19820	.19820
.18638	.1872	.18721	.18639	.18639
			.18632	.18632
.18380		**.18472**	.18420	.18420
.16681	.1675	.16750	.16710	.16710
		.16739	.16699	.16700
			.16631	.16631
.15812				
.15503	.1558	.15579	.15518	.15519
.15348	.1542	.15426	.15336	.15336
.14437	.1438	.14503	.14454	.14454
			.14447	.14447
.14300		**.14380**	.14304	.14305
			.14301	.14301
.14022	.1405	.14046	.14021	.14021
			.14009	.14009
.13501		**.13527**	.13498	.13498
			.13487	.13487
.12744	.1282	.12805	.12773	.12773
			.12740	.12740
.12503	.1256	.12563	.12539	.12539
		.12554	.12532	.12532
.12229	.1226	.12259	.12223	.12223
			.12215	.12215
.12134	.1219	.12188	.12160	.12161
		.12184	.12155	.12155
			.12131	.12131
			.12127	.12127

APPENDIX J: EMPA results of a litharge-scrutinyite sample

Table J.I: Film Composition

Acquisition Number	Si (at.%)[a]	Pb (at.%)[b]	Ti (at.%)[c]	O (at.%)[d]
1	3.62	45.84	0.18	50.35
2	3.73	45.00	0.18	51.09
3	3.67	45.14	0.12	51.07
4	3.82	46.45	0.11	49.61
5	3.67	45.65	0.10	50.59
6	3.80	45.87	0.17	50.16
7	3.84	44.44	0.09	51.62
8	4.16	45.07	0.23	50.54
9	4.22	44.33	0.08	51.38
Average	3.77	45.42	0.14	50.71
Standard Deviation	0.28	0.58	0.05	0.60

[a] K line for Si
[b] M line for Pb
[c] K line for Ti
[d] K line for O

APPENDIX K: Lattice parameter calculation

X-ray wavelength used in calculation: 1.540598 Å

refinement based on the following class: tetragonal

Lattice Constants	Standard Errors
a= 3.901214	.0045630
c= 4.152091	.0069906

volume of unit cell = 63.193 Å^3

Table K.I: Lattice Parameter Calculation

hkl	2θ (obs.)	2θ (calc.)	delta (2θ)	d (obs.)	d (calc.)	delta (d)001
001	21.399	21.383	.016	4.149	4.152	-.003
100	22.659	22.776	-.117	3.921	3.901	.020
101	31.555	31.440	.115	2.833	2.843	-.010
110	32.352	32.429	-.077	2.765	2.759	.007
111	39.259	39.175	.084	2.293	2.298	-.004
200	46.359	46.520	-.161	1.957	1.951	.007
201	51.753	51.737	.016	1.765	1.765	-.003
210	52.391	52.401	-.010	1.745	1.745	.003
112	55.332	55.340	-.008	1.659	1.659	-.007
211	57.246	57.228	.018	1.608	1.6-8	-.001
202	65.181	65.622	-.441	1.4301	1.4216	.0086
003	67.600	67.637	-.037	1.3847	1.3840	.0007
212	70.650	70.440	.210	1.3322	1.3357	-.0034
301	76.809	76.738	.071	1.2400	1.2410	-.0010

Obs. (Observed value),
Calc. (Calculated value for final lattice parameters),
Delta (difference in observed and calculated values).

APPENDIX L: EMPA of $PbTiO_3$

L.1 Analysis for Carbon

The possible presence of carbon in the $PbTiO_3$ was a particular concern because of the precursors used in the deposition process: $Ti(OC_3H_7)$ and $Pb(C_2H_5)_4$. Incomplete oxidation could result in C being incorporated into the film.

Detailed EMPA was performed on a Cameca Camelbax MBX probe. The specimen thought to have the highest C content (from preliminary EMPA work) was probed at 5 kV, using a 6 nm 2d-spacing synthetic multi-layer diffracting crystal. The specimen was found to be a reasonable conductor without the usual 25 nm carbon coating. The secondary electron image showed the film did not have a uniform surface but exhibited significant roughness. An appreciable signal was detected at the C-Kα angle equivalent to several weight percent carbon if it was indeed real. In x-ray tables [White and Johnson 1970], a Pb N_V-$N_{VI\text{-}VII}$ line is listed quite close to the C-Kα position with an unspecified intensity. No lines were listed in this vicinity for Ti. To see if there was an interference giving rise to the "carbon" signal, a series of 2θ scans were run across the C-Kα angle ($\pm 0.02 \sin\theta$) on sample LM30405, carbon (diamond), pure Pb and pure Ti. A somewhat lower current was used on the carbon in order to facilitate comparison with the other curves. Evidently both Pb and Ti have lines that gave significant intensity near the C-Kα position (figure L.1). The Pb-$N_{V\text{-}VII}$ line is the more important of the two since it has a higher intensity and because of the large weight fraction of Pb in $PbTiO_3$. The position of the signal from the thin film coincides with that of the Pb not with the C. If the Pb content varies substantially from specimen to specimen then the false C-Kα signal should vary in direct proportion. This result was indeed found with preliminary EMPA where the apparent C was found to track the Pb content.

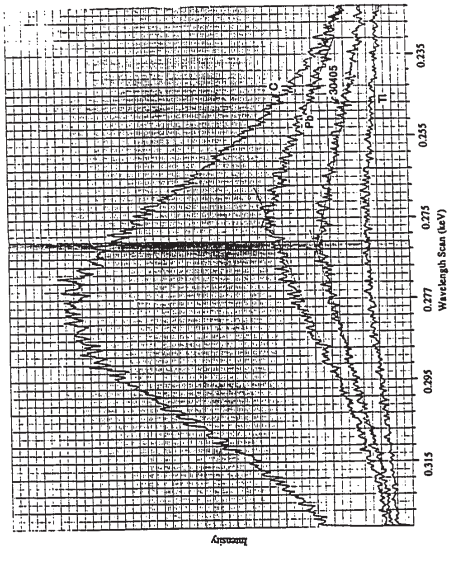

Figure L.1: EMPA 2θ Scans

L.2 Estimation of surface PbO_x thickness.

TEM plan-view samples had a diffraction pattern corresponding to an amorphous phase and EDS indicated Pb and O in the absence of Ti. Further ion mill thinning of the surface removed this layer, thereby eliminating TEM sample preparation as a possible cause. Raman spectroscopy, SEM cross-sectional examination and AES were unable to discern anything different about the surface from the bulk of the film.

With specimen LM30363E, the depth uniformity of the $PbTiO_3$ layer was explored. This examination was done by using a series of progressively lower accelerating voltages (E_o). To help visualize where the x-ray generation occurred, the Gaussian $\phi(\rho z)$ theory [Packwood and Remond 1992] was applied. One particulary useful parameter in the theory is the $3/2\alpha$ (excitation) range for the electron beam. $3/2\alpha$ is a mass-thickness parameter that indicates $\sim 90^{+}\%$ of all x-rays generated (figure L.2). The $3/2\alpha$ ranges for each voltage were calculated (Table L.I). The ranges were converted to thickness (depths) on the basis of a density, $\rho = 5$ g-cm^{-3} (§2.5). The results for Pb-Mα on the pure metal (oxide free) and the $PbTiO_3$ showed their ratios varied (from 0.55 to 0.62) over the range of ~ 3 to 10 kV, but no trends

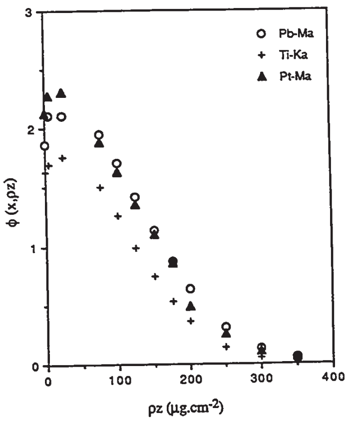

Figure L.2: Mass-depth distribution of x-ray production for a given element.

were observed. At yet a lower kV (using a separate precise high voltage meter) of 2.76 kV, a $PbTiO_3$: Pb value of 0.66: 1 was obtained. This ratio is somewhat higher than the calculated one of 0.57: 1. The $3/2\alpha$ curve was used to estimate that a pure (100% dense) PbO layer in the range of 1.5 to 3.0 nm would cause a 0.09 shift in the ratio value.

Table L.I: $3/2\alpha$ values for various accelerating voltages.

E_o (kV)	Pb-Mα Depth (nm)	Ti-Mα Depth (nm)
10	550	480
8.5	-	346
7.5	340	-
7	-	218
6	-	135
5.5	-	89
5.2	-	55
5	162.5	-
4	101.5	-
3	42	-

APPENDIX M: Electrical measurements and calculations

Table M.I: Electrical properties of an etched $PbTiO_3$ CVD sample with small Au top electrodes and no post-deposition anneal.

Frequency (kHz)	Capacitance (pF)	Resistance (MΩ)	tan δ	Hysteresis properties
1	61-62	69-75	~0.04	linear
10	59	7-8	~0.03	linear
100	56-57	~1	0.03-0.04	linear
1000	55-56	0.5-1	0.05-0.06	N.A.

For example, using a film thickness of 405 nm and eqn. 2.16 (§2.7.2) with small electrode dots, ϵ' can be found:

$$\epsilon' = (d\,C) / (\epsilon_o A)$$

$$= 405\text{x}10^{-9}\, C_p / (8.85\text{x}10^{-12} \text{ x } \pi(77.5\text{x}10^{-6})^2)$$

$$= 2.425\text{x}10^{12}\, C_p$$

To convert from resistance to resistivity equation 2.21 (§2.7.2) is used:

$$\rho = R_p\, A / d$$

$$= R_p\, \pi(77.5\text{x}10^{-6})^2 \text{ x } 10^4 / 0.405\text{x}10^{-6}$$

$$= 465.9\, R_p$$

for small dots and films 405 nm thick.

Table M.II: Electrical properties of a 585°C annealed $PbTiO_3$ CVD sample with small Au top electrodes.

Frequency (kHz)	Capacitance (pF)	Resistance (MΩ)	tan δ	Hysteresis properties
1	19-25	36-40	0.13-0.21	yes
10	16-18	12-13	0.05-0.06	no*
100	16-17	~3	0.03-0.04	no*
1000	16-17	~0.4	0.03	N.A.

*switching frequency is too high for the material; this effect has been observed by others.